Electroproduction of the $\phi(1020)$ Vector Meson at 4 GeV.

Konstantin Loukachine

Dissertation submitted to the Physics Department of the
Virginia Polytechnic Institute and State University
in partial fulfillment of the requirements for the degree

Doctor of Philosophy
in
Physics

John Ficenec, Co-Chair
Elton Smith, Co-Chair
Richard Arndt
David Jenkins
Titzuro Mizutani
Mark Pitt

February 1, 2000
Blacksburg, Virginia

Keywords: Vector Meson, Electroproduction, Strangeness, Nucleon

Electroproduction of the $\phi(1020)$ Vector Meson at 4 GeV.

Konstantin Loukachine

ABSTRACT

We studied the reaction $ep \to e'p'\phi$ with a 4.2 GeV incident electron beam in the region of the electroproduction variables Q^2 from 0.7 to 2.2 GeV^2 and W from 2.0 to 2.6 GeV. The data were taken and analyzed at the Thomas Jefferson National Accelerator Facility. For the first time, we observe the expected t-slope dependence on Q^2 and $\Delta\tau$ in ϕ vector meson production. We find that the width of the forward ϕ-meson diffraction peak increases rapidly as the interaction time decreases below $c\Delta\tau \approx 1$ fm. Within a simple optical model framework, the data show that ϕ meson has a smaller size than the ρ. The measured ϕ cross-section dependence on Q^2 is in a good agreement with previous measurements and well-described by the phenomenological Pomeron-exchange model. Our cross-section data do not favor the standard Vector Meson Dominance and $s\bar{s}$-knockout model predictions. From the angular distribution of the decay $\phi \to K^+K^-$, assuming the s-channel helicity conservation, we extracted the longitudinal-to-transverse cross-section ratio, R, and Vector Meson Dominance scaling parameter, ξ^2, which are consistent with the previous measurements and the model expectations.

This work was supported by the TJNAF and SURA Graduate Student Fellowship Program.

Acknowledgments

This Ph.D. project has extended over more than three years, during which I have received help and encouragement from many people. Among these, my on-site Jefferson Lab adviser Elton Smith played a special role. His continuous help, numerous advises and suggestions made this research project feasible. John Ficenec and David Jenkins, my VPI & SU advisers, deserve special recognition. I would like to thank all my advisers for giving me many opportunities to learn good physics, many valuable skills and experimental techniques. I would like to thank Chris Thomas for great help in overall organization.

I would like to thank my committee members for reading this manuscript. Their comments and suggestions greatly improved the readability and accuracy of this thesis.

My special gratitude to David Cassel from Cornell University for the most interesting and encouraging discussion on this dissertation topic.

Like in most of modern physics projects, this experiment involved a large collaboration of technicians, engineers and scientists. My special thanks to the Hall B research staff for their valuable help, suggestions and advises during these years. I would like to thank the entire CLAS Collaboration, the Hall B technicians and CEBAF team for making this experiment happen, for their excellent work and for their support.

My special thanks to Joe Manak, Richard Thompson, Simeon McAleer, Stephen Barrow, Simon Taylor and John McNabb for their valuable help in software and analysis algorithms development, physics discussions and being good friends.

Finally, I thank my parents for their patience, permanent spiritual support and encouragement, not only during these years, but all my rambling life.

Contents

List of Figures

List of Tables

Chapter 1

Physics Motivation and Existing Data

1.1 Overview of $\phi(1020)$ Electroproduction

Vector meson production has been an important tool used in understanding the hadronic properties of the photon [1]. For low values of Q^2 and W, the photon interacts with the target predominantly through vector meson intermediate states which diffractively scatter from the target, conserving helicity, in a process called Vector-Meson Dominance (VMD) (Figure 1.2). However, as was first discovered in the mid 1970's, for large values of Q^2, the photon directly probes the constituents in the nucleon [2, 3]. These results were interpreted as an onset of non-diffractive, hard production mechanisms. One of such possible production mechanisms of ϕ mesons, is $s\bar{s}$-knockout of the ϕ meson from the proton [4]. A long-standing mystery in ϕ meson electroproduction, as contrasted with ρ meson production, is the constant width of the forward peak as one probes the nucleon with increasing resolution in space and time. The data on ρ meson production [6, 2] show a decrease in width of the forward peak at small interaction time, $\Delta\tau$, and large momentum transfer, Q^2.

Because of the low cross section for ϕ meson electroproduction, only a few measurements have been made [5, 6, 7]. They are statistically limited to low Q^2 in the case of exclusive production, and it is not possible to draw strong conclusions on either diffractive or hard production mechanisms. The relatively high luminosity of CEBAF at Jefferson Lab and large acceptance of the CLAS detector allows the study of the momentum transfer distributions, the angular distribution of K mesons from ϕ decay, and different features of the space-time structure of the virtual photon over a broad Q^2 region.

Figure 1.1 sketches the kinematic quantities of interest in the electroproduction of the ϕ meson. The virtual photon γ_V has mass squared -Q^2 and energy ν. The electron scattering plane is at an angle Φ to the hadron production plane, defined in the $\gamma_V p$ center of mass system. The θ_H and ϕ_H are polar and azimuthal angles of K^+ from decay of the ϕ vector meson in its rest frame. In this frame (Helicity Frame), the z-axis is directed along the

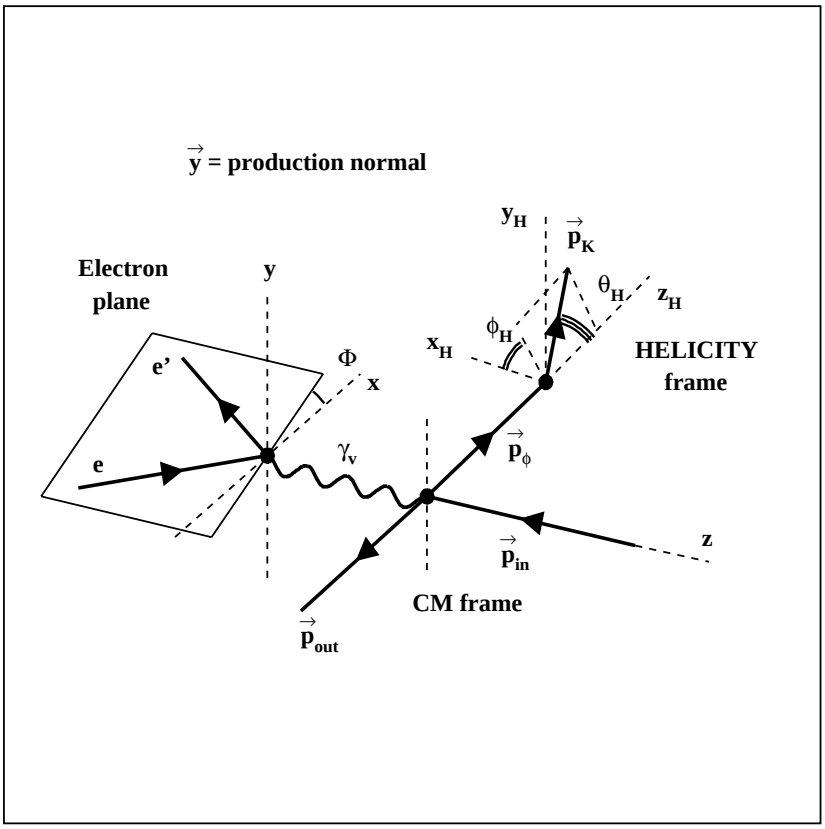

Figure 1.1: Sketch of the electroproduction of ϕ meson. The virtual photon γ_V delivers the electron momentum transfer Q^2 and energy ν. The electron scattering plane is at an angle Φ to the hadron production plane. The θ_H and ϕ_H are polar and azimuthal angles of K^+ from the decay of the ϕ vector meson in its rest frame (Helicity Frame). In this frame the z-axis is directed as the momentum of the ϕ meson in $\gamma_V p$ center of mass system, and y-axis is perpendicular to the ϕ-production plane.

momentum of the ϕ meson in the $\gamma_V p$ center of mass system (s-channel), and y-axis is perpendicular to the ϕ-production plane.

The kinematic variables usually used in description and analysis of vector meson electroproduction are listed below:

• Energy of the virtual photon:

$$\nu = E_e - E_{e'} \ , \tag{1.1}$$

where E_e and $E_{e'}$ are energy of incident and scattered electrons.

• Electron momentum transfer, which can be interpreted as the negative mass squared

of the virtual photon:

$$Q^2 = -q^2 = (P_e - P_{e'})^2 \approx 4E_e E_{e'} sin^2(\frac{1}{2}\theta_{ee'}) \,, \tag{1.2}$$

where P_e and $P_{e'}$ are four-momenta of incident and scattered electrons, and $\theta_{ee'}$ is the angle between their momentum directions.

• Center-of-mass energy squared of the virtual photon-proton system:

$$W^2 = (P_e - P_{e'} + P_p)^2 = (P_{\gamma_V} + P_p)^2 = -Q^2 + M_p^2 + 2M_p\nu \,, \tag{1.3}$$

where P_p and M_p are four-momentum and mass of the proton, respectively, and P_{γ_V} is four-momentum of the virtual photon.

• Momentum transfer from the virtual photon to the vector meson:

$$t = (P_\phi - P_{\gamma_V})^2 = (P_{K^+} + P_{K^-} - P_e + P_{e'})^2 \,, \tag{1.4}$$

where P_ϕ, P_{γ_V}, P_{K^+} and P_{K^-} are the four-momenta of the ϕ meson, virtual photon, positive and negative kaons respectively. We define t' to be

$$t' = \mid t - t_{min} \mid \,, \tag{1.5}$$

where $t_{min}(Q^2)$ is the minimum four-momentum transfer given by :

$$t_{min} = (E_\gamma^\star - E_\phi^\star)^2 - (p_\gamma^\star - p_\phi^\star)^2 \,. \tag{1.6}$$

Here $E_\gamma^\star$ ($E_\phi^\star$) and $p_\gamma^\star$ ($p_\phi^\star$) are the energy and momentum of the virtual photon (ϕ) in the $\gamma_V p$ center of mass frame.

• Formation time, which characterizes the time and size of the interaction. Under the VMD assumption, virtual photon is converted to a virtual ϕ vector meson, which diffractively scatters on the proton (see Figure 1.2). Applying the uncertainty principle to the $\gamma_V\phi$ vertex

$$\Delta\tau = 1/\Delta E \,. \tag{1.7}$$

Assuming also conservation of momentum k_V at the $\gamma_V\phi$ vertex, we have:

$$-Q^2 = q^2 = \nu^2 - k_V^2 \quad \Rightarrow \quad \nu^2 + Q^2 = k_V^2 \,, \tag{1.8}$$

then

$$\Delta E = E_\phi - \nu = (k_V + M_\phi^2)^{1/2} - \nu = (\nu^2 + Q^2 + M_\phi^2)^{1/2} - \nu \,, \tag{1.9}$$

with E_ϕ being the energy of the virtual ϕ meson, and M_ϕ its mass. At large ν, formation time, $\Delta\tau$, approaches asymptotically

$$\Delta\tau = \frac{2\nu}{(Q^2 + M_\phi^2)} \tag{1.10}$$

• Total cross section of the ϕ meson electroproduction:

$$\sigma_\phi(Q^2, W) = \sigma_T(Q^2, W) + \epsilon\, \sigma_L(Q^2, W) = \sigma_T(1 + \epsilon\, R)\,, \tag{1.11}$$

where σ_T and σ_L are cross section terms due to transversely and longitudinally polarized virtual-photons, respectively; $R = \sigma_L/\sigma_T$ is their ratio, and ϵ is the virtual-photon polarization parameter, given by

$$\epsilon = \frac{1}{[\, 1 + 2(Q^2 + \nu^2)/(4EE' - Q^2)\,]}\,. \tag{1.12}$$

• Virtual-photon flux in electroproduction on hydrogen, the probability of a scattered electron, at fixed Q^2 and W, to produce a virtual photon,

$$\Gamma(Q^2, W) \;=\; \frac{\alpha}{8\pi^2}\,\frac{W}{M_p E_b^2}\,\frac{W^2 - M_p^2}{M_p Q^2}\,\frac{1}{1-\epsilon} \tag{1.13}$$

where E_b is the energy of the electron beam and M_p is the mass of the proton.

• The total integrated ϕ meson rate in electroproduction can be written as

$$N_\phi(\Delta Q^2, \Delta W) \propto \sigma_\phi(Q^2, W) \cdot \Gamma(Q^2, W) \cdot L_{int} \cdot \Delta Q^2 \cdot \Delta W\,. \tag{1.14}$$

Here L_{int} is the integrated luminosity

$$L_{int} = \frac{l_t \cdot D_t \cdot N_{Av}}{M_H} \cdot \frac{Q_{int}}{q_e}\,, \tag{1.15}$$

where l_t is the length of the target, D_t is the density of hydrogen, N_{Av} is Avogadro number, M_H is molar density of hydrogen, Q_{int} is the integrated beam charge and q_e is the electron charge.

1.2 Diffractive Production

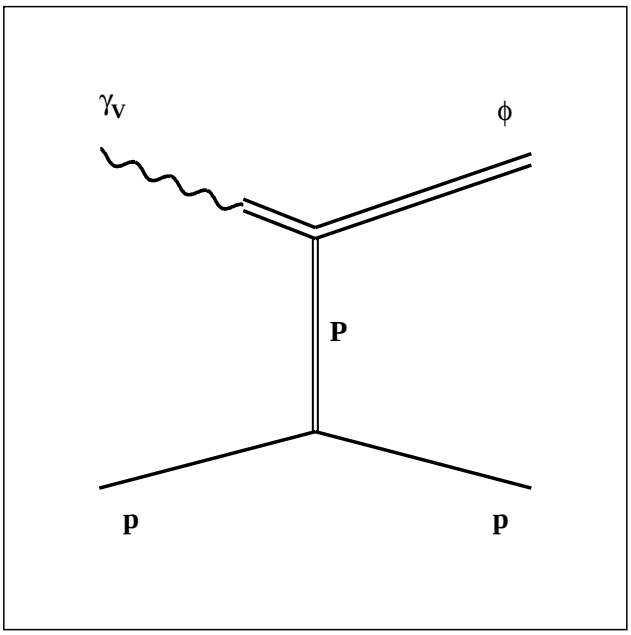

Figure 1.2: Feynman diagram of the ϕ meson diffractive production mechanism.

1.2.1 The Vector-Meson Dominance Model

The dominant mechanism for ϕ meson photo- and electroproduction at low momentum transfer is diffraction, which is usually analyzed using the Vector-Meson Dominance (VMD) model. In this model it is assumed that in the interaction of photons with hadrons, the photon may be decomposed into a superposition of vector meson states, which subsequently scatter elasticly off the hadron [1]. The Feynman diagram of the diffractive producton of ϕ is shown in Figure 1.2. Production of ϕ mesons through this mechanism may be interpreted in terms of the hadronic structure of the photon, which coupled to a virtual meson with a strength proportional to the charge of its constituent quarks. Within this framework, the polarization of ϕ is the same as the polarization of the virtual photon in the s-channel helicity frame (see Figure 1.1), a mechanism referred to as s-channel Helicity Conservation (SCHC).

Cross Section. The diffractive cross section in the VMD model may be written as [1]

$$\sigma_\phi^{VMD}(Q^2,W) = \sigma_\phi(0,W)\,\frac{p_\gamma^\star(Q^2=0)}{p_\gamma^\star(Q^2)}\,\frac{1+\epsilon R}{(1+Q^2/M_\phi^2)^2} \times exp(-b \mid t_{min}(Q^2) - t_{min}(0) \mid) \,, \tag{1.16}$$

[1] See Reference [1], page 375, and Reference [58].

$$\frac{p^{\star}_{\gamma}(Q^2=0)}{p^{\star}_{\gamma}(Q^2)} = \frac{W^2 - M_p^2}{[(W^2 - M_p^2 - Q^2)^2 + 4W^2Q^2]^{1/2}}\,, \tag{1.17}$$

where the factor $\sigma_{\phi}(0,W)/(1+Q^2/M_{\phi}^2)^2$ represents the photoproduction cross section extrapolated to Q^2 by the square of the ϕ meson propagator. The W dependence of the photoproduction cross-section is the same as for the hadron-hadron scattering [7, 9], $\sigma_{\phi}(0,W) \propto W^{0.32}$. The $(1+\epsilon R)$ factor corrects this cross section for the longitudinal component which is missing at Q^2=0. The exponential factor corrects for the fact that for a given W the physical t range is smaller when $Q^2 > 0$ than it is at $Q^2 = 0$. The factor $p^{\star}_{\gamma}(Q^2=0)/p^{\star}_{\gamma}(Q^2)$, where $p^{\star}_{\gamma}(Q^2)$ is the virtual-photon momentum in the $\gamma_V p$ center of mass, represents a correction to the virtual photon flux [59] in Equation 1.13. In the VMD framework, the R is given by

$$R = \xi^2\,\frac{Q^2}{M_{\phi}^2}\,, \tag{1.18}$$

where ξ^2 is VMD scaling parameter and M_{ϕ} is mass of the ϕ meson [13].

Angular Distribution. Under the VMD and SCHC assumptions, the decay distribution $W_D(\cos\theta_H,\psi)$ of the K^+ in the rest frame of the ϕ (see Figure 1.1) has the form [12]:

$$\begin{aligned} W_D(cos\theta_H,\psi) &= \frac{3}{8\pi}\frac{1}{(1+\epsilon\,R)}\{sin^2\theta_H(1+\epsilon\,cos2\psi) + 2\epsilon\,R\,cos^2\theta_H \\ &\quad -\sqrt{2\epsilon(1+\epsilon)R}\,cos\delta\;sin2\theta_H\;cos\psi\}\,, \end{aligned} \tag{1.19}$$

Where $\psi = \phi_H - \Phi$ and $\sqrt{R}e^{i\delta}$ is the ratio of longitudinal to transverse amplitudes. The term proportional to $\cos^2\theta_H$ is due to longitudinally produced ϕ mesons, that is, helicity zero (refer to Appendix B for detail). We note that $W_D(\cos\theta_H,\psi)$, evaluated in s-channel helicity frame (see the frame definition in Figure 1.1), is independent of the momentum-transfer t. After integration over ψ, the decay distribution becomes a function of $cos\theta_H$ alone:

$$W_D(cos\theta_H) = \frac{3}{4}\,\frac{1}{(1+\epsilon\,R)}[1 + (2\epsilon R - 1)\;cos^2\theta_H]\,. \tag{1.20}$$

The simple picture of R increase with Q^2, as predicted by Equation 1.18, was confirmed by the ρ decay distribution in the low Q^2 regime [6], but at $Q^2 \approx 2$ GeV^2 a change of behavior is observed [7]. The summary of the existing R measurements in ρ, ϕ and J/Ψ mesons electroproduction is shown in Figure 1.3. The recent ZEUS helicity analysis of ρ meson electroproduction data show the violation of SCHC [2] at high W and Q^2 [7], which may be the indication of the VMD limits, and can be expected for the ϕ electroproduction as well.

Also, the earlier cross-section measurements in ρ muoproduction disagree with the VMD prediction and show that R is consistent with zero [2]. Hard scattering measurements of

[2]The 15-Parameter Helicity Angle Fit shows a non-zero contribution from the interference of helicity-violating amplitudes (linear combination of the spin-density matrix elements $r^5_{00} > 0$).

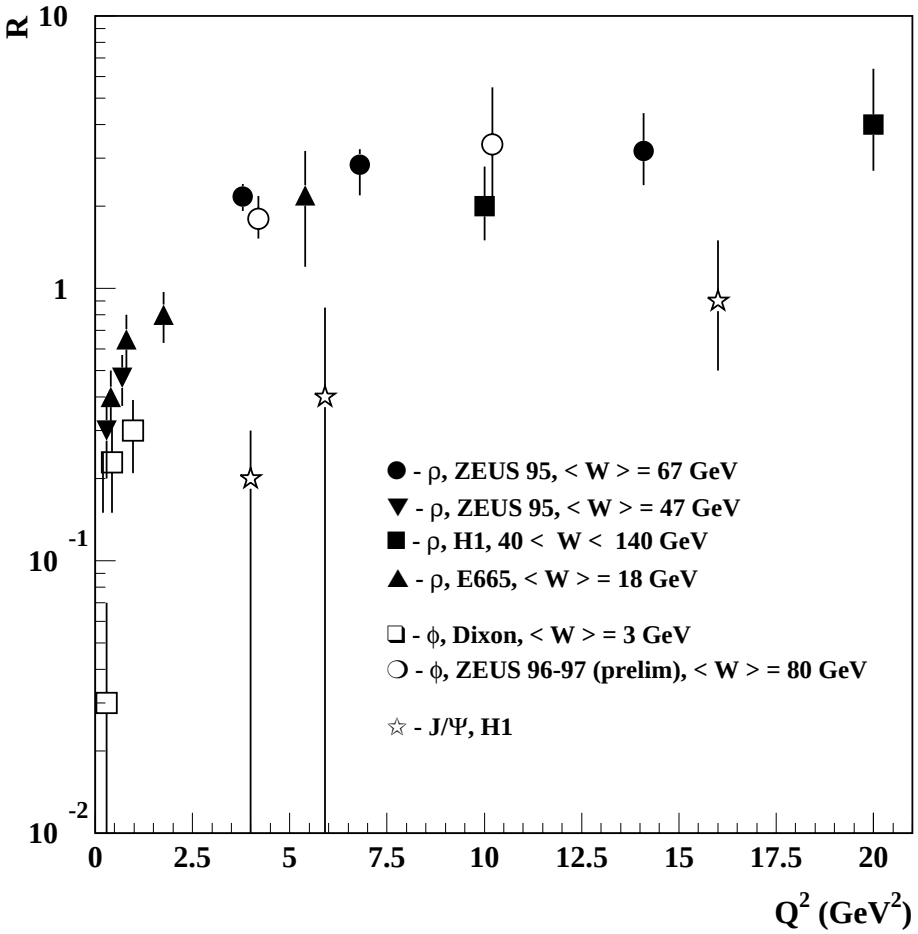

Figure 1.3: The R, measured under the VMD and SCHC assumptions, versus Q^2 for ρ, ϕ and J/Ψ vector mesons.

the W_1 and W_2 proton structure functions in the deep inelastic region also show that R is small (~ 0.13) and does not scale with Q^2 as in Equation 1.18 [1]. At least, the VMD model fails to reproduce the rapid decrease in the cross-section with increasing W, observed in ρ meson electroproduction [6]. The ratio of the measured cross section to VMD predicted cross section, σ_ρ/σ_{VMD}, falls by a factor of 3 from 1.5 to 0.5 in the W range from 2.7 to 4.0 GeV.

Previous Measurements. Most of the measurements of ϕ production have been realized in experiments with unpolarized real photons [14, 15, 16]. They indicate that the ϕ mesons are diffractively produced and conserve helicity. Their agreement with the predictions of the VMD model was considered a confirmation of the model [17, 18]. However, these experiments are limited to Q^2=0. There are only a few measurements of ϕ production by virtual photons [5, 6, 7] . The features of the ϕ electroproduction at low W and Q^2 were measured with

Table 1.1: Values of the parameters of ϕ meson electroproduction measured by [5].

	$<Q^2> = 0.23$ GeV^2	$<Q^2> = 0.43$ GeV^2	$<Q^2> = 0.97$ GeV^2
b_ϕ(GeV^2)	3.40±0.34	3.84±0.46	3.14±0.38
R	0.03±0.04	0.23±0.08	0.30±0.09
ξ^2	0.16±0.17	0.56±0.18	0.33±0.11
$cos\delta$	0.78±1.20	0.12±0.69	1.21±0.61

two magnetic spectrometers [5], one detecting the electron, the other measuring the two charged kaons from the decay of ϕ. Data were taken at $<Q^2> = 0.23$, 0.43, and 0.97 GeV^2 and $<W> \approx 3.0$ GeV. The measured VMD parameters are shown in Table 1.1. The exclusive LAME experiment [6] extended the cross section measurements to higher Q^2, 0.8 - 4 GeV^2, and covered a range in W between 2 and 3.7 GeV. Their results are consistent with the parameters in Table 1.1, but did not constrain them further because of very limited statistics. The most recent measurement of ϕ electroproduction was made by the ZEUS Collaboration [7]. The R dependence on Q^2 for ϕ meson production is shown in Figure 1.3. One could expect scaling with vector meson mass ($\propto Q^2/M_V^2$), as it is clearly seen by comparing ρ and J/Ψ. Preliminary results of the ZEUS Collaboration for ϕ mesons show no difference from the behavior of the ρ at large Q^2 whereas the CORNELL results [5] are systematicly lower at low Q^2. Both measurements had limited ϕ meson data samples, and the errors are very large [3].

1.2.2 Pomeron Exchange Models of the ϕ Vector Meson Electroproduction

It was pointed out on the basis of quite general arguments [35, 36, 37, 38] that ϕp scattering at low momentum transfer, t, should proceed only through Pomeron exchange, similar to the hadron-hadron diffractive scattering. This is a consequence of the most simple form of the quark model in which the ϕ is made up of only two strange quarks which are barred from resonant reactions with non-strange hadrons. A diagram of the ϕ meson production within the so-called Pomeron exchange model is shown in Figure 1.4. It is generally believed that the underlying mechanism responsible for Pomeron exchange is multiple-gluon exchange. This idea was first investigated within the Bag model [39, 40]. The simplest multiple-gluon exchange requires at least two gluons, since all hadrons are color singlets.

Because of the suppressed meson-exchange production channels, ϕ meson electroproduction is a very useful tool for testing the Pomeron exchange models. The existing ϕ meson production data are shown in Figure 1.5 together with the predictions of two Pomeron exchange models

[3] ZEUS Collaboration analysis of ϕ electroproduction are in preliminary stage.

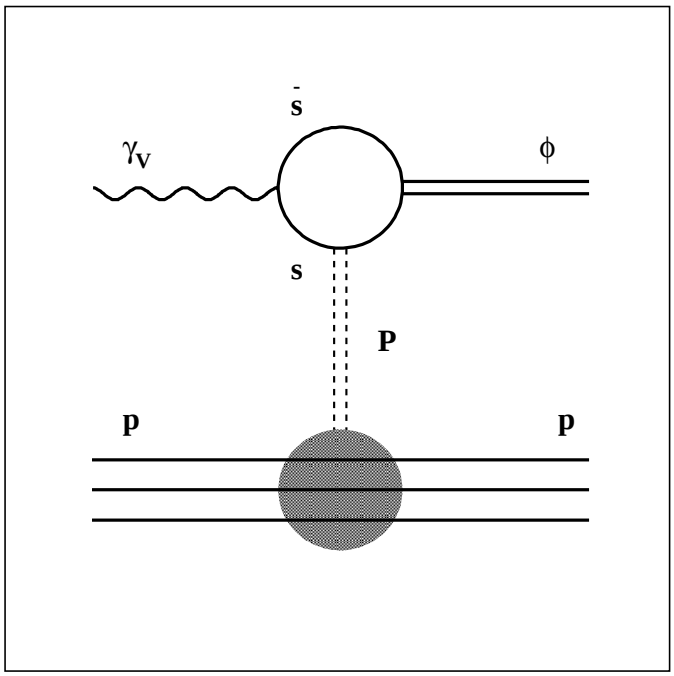

Figure 1.4: Feynman diagram of the ϕ vector meson production within the Pomeron exchange model.

from References [41] and [11].

The open circle and solid triangles are the ZEUS data from References [50, 48] at $W = 70$ GeV, the solid squares are NMC data at $W = 14$ GeV from Reference [51]. The solid circles are electroproduction data from Reference [6]. The open square and star are the photoproduction data at $W \approx 3$ GeV from References [71] and [72], respectively.

The solid green and red lines in Figure 1.5 are the predictions from the Reference [41] for the ρ and ϕ mesons production at $W = 15$ and 70 GeV, respectively. These calculations predict the cross-section to behave as

$$\sigma(W, Q^2 \gg (q_0^2)_X) \propto \frac{1}{1 + [\, Q^2/(q_0^2)_X \,]^2} \,, \tag{1.21}$$

where $(q_0^2)_X$ is a scale that determines the onset of the $(1/\mathrm{Q}^2)^2$ behavior for vector mesons, and $X = \rho, \phi, J/\Psi$ is the index of a vector meson. The value of Q^2, at which the transition to the $(1/\mathrm{Q}^2)^2$ behavior occurs, depends on the scale factor $(q_0^2)_X$ which, in turn, depends on the current-quark mass propagator m_f. The $(1/\mathrm{Q}^2)^2$ behavior is a general feature of the model, independent of the value of m_f. However, the transition from a cross-section that slowly decreases with Q^2 to one that falls off as $(1/\mathrm{Q}^2)^2$, occurs at a value of $(q_0^2)_X$ which increases with current-quark mass m_f. This suggests that the electroproduction cross-sections for heavy-quark vector mesons, produced through Pomeron exchange, reach this $(1/\mathrm{Q}^2)^2$

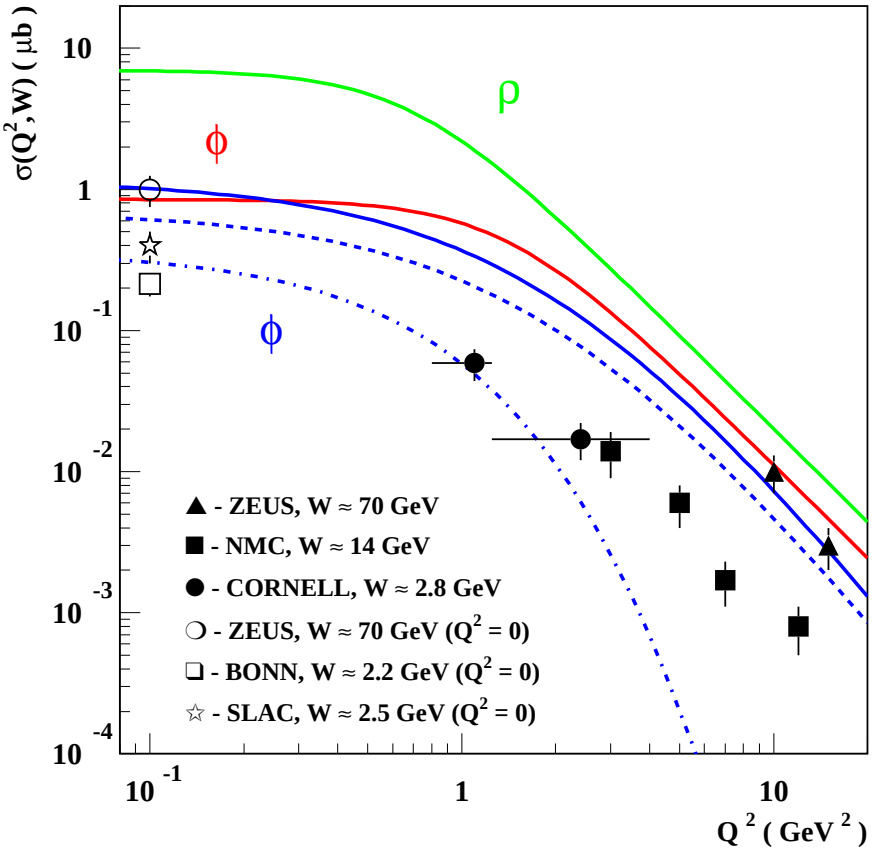

Figure 1.5: The solid red curve is the quark-nucleon Pomeron exchange model prediction of the Q^2 dependence of ϕ-meson electroproduction cross-section at $W = 70$ GeV, and the solid green curve is the prediction for the ρ electroproduction cross-section at $W = 15$ GeV, both from the Reference [41]. The solid, dashed and dot-dashed blue curves are the Pomeron-exchange model predictions for ϕ production at W = 70, 14 and 2.3 GeV, respectively, from the Reference [11]. The plotted data are described in the text.

falloff at larger values of Q^2 than for those of light-quark vector mesons. The prediction of distinguishing between quark substructure of the ϕ and ρ mesons in Q^2 differential cross-sections is shown in Figure 1.5. The calculated Q^2 dependence of ϕ electroproduction at $W = 70$ GeV ($\epsilon = 0.5$) is compared with that of ρ meson at $W = 15$ GeV. For large values of Q^2, the ρ and ϕ meson cross-sections approach the asymptotic, power law $\approx (1/Q^2)^2$. In the model, since $m_s \gg m_u$, the ϕ meson electroproduction cross-section reaches the asymptotic region later, $(q_0^2)_\phi \approx 2.0$ GeV^2, than that of the ρ meson $(q_0^2)_\rho \approx 1.0$ GeV^2. Furthermore, this result suggests that for large enough Q^2 values, the ratio of ρ and ϕ meson electroproduction cross-sections, σ_ϕ/σ_ρ, approaches a constant. The model agrees very well with the ρ and high energy ϕ meson electroproduction data (see Reference [41] and Figure 1.5). But the New Muon Collaboration ϕ meson data taken at $W = 14$ GeV lie systematically lower [4].

[4]The calculations within the Pomeron exchange model, from References [41] and [11], both do not describe

The solid, dashed and dot-dashed blue lines in Figure 1.5 are the predictions of the ϕ meson electroproduction cross sections from the References [11] at W = 70, 14 and 2.3 GeV, respectively. The model is described in Reference [10]. These calculations are consistent with those from the Reference [41] and extend the predictions to low W. The model predicts a W dependence of the cross section similar to that for the hadron-hadron diffractive processes at low momentum transfer t [9, 10]

$$\frac{d\sigma}{dt}\,(t=0) \propto \left(\frac{s}{s_0}\right)^{2(\alpha_P(0)-1)} \propto W^{0.32}\,, \quad W=\sqrt{s}\,, \tag{1.22}$$

and successfully describes the data at low and high W from References [6] and [50, 48], respectively. The calculations at low W show that the ϕ meson cross-section falls faster with increasing Q^2 because of increasing t_{min} in kinematicaly limited phase space.

1.2.3 Space-Time Picture

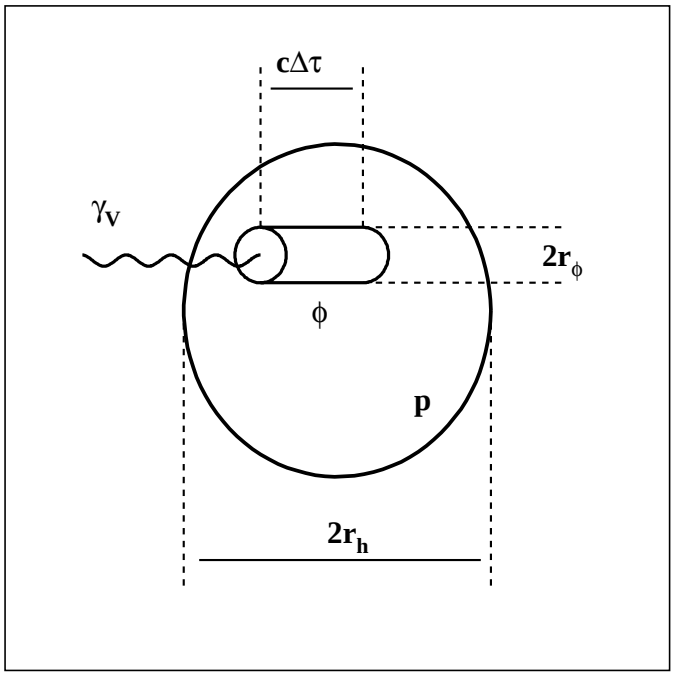

Figure 1.6: Space-time diagram of the $\gamma_V p$ scattering through the conversion of virtual photon into the virtual ϕ meson inside the target proton.

Another important subject to study in diffractive production of ϕ mesons is the t-slope dependence on Q^2 and $\Delta\tau$. Here we try to describe pedagogically, in a simple optical model, the qualitative picture of the vector meson diffractive scattering. A sketch of the process is

the NMC data at W = 14 GeV. For the NMC data interpretation see discussion in References [7] and [41].

shown in Figure 1.6. The virtual photon, produced by the scattered electron, is converted into the virtual ϕ vector meson (of radius r_ϕ), which diffractively interacts with the proton (of radius r_h) during an interaction time $\Delta\tau$. In an optical model, the intensity of scattered light from a circular aperture as a function of angle is given by

$$\frac{I}{I_0} \approx 1 - \frac{R^2}{4}(k\theta)^2 \,, \tag{1.23}$$

where k is the wave number of the photons, and R is the radius of the aperture. For the hadron-hadron elastic scattering

$$\frac{d\sigma/dt}{(d\sigma/dt)_{t=0}} = exp\ (bt) \approx 1 - b\ (p\theta)^2 \,, \tag{1.24}$$

where p is the momentum of the incident hadron. Comparison of Equations 1.23 and 1.24 leads to a relationship between the radius of interaction, R_{int}, and the t-slope parameter:

$$b = \frac{R_{int}^2}{4} \tag{1.25}$$

In the case of a finite-size vector meson diffractive scattering on the nucleon

$$R_{int} \propto [\ r_h + r_{VM}(Q^2)\ ] \,, \tag{1.26}$$

where r_h and r_{VM} are the radii of the nucleon and vector meson, respectively.

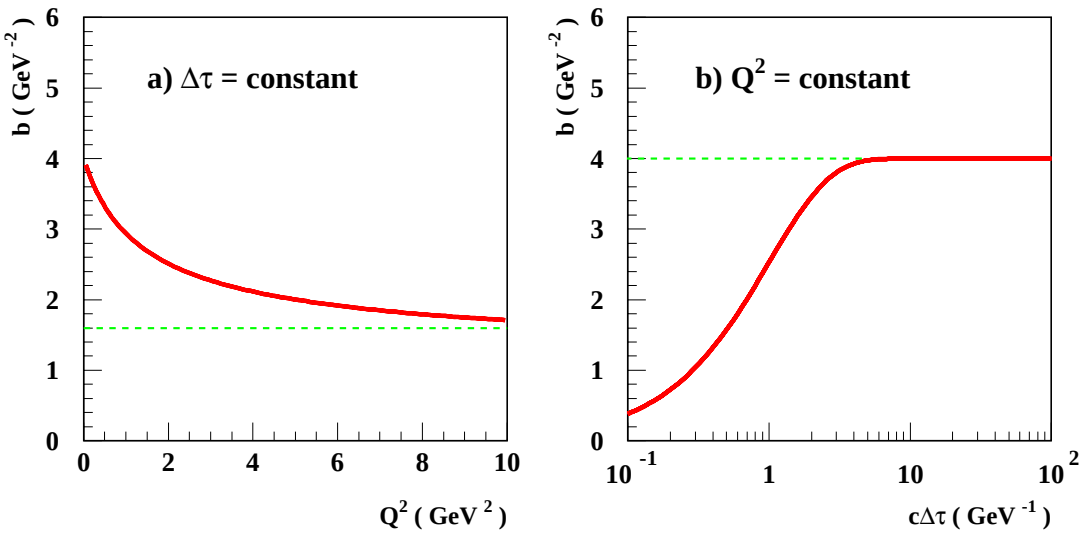

Figure 1.7: a) The expected t-slope parameter, b, dependence on Q^2 (the solid red line) with a fixed $\Delta\tau$. The dashed green line is the asymptotic value of b, proportional to $(r_h + r_\phi^{min})^2$. b) The expected t-slope parameter, b, dependence on $\Delta\tau$ (the solid red line) with a fixed Q^2. The dashed green line is the asymptotic value of b, proportional to R_{int}^2.

It has been argued that with increasing Q^2 the radius of the virtual photon, converted into a ϕ meson, will shrink [1], and a corresponding decrease of b should be observed. Because of virtuality of the vector meson, the decrease of the interaction region should also occur if the formation time $\Delta\tau$ for the vector meson is less than the time it takes the photon to transverse a nucleon $c\Delta\tau \approx 2r_h \approx 1$ fm. [5] Therefore, the t-slope parameter reflects some combined size of the virtual photon, converted into the virtual ϕ meson, and size of the proton, scaled with the interaction time:

$$b(Q^2) \propto \frac{1}{4}\,(1 - e^{-c\Delta\tau/r_h}) \cdot (\, r_h + r_\phi(Q^2))^2 \tag{1.27}$$

Under the VMD model assumption [1] the r_ϕ can be written as

$$r_\phi \approx \frac{cM_\phi}{M_\phi^2 + Q^2}\,, \tag{1.28}$$

and an intuitive quark model approach [8] predicts

$$r_\phi \approx \frac{r_h M_\phi}{\sqrt{M_\phi^2 + Q^2}} \tag{1.29}$$

In Figure 1.7a we show the expected b dependence on Q^2 with a constant $\Delta\tau$ (the solid red line) [6]. The dashed green line is the asymptotic value of b, proportional to $(r_h + r_\phi^{min})^2$, where r_ϕ^{min} is the minimum radius of shrunken ϕ meson. Figure 1.7b illustrates the expected t-slope parameter dependence on $\Delta\tau$ with a constant Q^2 (the solid red line). The dashed green line is the asymptotic value of b, which is proportional, in this case, to $(r_h + r_\phi)^2$.

Indeed, the expected behavior of b with Q^2 and $\Delta\tau$ was observed and well measured in ρ photo- and electroproduction [6, 2], shown in Figure 1.8 and Figure 1.9 (the black symbols), respectively. However, the previous measurements of ϕ meson photo- and electroproduction, Figure 1.8 and Figure 1.9 (the green symbols), are consistent with no dependence of the t-slope parameter no on Q^2, neither on $\Delta\tau$ [1, 5]. This difference in the ρ and ϕ mesons production is a longstanding and non-understood mystery.

1.3 Hard Production Mechanisms

ρ Production. Previous measurements at relatively high Q^2 show that there are kinematic regions where exclusive production of vector mesons is a hard scattering process. The European Muon Collaboration (EMC) [2] has measured exclusive ρ vector meson production

[5] For such small formation times the whole qualitative VMD picture may be in doubt [1].

[6] Since the entire range of the $c\Delta\tau$ for this experiment is below 1 fm, we used for analysis the expression for the vector meson radius, r_ϕ, from Equation 1.29.

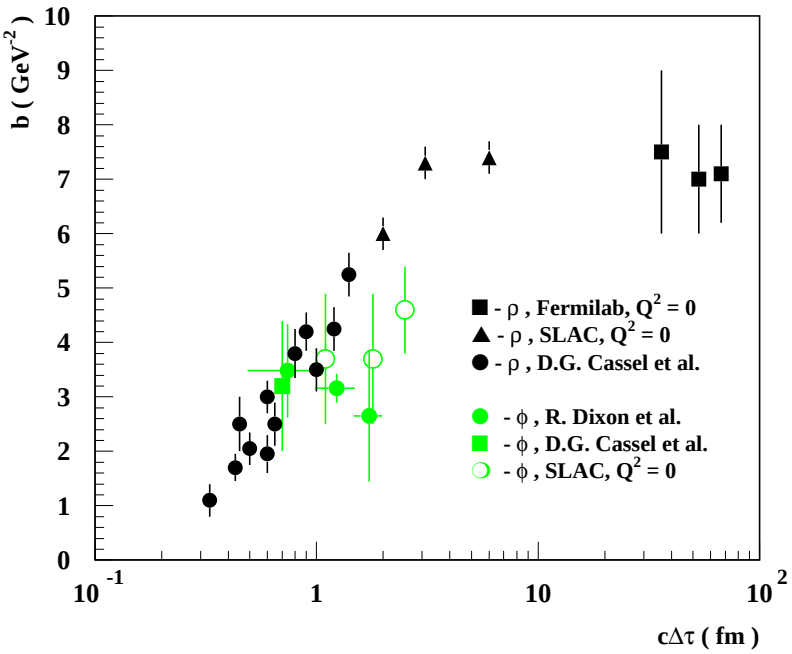

Figure 1.8: The t-slope parameter dependence on $c\Delta\tau$ for the photo- and electroproduction of ρ and ϕ mesons. The ρ data show a clear decrease of b with decreasing $c\Delta\tau$ below 2 fm, while ϕ production data are consistent with a constant behavior of b.

with muons, i.e. $\mu p \rightarrow \mu p \rho$ at $Q^2 \geq 1.0$ GeV^2. Their data indicate that in this regime, the soft hadron-like properties of the photon have disappeared and the virtual photon acts as pure electromagnetic probe of the nucleon structure. A signature for the departure from the diffractive nature of the reaction mechanism is given by: 1) The $\rho \rightarrow \pi^+\pi^-$ decay distributions shown in Figure 1.10. The measured angular distributions are consistent with pure $cos^2\theta$ distribution (more pronounced for 280 and 200 GeV data than for the 120 GeV data). From Equation 1.20 this implies a very large value of R within the VMD model or the violation of SCHC. 2) The $R = \sigma_L/\sigma_T$ derived from cross-section measurements [2] is not consistent with that extracted from helicity angular distributions under the VMD assumption. 3) The observed increase of the longitudinal polarization of ρ with increasing Q^2 appears together with the decrease of the slope parameter b. And, since small values of b are characteristic of hard scattering processes, it is likely that the longitudinal polarization is connected with hard scattering. Their analysis suggests that the data can not be described by the VMD model with SCHC, and that hard production mechnisms start dominating at values of $Q^2 \geq 1$ GeV^2.

Recent helicity analysis of HERA ρ meson electroproduction data [61], performed using 15-Parameter Helicity-Angle fit, also indicate the violation of SCHC in the high W and Q^2 regime (the linear combination of matrix elements, corresponding to the helicity violating amplitudes, $r^5_{00} > 0$), which was conserved at low values of Q^2. These results set limits on VMD model range of application and highlight the necessity to understand the reason for

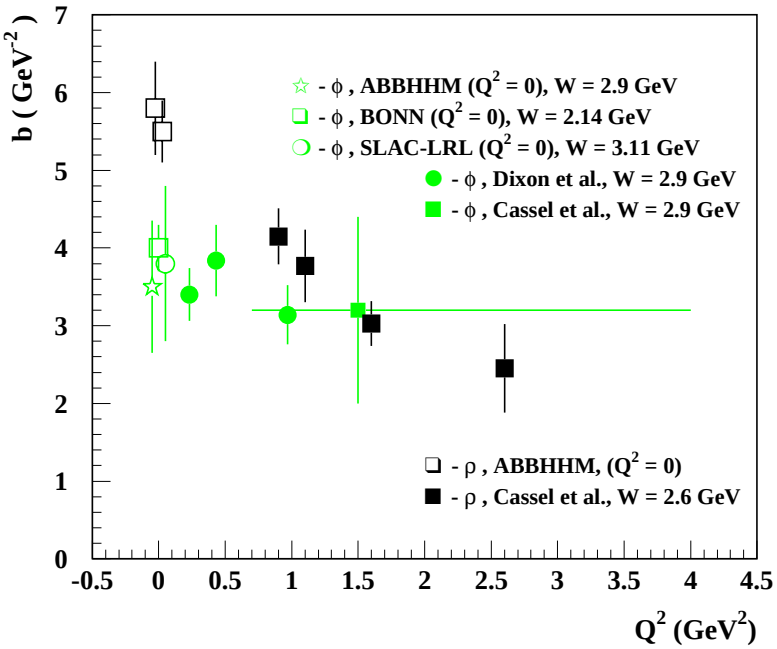

Figure 1.9: The t-slope parameter dependence on Q^2 for the ρ and ϕ mesons production. The ρ data show a clear asymptotic decrease of b with increasing Q^2, while ϕ production data are consistent with a constant behavior of b.

the violation.

ϕ Production. Inclusive ϕ photoproduction measurements [3] for photon energies between 20 and 70 GeV also show that the ϕ angular decay distribution is a sensitive measure of the onset of non-diffractive production mechanisms. The diffractive character of the reaction mechanism is in the $sin^2\theta$ distribution in Figure 1.11 for $x_F \geq 0.7$, where x_F is the momentum of the vector meson along the photon beam relative to the maximum allowed in the virtual photon-hadron center-of-mass. Hard processes, described within the quark fusion model, are indicated by a very different angular distribution for $0.1 \leq x_F \leq 0.7$. Interpreted as the onset of hard photo-knockout of a $s\bar{s}$ pair, the data suggest about a 20 - 30% $s\bar{s}$ nucleon component (see Section 1.4). The lack of substantial ϕ-nucleon coupling makes it a useful indicator of the onset of hard processes. However, no previous experiment has accumulated enough data to measure the details of ϕ photo- or electroproduction with the accuracy required for a reliable indication of this reaction mechanism.

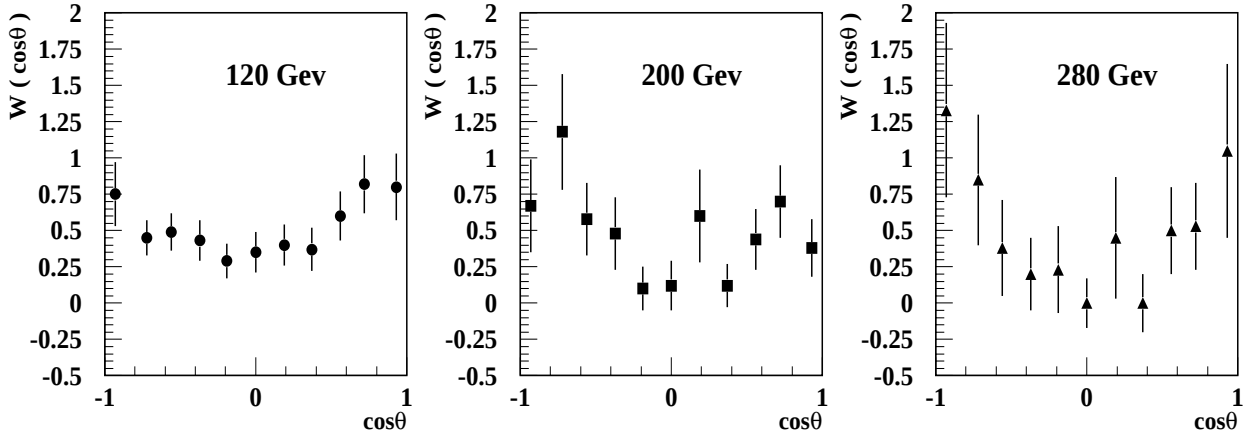

Figure 1.10: Decay distributions of $\rho \to \pi^+\pi^-$ in exclusive muon-production from Reference [2] show primarily a $cos^2\theta$ distribution.

1.4 ϕ Production by $s\bar{s}$ Knockout

Electromagnetic production of ϕ mesons is simple relative to other vector mesons because its valence quark structure is almost pure $s\bar{s}$ (see Appendix A). Unlike the case for ρ or ω mesons production, quark exchange mechanisms should be strongly suppressed. This OZI suppression occurs at a level between 0.1 - 5% of OZI allowed reactions. For example, $\Gamma_{\phi\to\rho\pi} \approx 0.6$ MeV, less than 0.6% of typical hadronic widths. Measurement of a ϕ component arising from a ϕ-N interaction significantly greater than the 5% expected from OZI violation could be indicative of an $s\bar{s}$ component in the nucleon. A number of unexpected experimental results may be explained by assuming that the nucleon $s\bar{s}$ sea component is of the order 10-20% [21, 22]:

1) The results from deep inelastic scattering of polarized muons on polarized protons [2];

2) νp elastic scattering [23];

3) the π-nucleon σ term, obtained by extrapolating low energy π-N scattering to the unphysical pion pole [24, 25, 26];

4) OZI suppressed reactions are at least of factor 3 more than expected in $p\bar{p}$ annihilation: $(p\bar{p} \to \phi\pi^+\pi^-)/(p\bar{p} \to \omega\pi^+\pi^-) = 2$ - 3% compared to theoretical expectations of 0.1 - 0.7% [27];

5) fits to the isoscalar Dirac nucleon electromagnetic form factor require a ϕ vector meson component with a large nucleon coupling: $g_1(\phi NN)/g_1(\omega NN) \sim 0.4$ [28].

An independent tool for testing nucleon's strange quark component is ϕ electroproduction. Schematically this process is shown in Figure 1.12. The rate of ϕ electromagnetic production on a nucleon via photon scattering from a virtual $s\bar{s}$ pair in the proton has been estimated

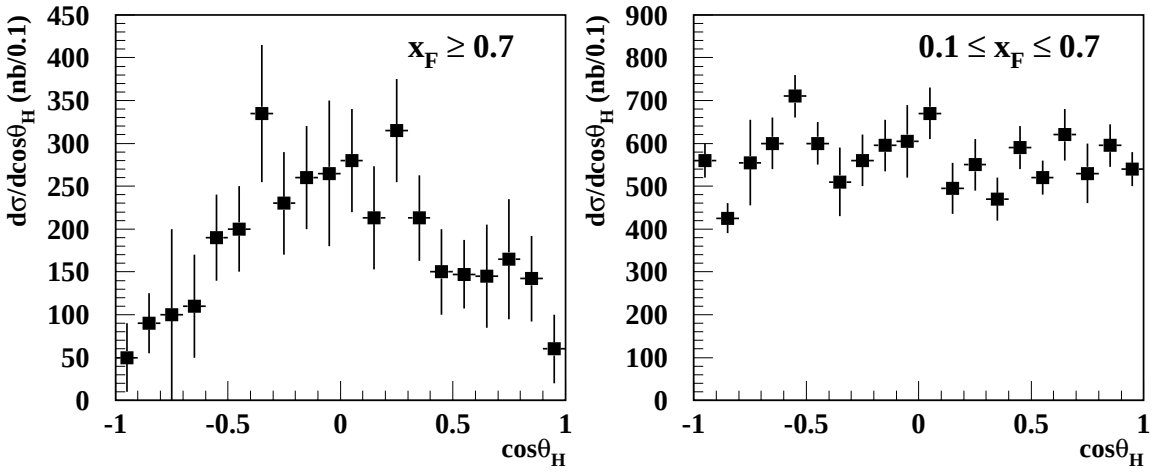

Figure 1.11: Decay of $\phi \to K^+K^-$ in inclusive photoproduction from Reference [3]. The angular distributions show that different production mechanisms are responsible for ϕ production in different regions of x_F.

by several authors [29, 30, 31]. The calculations indicate that the knockout and diffractive contributions to ϕ production are of the same magnitude when one assumes an admixture of 10 - 20% strange quarks in the nucleon. The calculations assume the $s\bar{s}$ pair to be in a relative 1s-state with respect to each other inside the proton just as they are in the ϕ. The spin of the $s\bar{s}$ pair is taken to be either 0 or 1 [4]. However, only the spin zero component survives because of cancellations between $\gamma_V s$-quark and $\gamma_V \bar{s}$-quark contributions. Spin 0 is also expected from C-conjugation and hyperfine splitting arguments. The parity of the pair is negative, since the intrinsic parity of the s-quark is opposite to that of $\bar{s}$-quark. Thus, ϕ production due to $s\bar{s}$ knockout is calculated through the exchange of a pseudoscalar meson in the t-channel.

Angular Correlations. Pseudoscalar exchange provides a particularly simple signal in the $\phi \to K^+K^-$ decay distribution if evaluated in the Gottfried-Jackson frame (see for details Appendix B):

$$W_{PS}^{GJ}(cos\theta, \psi) \;=\; \frac{3}{8\pi} sin^2\theta(1 + \epsilon P_\sigma cos2\psi) \tag{1.30}$$

The angle θ is the polar angle of the K^+ and $\psi = \phi_H - \Phi$ is the azimuthal angle relative to the electron scattering plane (*not* the hadron production plane, see Figure 1.1). Because a spin 0 object is exchanged, the polarization of the ϕ cannot depend on the orientation of the hadron production plane. Furthermore, the ϕ has no longitudinal spin component. The $\sin^2\theta$ term arises from ϕ's polarized in the ± 1 helicity state. The $\cos 2\psi$ term is due to interference between the two transverse helicity states. For pseudoscalar meson exchange (unnatural parity), P_σ = -1; for the case of diffraction (natural parity), $P_\sigma = +1$. The $\cos 2\psi$

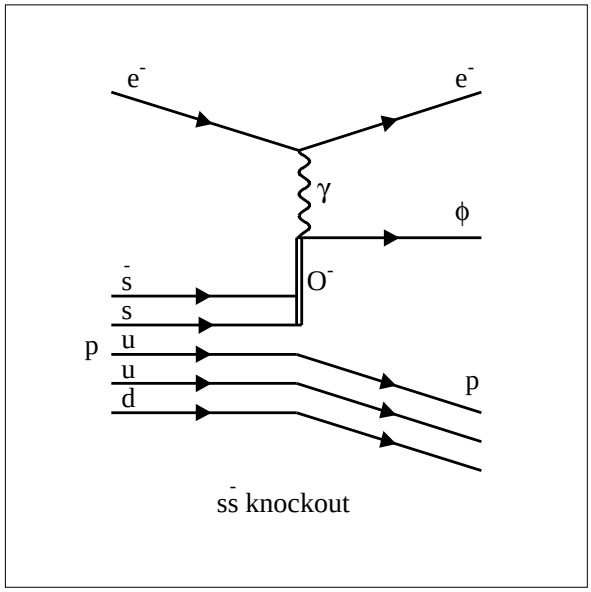

Figure 1.12: Feynman diagram of the $s\bar{s}$-knockout production mechanism.

term, a key to identifying pseudoscalar meson exchange, is proportional to the transverse linear polarization of the photon, either real or virtual. In the helicity frame (Figure 1.1) the distribution in Equation 1.30 is modified in a predictable way as a function of the momentum-transfer t, as given in Appendix B, and yields a second key to identifying the pseudoscalar exchange mechanism. Since pseudoscalar exchange is incoherent with helicity-conserving diffraction [56], the decay distribution W(cosθ_H, ψ, Φ) is a linear combination of pseudoscalar exchange and diffraction with relative fractions f_{PS} and f_D respectively:

$$W(cos\theta_H, \psi, \Phi) \;=\; f_{PS}\, W^H_{PS}(cos\theta_H, \psi, \Phi; t) + f_D\, W^H_D(cos\theta_H, \psi; \xi^2, cos\delta)\,. \quad (1.31)$$

Here the dependencies on the kinematic variable (t) and and parameters of the model (ξ^2, $cos\delta$) are shown explicitly. A multipole moment analysis with respect to these angles permits one to test the model and determine the combinations of the matrix elements.

There is very little data of ϕ production with linearly polarized photons [32, 33]. Although the results are in general agreement with Vector Meson Dominance, the measured value of one density matrix , $\rho^1_{1-1} \approx 0.18 \pm 0.13$, was notably low compared to an expected value of 0.5. Within the quoted error bars, the value of ρ^1_{1-1} and ρ^2_{1-1} could indicate a pseudoscalar exchange cross section component as large as $\sim 30\%$ of the total. There is only one measurement of helicity angular distributions of ϕ electroproduction [5]. Finally there is a very low statistics experiment measuring ϕ production by muons [34]. All experimental results generally agree with the expectations of the VMD model for ϕ production. However, the sensitivity of the measurements was quite limited, and both models, VMD and production through pseudo-scaler exchange, which contain several parameters, are able to accommodate

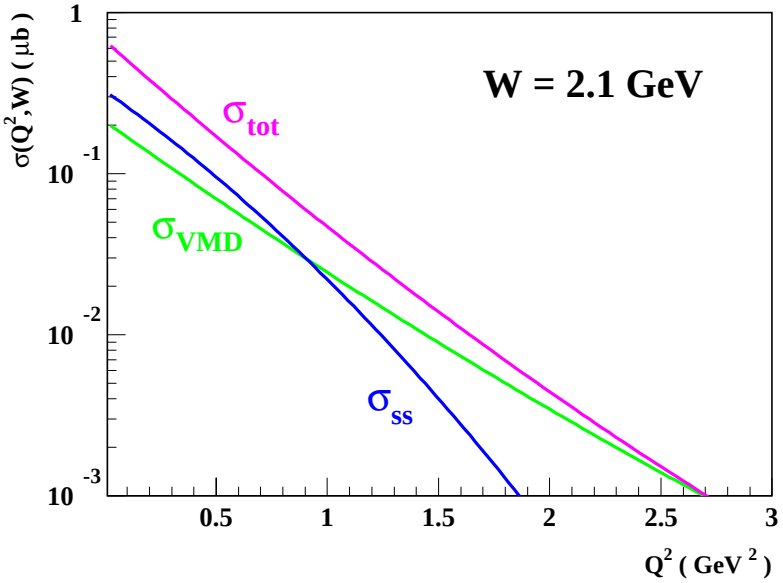

Figure 1.13: Predictions of the cross-section dependence on Q^2 by constituent quark and VMD models for $s\bar{s}$-knockout (blue line) and diffractive (green line) production mechanisms, respectively [4]. The solid magenta line is the sum of both. Calculations are made at W = 2.1 GeV.

a broad range of results.

Cross-Section Calculations. There are theoretical predictions of $\sigma(Q^2,W)$ for $s\bar{s}$-knockout and diffractive mechanisms [4], calculated within a constituent quark and the VMD models, respectively. This simple quark model is not expected to be reliable either far above the ϕ-production threshold ($W \gg M_p + M_\phi = 1.96$ GeV) or for large Q^2 (≥ 1 GeV^2) (see for details Reference [4]). The calculations were made under assumptions that the strangeness content of the proton is about 20 % ($B^2 = 0.2$), the $s\bar{s}$-pair are in a relative $1s$-state with respect to each other inside the proton just as they are in ϕ. In Figure 1.13 the calculated Q^2-dependence of $\sigma(Q^2,W)$, at W = 2.1 GeV, is shown for both diffractive and knockout mechanisms. The diffractive result falls approximately exponentially for $Q^2 \geq 1$ GeV^2, the $s\bar{s}$-knockout prediction falls somewhat faster with Q^2. All of the cross-sections are predicted to increase as W moves away from the production threshold because of the increased available phase space. However, as W continues to increase (beyond $\simeq$ 2.3-2.4 GeV) the knockout cross-section begins to decrease because of the fall-off of the high-momentum tail of the quark wavefunctions. The diffractive cross-section becomes approximately independent of W for W $\geq$ 2.4 GeV. This calculations suggest that experiments intending to look for the $s\bar{s}$-knockout ϕ production mechanism should be done just above threshold in W.

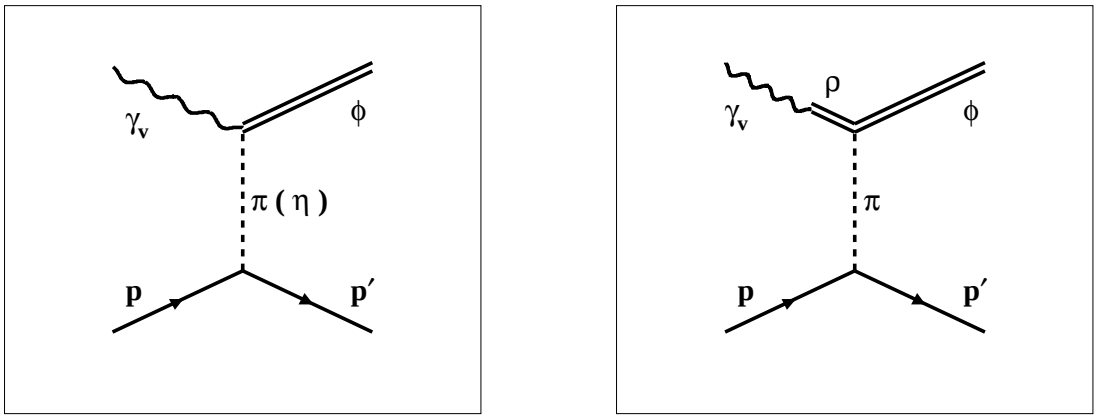

Figure 1.14: Feynman diagrams of ϕ production through the exchange of π and η mesons in t-channel.

1.5 Meson Exchange Production Mechanisms

There is a small admixture of nonstrange quarks in ϕ meson that could modify the simple view of the diffractive production mechanism dominace [1]. Indeed, electroproduction of ϕ meson can be realized through the t-channel exchange of π and η mesons. Feynman diagrams of these processes are illustrated in Figure 1.14.

The calculation of the diffractive ϕ and ρ mesons photoproduction and the π/η meson-exchange contribution were made and compared in Reference [41]. Exclusive diffractive processes on the nucleon are investigated within a model in which the quark-nucleon interaction is mediated by Pomeron exchange and the quark substructure of the mesons. The lowest order of the meson-exchange contributions was derived from the phenomenological Lagrangian of Reference [43]. The calculated cross-sections describe the experimental data well, and are shown together in Figure 1.15. We see from Figure 1.15a that the W dependence of meson-exchange is very different than that of Pomeron exchange. The difference suggests that these two exchanges may be modeling very different aspects of QCD. For example, one might view meson exchange as a phenomenological representation of the exchange of correlated quark-antiquark pairs. Its strength, therefore, depends strongly on the flavor structure of the hadrons involved. Therefore, it is not surprising that meson-exchange contributions to ϕ-meson photoproduction are significantly less than those to ρ-meson photoproduction; the lack of valence-s quarks in the nucleon tends to suppress direct quark exchange [7]. However, the meson exchange contributions become comparable to the Pomeron-exchange scattering at low energies, even for ϕ photoproduction. The predictions for the Pomeron-exchange and meson-exchange in ϕ photoproduction in the differential cross-section $d\sigma/dt$ at $W = 3$ GeV are shown in Figure 1.15b. It is very interesting that Pomeron exchange (dot-dashed

[7] It is also consistent with the electroproduction model calculations [58, 62].

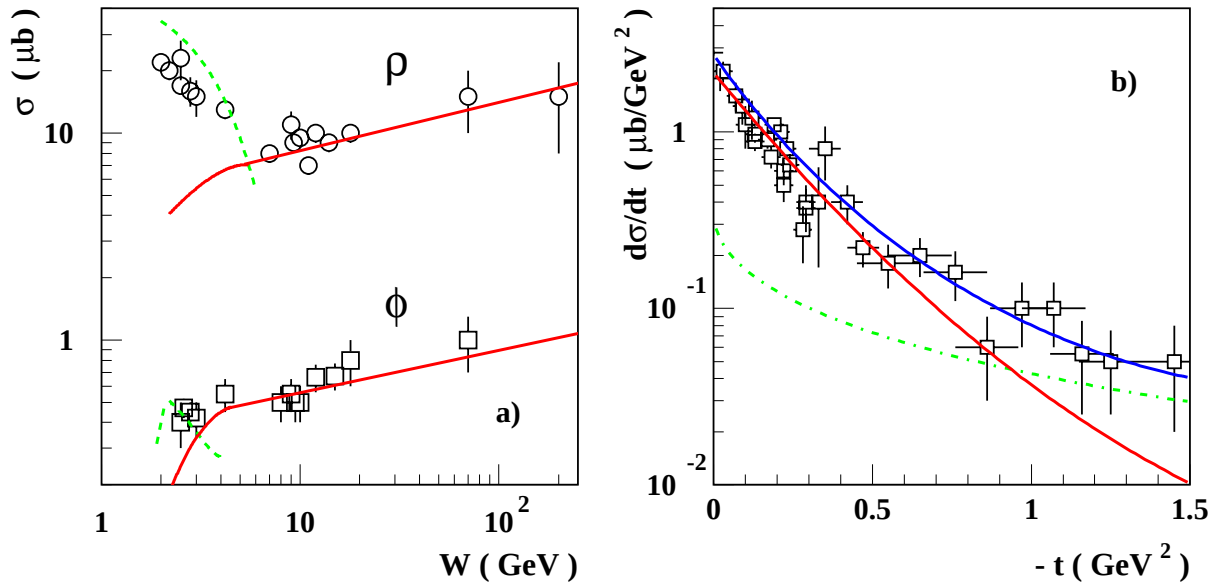

Figure 1.15: a) Energy dependence of ρ and ϕ photoproduction cross-sections. The red solid curve are the predictions for quark-nucleon Pomeron-exchange interaction, and the dashed green curves are the predictions of the meson-exchange model [41]. The ρ-meson data (circles) are from References [32, 34, 44, 45, 46, 47]. The ϕ-meson data (squares) are from References [32, 46, 48, 49]. b) The differential cross-section for ϕ-meson photoproduction ($Q^2 = 0$) for $3.0 \leq W \leq 3.5$ GeV. The red curve is the contribution due to the Pomeron-exchange interaction, the green dot-dashed curve is the contribution due to π and η exchange at W = 3 GeV, and the blue curve is the sum of these. The data (squres) are from References [15, 16, 49].

green curve) is dominant in the forward peak while π and η exchanges contribute a flatter background at low t and start to dominate at momentum transfer above 1 GeV^2. It is not clear if this picture holds also in ϕ meson electroproduction [42].

1.6 Summary

In this Section we summarize the objectives for this experiment:

a. t-slope Dependence. The analysis of the t-slope parameter dependencies on momentum transfer and interaction time are quite simple after the ϕ meson channel is identified. It is determined from the t-slope parameter, b_ϕ, of the $d\sigma/dt'$ distribution at low t' for different values of Q^2 and $\Delta\tau$, using the fitting function:

$$\sigma_{t'} \quad = \quad A_\phi \; exp(-b_\phi t') \; , \tag{1.32}$$

where $t' =\mid t - t_{min}(Q^2) \mid$. If the ϕ production has the expected features, the data must show a decrease of b_ϕ with increasing Q^2 and decreasing $\Delta\tau$, as shown in Figure 1.7.

The shape of the differential cross-section, $d\sigma/dt'$, is also important in connection with the theoretical predictions, described in Section 1.5. If the π and η meson exchange contributions are significant in our kinematic regime, we should be able to see it as slope change at high values of t'.

b. Cross-Sections. It is very interesting to compare the existing theoretical calculations of ϕ electroproduction cross-section dependence on Q^2 with the experimental data. The VMD model, the Pomeron exchange and $s\bar{s}$-knockout models predict very different behavior of $\sigma(Q^2)$. This may facilitate a conclusion about the dominant ϕ production mechanism and validity of theoretical models.

c. Angular Distributions. The $\phi(1020)$ is a spin 1 object. Its decay into K^+K^-, two spin-0 mesons is "self-analyzing": the angular distributions provide a complete description of the ϕ polarization. The choice of coordinates, characteristic of each production mechanism, makes this polarization easily analyzable. We are interested, then, in measuring the decay angles of an identified kaon in the ϕ rest frame (s-channel helicity frame, see Figure 1.1). These are the polar angle θ_H, the azimuthal angle ϕ_H and Φ, the angle between the electron scattering and hadron production planes. The helicity frame simplifies the description of diffractive scattering (Equation 1.19), so this frame was chosen for the analysis. From the measured angular distributions we can derive the VMD model parameters [8].

[8] At present, we can not draw any conclusion about $s\bar{s}$-knockout production channel from the helicity angular distribution because of statistically limited data sample.

Chapter 2

Experimental Setup

2.1 Continuous Electron Beam Accelerator Facility

The Continuous Electron Beam Accelerator Facility (CEBAF) is located at the Thomas Jefferson National Accelerator Facility (Jefferson Lab), Newport News, Virginia. Its electron accelerator is based on super-conducting RF cavities operated in a continuous wave (CW) mode. A schematic of the machine is shown in Figure 2.1. Two parallel linacs in a "race track" configuration boost the beam energy by 800 MeV for each turn. The beam is recirculated five times to reach an initial maximum energy of about 4 GeV. At the heart of the machine are the five niobium cavities per cryomodule, which have a minimum gradient of 5 MeV per meter. The cavities perform significantly better than the specifications, therefore providing the technical basis for a future energy upgrade. The machine can deliver electron beams to three experimental areas (Hall A, B, C) at either the same energy, or at multiples of 1/5 of the end-point energy. Due to the virtual lack of synchrotron radiation , the energy spread in the beam is $\Delta E/E \leq 10^{-4}$.

Beams can be extracted at each recirculation, thus allowing the operation of the experimental halls with simultaneous beams of different, though correlated energies. The 1.497 GHz RF structure allows simultaneous beams to be delivered to each hall at a frequency of 499 MHz. The micro bunches can also be loaded with different electron densities, which provide the basis for operating the experimental areas with currents spanning a large dynamic range. In addition, a polarized electron gun can be operated in parallel with the standard thermionic unpolarized gun.

The end stations are equipped with spectrometers for complementary experimental programs. Hall C contains two magnetic spectrometers of medium resolution with $\Delta p/p \leq 10^{-3}$, but different maximum momenta: the High Momentum Spectrometer (HMS) has a maximum momentum of 7 GeV/c, and the Short Orbit Spectrometer (SOS) has a maximum momenta of 1.8 GeV/c, respectively. Hall A houses two High Resolution Spectrometers

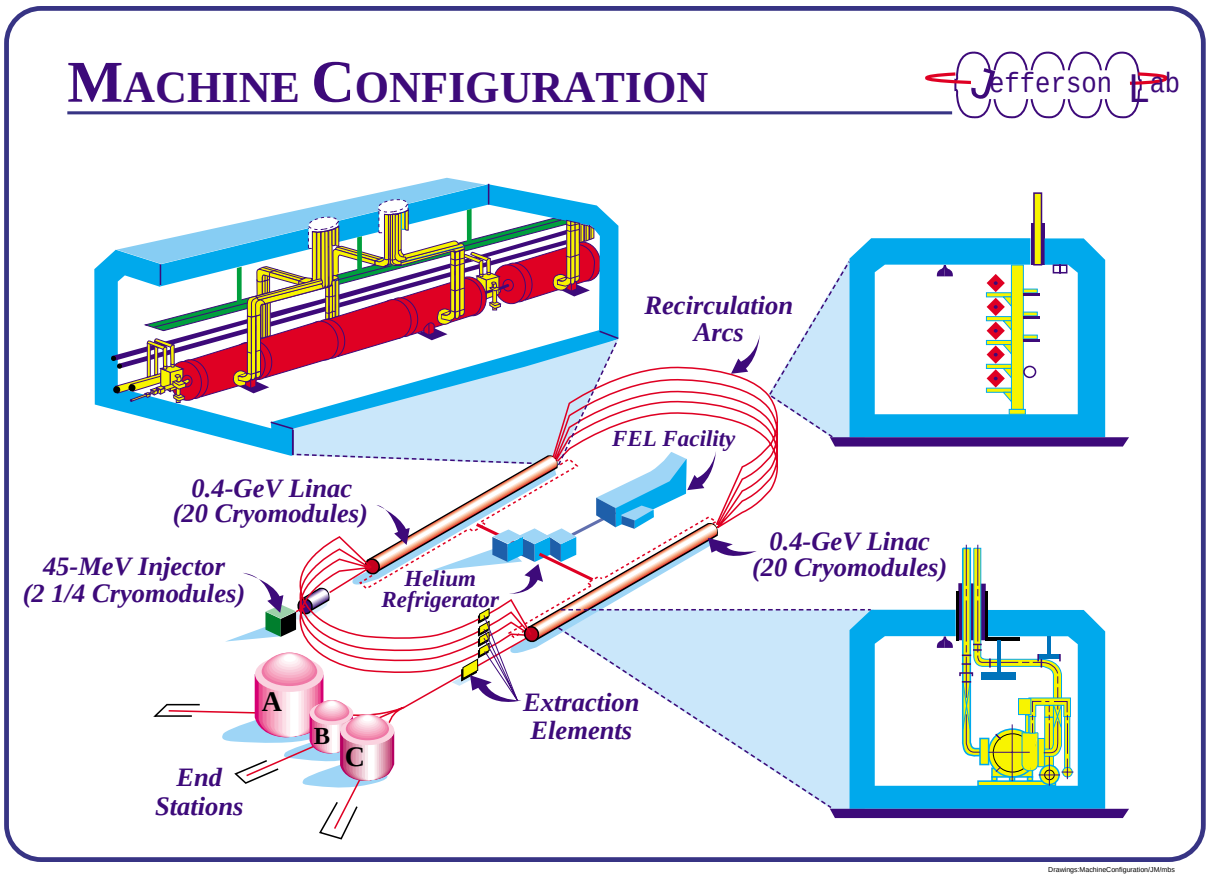

Figure 2.1: CEBAF configuration.

(HRS) with $\Delta p/p \leq 10^{-4}$, and a maximum momentum of 4 GeV/c, instrumented for electron and hadron detection. Hall B houses the CEBAF Large Acceptance Spectrometer (CLAS), dedicated to the exclusive multi-particle final state measurements. The CLAS detector is described in more detail below.

2.2 CEBAF Large Acceptance Spectrometer, Experimental Hall B

2.2.1 General Description.

Hall B of Jefferson Lab is equipped with a near 4π acceptance detector, the CEBAF Large Acceptance Spectrometer (CLAS), as shown in Figure 2.2. Its main mission is to carry

out exclusive measurements that require simultaneous detection of several particles in the hadronic final state at limited luminosity ($\sim 10^{34}$ cm^2/sec).

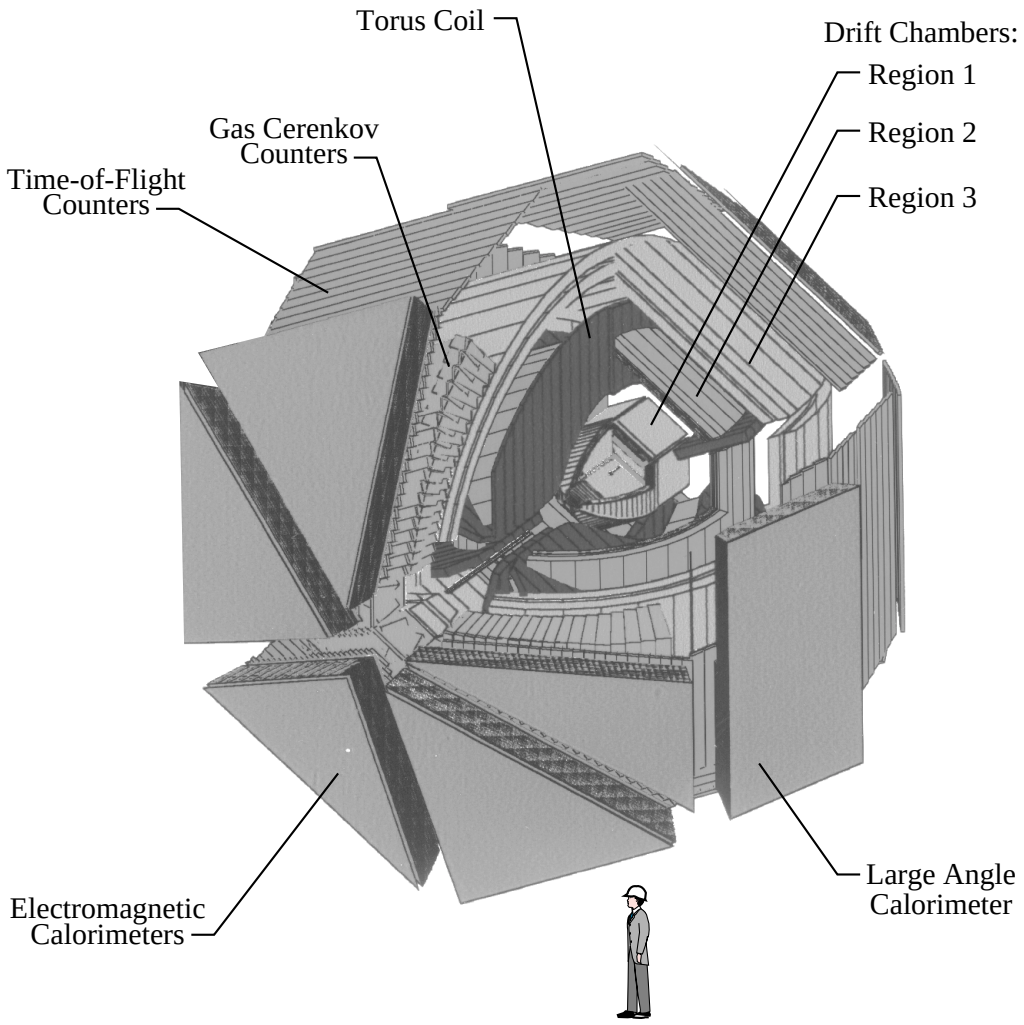

Figure 2.2: CLAS detector layout

The magnetic field in the CLAS has a toroidal configuration generated by six iron-free superconducting coils arranged around the beam line to produce a field, primarily in azimuthal direction about the beam, with a maximum intensity of about 2 Tesla. The size (about 5 meters long and 2.5 meters wide) and the shape of the coils were chosen to optimize them based on the physics program for fixed target operation using electron beams of a few GeV. The spectrometer consists of Drift Chambers (DC) to determine the trajectories and momenta of charged particles, threshold Cherenkov Counters (CC) for the electron identification, scintillation counters (SC) for the Time-of-Flight (TOF) measurement of charged particles, and Electromagnetic Calorimeters (EC) to identify electrons and to detect photons and neutrons. To facilitate pattern recognition and track reconstruction at high luminosity,

the segments are individually instrumented to form six independent magnetic spectrometers, located symmetrically around the beam line (Figure 2.2). All detectors may be used to build the trigger configuration for the reactions of interest. Hall B also includes a bremsstrahlung photon tagging facility so that CLAS can investigate real as well as virtual photon processes.

2.2.2 Drift Chambers

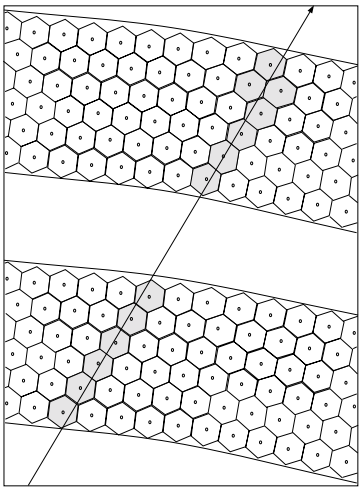

Figure 2.3: Representation of one portion of a drift chamber sector showing two superlayers each consisting of six layers of drift cells. The hexagonal granularity is drawn to guide the eye. The cells are electrostatic boundaries determined by field wires located at each of the corners of the hexagons. Not shown are the guard wires that surround the perimeter of each superlayer. A charged particle is shown traversing the drift chamber package, with shaded areas indicating hit wires.

The Drift Chambers of CLAS [53] include 18 separate chambers placed in three radial locations in each of the six sectors (see Figures 2.2). The radial locations are referred to as "Regions". The Region One (R1) chambers surround the target in an area of low magnetic field, the Region Two (R2) chambers are larger than those of R1 and are situated between the magnet coils in an area of highest magnetic field near the point of maximum track sagitta, and Region Three (R3) chambers are the largest tracking devices, located radially outward of the magnet. The wire midpoints are arranged in "layers" of concentric circles. For pattern recognition and tracking redundancy, the wire layers are grouped into "superlayers", one axial to the magnetic field and the other tilted at a 6° stereo angle to provide azimuthal information. Each superlayer consists of six layers of drift cells as shown in Figure 2.3. The "brick-wall" pattern of hexagonal drift cells gives a good resolution of left-right ambiguity and a reasonable approximation to the ideal circular cells in which the drift time to distance relation is independent of entrance angle. With this wire arrangement and a high magnetic field setting average momenta resolutions for charged particles below

1% is expected. A 90%-10% argon-CO_2 ionizing gas mixture is used for several reasons: it is non-flammable, the gas has fairly high saturated drift velocity (greater than 4 cm/μsec) and it has an operating voltage plateau of several hundred volts before breakdown. This 90%-10% mixture provides efficiency above 99%, about 350 μm average space resolution and 1 μs collection time within one sector. The DC calibration procedure is based on determination of a time-to-distance function, the conversion of measured drift time to the distance from the anode wire of a cell. During this experiment the overall DC resolution was close to 1000 μm, which include sector-to-sector chamber alignment.

2.2.3 Cherenkov Detector

The threshold Cherenkov detector of CLAS consists of six nominally identical counters (CC), one per sector. Each counter covers the angular range from 8° to 45° in polar angle, θ, with the full coverage of CLAS in azimuthal angle ϕ (see Figure 2.2). The mechanical structure of each counter includes two side walls, which are in the planes of the CLAS magnet coils, a partial cylindrical piece at the vertex near the beam line, and a "45-degree wall" made of GreySeal, a composite material that is both strong and light. The entrance window material is a sandwich of 10 μm mylar surrounded on either side by 2 μm Tedlar. The whole system is gas sealed.

Perflorobutan (C_4F_{10}) at 0.2% above the atmosphere pressure is used as our radiator. This gas is easily purified, ten times heavier than air, non-flammable and ultra-violet light transparent. Cherenkov light, emitted by the particles passing through the counter, is collected by the three different types of mirrors: elliptical, hyperbolic, and cylindrical (in the order in which the Cherenkov light hits them). The mirrors are precisely aligned to optimize the light collection by PMTs.

The calibration of the Cherenkov detector primarily involves equalizing the gains of the photo-tubes to determine the hardware thresholds. This is especially important in this experiment because the Cherenkov counters are included in the event trigger. For CC calibration the data acquisition system is configured to read only the Cherenkov detector information. To match the gains of the PMTs, the voltages are set up so that the mean of the single photo-electron (SPE) peak for each channel is in ADC channel 150. The data taken for these runs consists of photo-tube noise ("self-triggering" data). After gain equalization the position of each SPE was measured and stored in the off-line calibration data-base for each counter.

2.2.4 Time of Flight System

The Time-of-Flight (TOF) system of CLAS serves to measure the time between an event trigger and the time when a particle hits a TOF counter. As additional information, energy

loss (ΔE) in the scintillator material is used for calibration purposes. The TOF system consists of 288 scintillator counters, 48 counters per a sector (Figure 2.2), readout and trigger electronics and a laser calibration system [54]. As the study, development, calibration, and maintenance of this system were a considerable part of my work during this research project at Jefferson Lab, it will be described in more detail in Chapter 3.

2.2.5 Electromagnetic Shower Calorimeter

The forward electromagnetic shower calorimeter of CLAS (EC) covers scattering angles from $\theta = 8^\circ$ to 45° with ϕ coverage matched to that of drift chambers. The detector is segmented into six triangular sectors, each of which is longitudinally segmented into inner and outer components (see Figure 2.2).

The EC consists of 39 layers of plastic scintillator and lead with a total of 16 radiation lengths. The scintillators are laid in a pointing geometry to the target, so the width of the strips increases through the stack. The lead contains a 5% admixture of antimony for increased stiffness. The front and back surface of the detector are composites fabricated from thin stainless steel skins epoxied to a layer of structural foam; the side walls of each triangular sector are made from aluminum plate. The nominal scintillator (BC412) thickness is 1 cm, and the lead has a nominal thickness of 2.3 mm. Each scintillator layer is further segmented into 36 strips approximately 10 cm wide with single sided readout into one of three views. This provides good granularity and redundant position measurement for multiple-hit reconstruction. The three views are oriented approximately in the direction 0°, 120°, and 240° around the normal to the target. The optic readout of the EC is built from plastic fibers attached to the PMTs in flight-path-compensating geometry. The overall energy resolution of the EC for the electrons is close to its design

$$\frac{\sigma(E)}{E} = \frac{10}{\sqrt{E}}(\%).$$

The energy deposited in EC was used as a criteria for an electron event trigger in coincidence with CC signal in the same sector. The phenomenological conversion relation of EC hardware threshold to the electron energy is [65]:

$$EC_{Thr}(MeV) \;=\; 214 + 2.47 \times EC_{Thr}(mV)\,. \tag{2.1}$$

2.2.6 Cryogenic Hydrogen Target

A cryogenic Hydrogen target was used in this experiment. The specifications of the target are shown in the Table 2.1. At temperature of 18 K Hydrogen is in the liquid state. The total number of the Hydrogen atoms in the target is given by relation:

$$N_H = \frac{l_t \cdot D_t \cdot N_{Av}}{M_H} = 2.035 \cdot 10^{23} cm^{-2}\,, \tag{2.2}$$

Table 2.1: Specifications of the Cryogenic Hydrogen Target

Item	Value
Length (cm)	5.0
Radius (cm)	1.5
Hydrogen temperature (K°)	18
Hydrogen density (g/cm^3)	0.073

where l_t is the length of the target, D_t is the density of hydrogen, N_{Av} is Avogadro number and M_H is molar density of Hydrogen. The target cell walls were made of 120 μm Kapton. The input and output target windows had radii of 5 mm, and the window thickness was 15 μm Al. The thickness of the target cell and the windows were optimized to minimize the multiple scattering contribution in the target and walls to the total scattering rate. However, empty target runs were taken in order to measure wall contributions to cross-section on Hydrogen. Target parameters, temperature and pressure of liquid hydrogen, were continuously monitored during data taking and stored in on-line data base. Overall fluctuations of the target density during the experiment were below 1%.

2.2.7 Event Trigger of the Experiment

The signals from the CLAS detector components, designed to form an event trigger, pass through pretrigger discriminators, whose thresholds are programmed based on each experiment's requirements. The Level 1 trigger required a hit in the same sector for both the CC and EC above the pretrigger thresholds specified in Table 2.2. A coincident hit in any sector, signaling a potential electron in the detector, was used to initiate a readout of the event by the Data Acquisition System.

Table 2.2: CC and EC trigger thresholds.

Detector	Threshold (mV)	Threshold (GeV)
EC	80	0.411 $\pm$ 0.04
CC	15	($<$ 1 ph. electron)

The EC threshold as low as 411 MeV was used in order to accept the events with high values of the kinematic variable W. The CC threshold was below that of a single photo-electron peak in PMT and was unbiased to the extent possible. About 13% of the raw trigger events have an identified electron. The remaining 87% consist mainly of events in which particles

hit the CC mechanical structure causing showers, which generate pretrigger signals in both CC and EC. However, these events are easily removed during off-line data processing.

2.2.8 Data Acquisition and Monitoring Systems.

The block-scheme of the Data Acquisition System (DAQ) of CLAS is shown in Figure 2.4. It is a complex system, which includes each detector's read-out and hardware electronics, computers, and software [1].

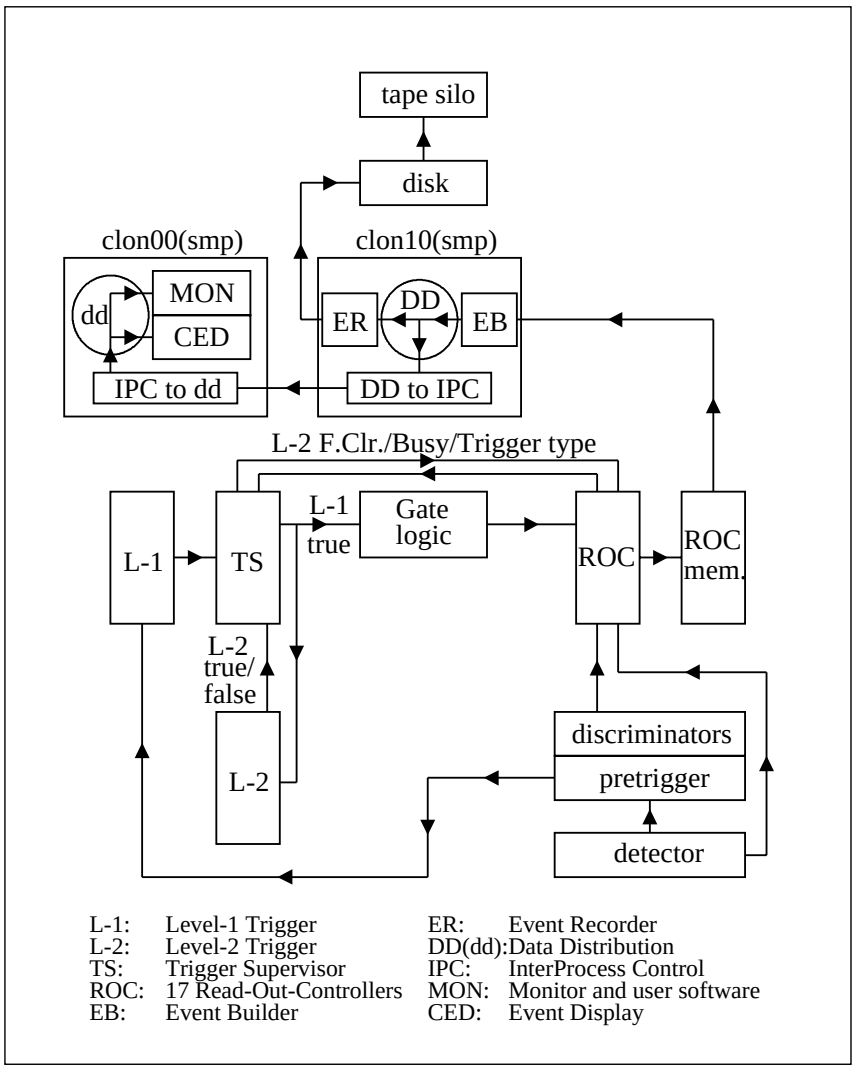

Figure 2.4: Data Acquisition system of CLAS.

[1] The software part of the DAQ was designed by CODA group of Jefferson Lab and DAQ group of CLAS.

The signals from the CLAS detectors, designed to form an event trigger, pass through the pretrigger discriminators, whose threshold is programmed according to the experiment's requirements. For this experiment the pretrigger threshold values are shown in Table 2.2. If the condition of the pretrigger is satisfied, the signal is passed to the Level-1 trigger, which contains the final configuration of the Event Trigger (see subsection "Event Trigger of the experiment"). If these requirements are satisfied, the signal is passed to the Trigger Supervisor [2], which communicates with 17 FASTBUS crates. Data signals are read out, digitized, and transmitted through ROC memory and network to the Event Builder. From the Event Builder the data pass to the Event Recorder through the main Data Distribution shared memory. From the Event Recorder data is written to a local disk and later archived to the tape silo of Jefferson Lab. During this experiment, running with 4.2 GeV electron beam at luminosity of about $L \approx 0.6 \cdot 10^{34} cm^{-2} s^{-1}$, the DAQ system allowed the recording of data at a frequency of 1500 Hz with a live time of about 96%.

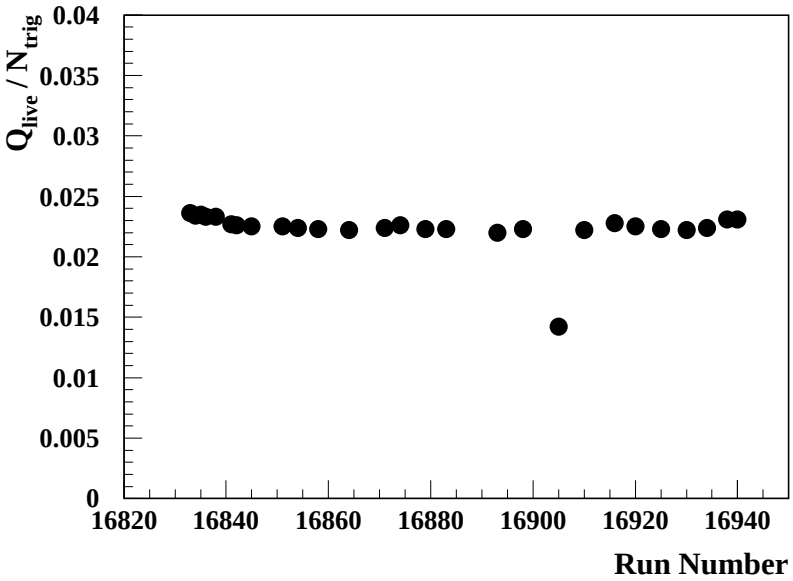

Figure 2.5: Run-by-run ratio of the live-gated accumulated beam charge to the total number of triggers during E1b data taking with 4.2 GeV electron beam energy.

For on-line monitoring purposes the main Data Distribution system picked out the events from the data stream with a frequency of 20 Hz and transfered it to a satellite computer with its own data distribution (see Figure 2.4), which served to supply the monitoring programs with the data. The detector status, beam, and data quality were continuously monitored in real time during data-taking. The most important run characteristics such as the total number of triggers, integrated beam charge, the averaged live-time of the DAQ and magnet settings were stored in the CLAS on-line data base. As an example of the detector and DAQ

[2]The Level-2 Trigger was designed to select the events with at least one track in drift chambers of CLAS. It was not implemented during this experiment.

stability monitoring, the run-by-run ratio of the live-gated accumulated beam charge to the total number of triggers during data taking is shown in Figure 2.5. This plot demonstrates that the data were usually taken with stable conditions. The low value of the ratio for the run number 16905 indicates that there is a potential problem with the DAQ or one of detector systems [3].

[3] In this case, it was possible to fix the problem during the off-line analysis.

Chapter 3

Time-of-Flight System

3.1 General Description

3.1.1 TOF Counters

The TOF counters cover the range from 8° up to 142° in polar angle θ and almost the entire range of azimuthal angle ϕ (see Figure 2.2). The scintillators are positioned outside the tracking system between the Cherenkov counters and the calorimeter. The counters are mounted in four panels in each of the six sectors. Scintillators 1-23 are mounted in panel 1, often referred to as "forward angle". Panels 2, 3 and 4 are called "large angle". The scintillator thickness of 5 cm is uniform throughout, chosen to give a large signal for traversing minimum-ionizing particles compared to background. Each scintillator is placed perpendicular to the beam direction such that the width of the counter subtends about 1.5° of scattering angle. The counters are parallel to the drift chamber axial wires.

Each TOF counter consists of scintillator material (Bicron BC-408) and two Photomultiplier Tubes [1] (Thorn EMI 9954 for the forward angle and Philips 4112B/D2 for the large angle counters) which read out the light, produced by a through-going particle. In order to obtain good particle identification, particularly for the kaons, a good time-of-flight resolution is required. The two-sided readout reduces the uncertainty in measured time by a factor of $1/\sqrt{2}$. The whole system was designed to have average time resolution of about 120 ps. In order to achieve this resolution a multi-step calibration procedure was performed during the experiment and data analysis [55], and will be described in detail in Section 3.2.

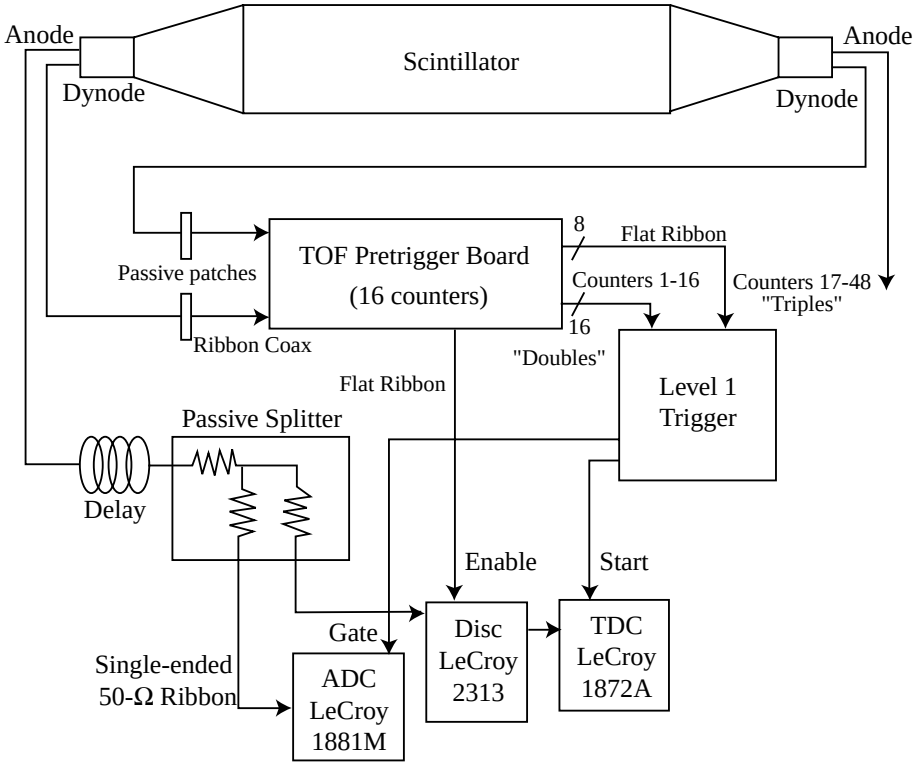

Figure 3.1: Time-of-Flight system electronics layout.

3.1.2 TOF Electronics.

All PMTs of the TOF counters are powered with about -2000 Volts by five LeCroy 1458 mainframes, which are controlled remotely from the Counting House of Hall B. The TOF counters generate prompt signals for the CLAS Level 1 trigger electronics [54] as well as signals for pulse-height and timing analysis. The overall layout of the TOF electronics which processes these signals is shown in Figure 3.1. The trigger from the TOF counters is initiated by events that deposit energy in the scintillators greater than some preselected value. The inverted PMT dynode pulses go to a pretrigger circuit where two signals are produced. One of these signals goes to the Level 1 Trigger, and the second is a gate pulse which is used to accept the corresponding signals of the low-level discriminator. Custom electronics are used for energy discrimination in the pretrigger circuit. The charge of the anode pulse is recorded by a LeCroy 1881M ADC for later analysis. The time of the pulse is determined by a LeCroy 1872A FASTBUS TDC triggered by a LeCroy 2313 discriminator set at a low threshold for precise timing.

[1]Referred to in the future as Left and Right.

3.1.3 Laser Calibration System

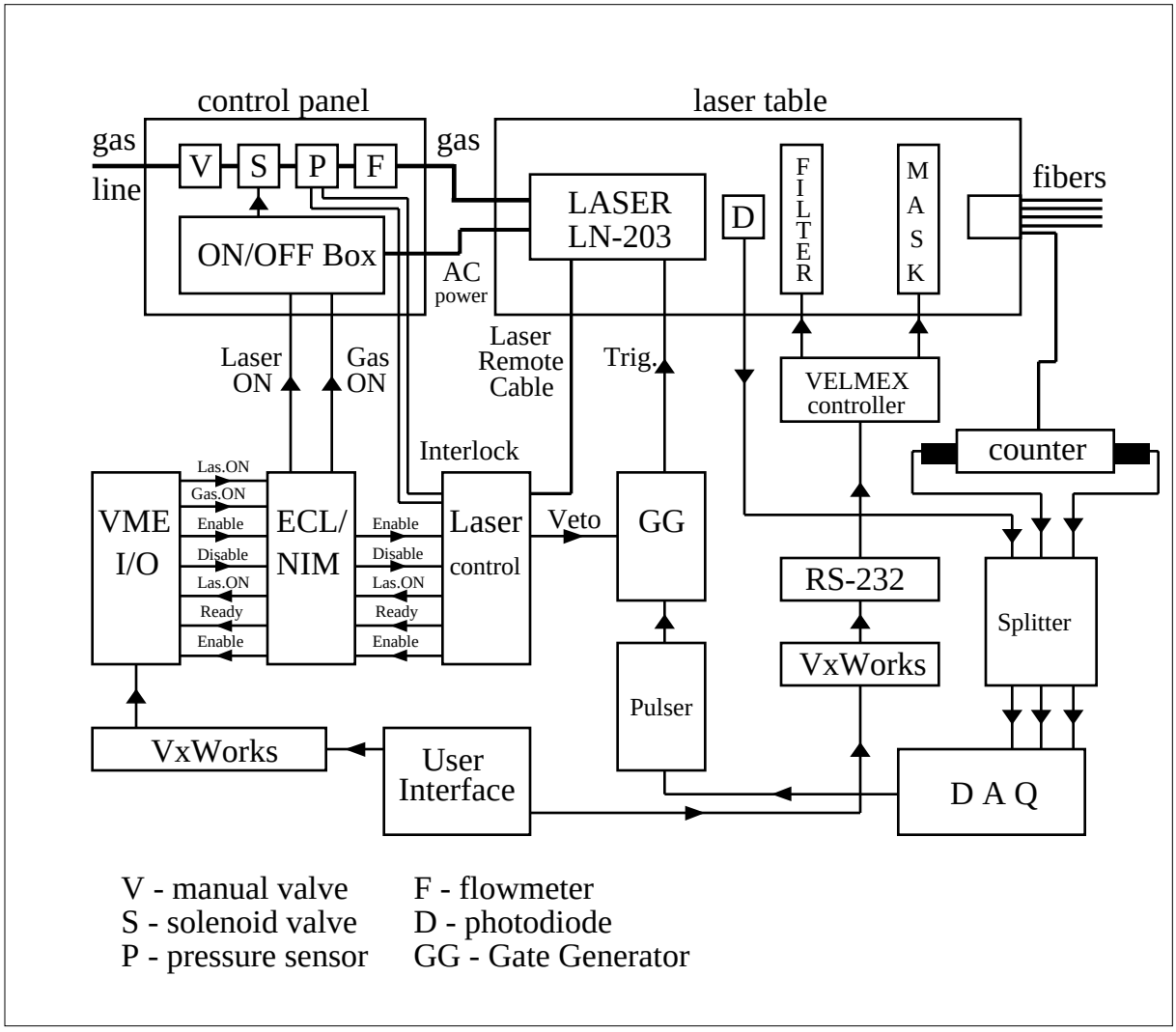

Figure 3.2: Block-scheme of the Time-of-Flight Laser Calibration System.

A system of four UV lasers (spectral output 337.1 nm) is used to calibrate the TOF counters. The schematic of the laser system set-up is show in Figure 3.2. The signal from an injected short UV light pulse is used to simulate the scintillator response to a through-going particle. UV light is delivered from the lasers to the center of each scintillator via a quartz optical fibers with core diameter of 200 μm and a 240 μm cladding. Signals, generated by the laser light, follow exactly the same path through the electronics as the signals of through-going particles during the experiment. The TDC and ADC information from the laser pulses is used to calibrate the pulse height dependent time-walk corrections, associated with the discriminator threshold settings.

Table 3.1: Specifications of the pulsing Nitrogen UV-laser

Item	Description
Model	Laser Photonics, LN203
Spectral output (nm)	337.1
Spectral bandwidth (nm)	0.1
Pulse-width FWHM (ps)	600
Energy/Pulse (μJ)	100
Energy stability at 10 Hz (%)	3
Maximum repetition rate (Hz)	50

The lasers are located near the counters in the experimental Hall to minimize the dispersion of the laser pulse in the fibers. The main specifications of the Laser Photonics [2] UV-lasers LN203 are shown in the Table 3.1.

The laser beam is directed through an opening in the radio-frequency-shielded enclosure to a series of optical and mechanical elements. The laser beam first encounters a flat quartz plate which reflects a small part ($\approx 4\%$) of the light back to a fast photo-diode [3] circuit which is used as a time reference of the laser signal with respect to the TOF counters. Most of the laser light passes through a Reynard Corporation [4] variable neutral density filter with a dynamic range of 1:40. This filter is used to attenuate the light over a range of values suitable for measuring the time-walk correction of every discriminator channel. The filter is adjusted by a remotely controlled stepping motor. Downstream of the filter, the beam is expanded by a Physical Optics Corp. [5] CTR 5×3 diffuser. The beam can then be partially intercepted by a "mask" controlled by a stepping motor. Several different hole patterns along the "mask" can be positioned to illuminate various combinations of fiber bundles. Each bundle consists of seven all-silica 100-μm diameter fibers (numerical aperture is 0.22) which are 13 m long and distributed to the various scintillators. There are 24 bundle ends which are arranged in a 4 by 6 rectangular array behind the "mask" within an area of 3.0 cm^2. By lighting the different "mask" patterns cross-talk effects in the readout electronics can be studied [6].

[2]Laser Photonics, Inc. 12351 Research Parkway, Orlando, Florida 32826.
[3]P/N Diode, Motorola MRD 500.
[4]Reynard Corporation, 1020 Calle Sombra, San Clemente, CA 92673.
[5]Physical Optics Corp., 20600 Gramercy Pl., Torrance, CA 90501-1821.
[6]The "mask" application of the TOF laser calibration system has not yet been used.

3.2 TOF Calibration Procedure

The data for each channel of the TOF system consists of an ADC pulse height(A), with a maximum value of 8192, and a TDC time (T), with maximum value of 4095. Calibration of the system requires ADC pedestal determination, gain-balancing and gain-matching of the pulse heights, determination of the time-walk correction functions, and relative time-offsets of each counter [54, 55].

Three sources of data were used for calibration: laser light, cosmic rays, and reactions of 1.6, 2.4, and 4.0 GeV electron beams on a liquid hydrogen target. In general, the laser system was used when studying the characteristics of a single counter while times between different scintillators were studied with cosmic rays or production data, as there are large variations in the laser pulse amplitude for different counters and every laser fiber could have a different time offset.

3.2.1 Timing and Pretrigger Thresholds.

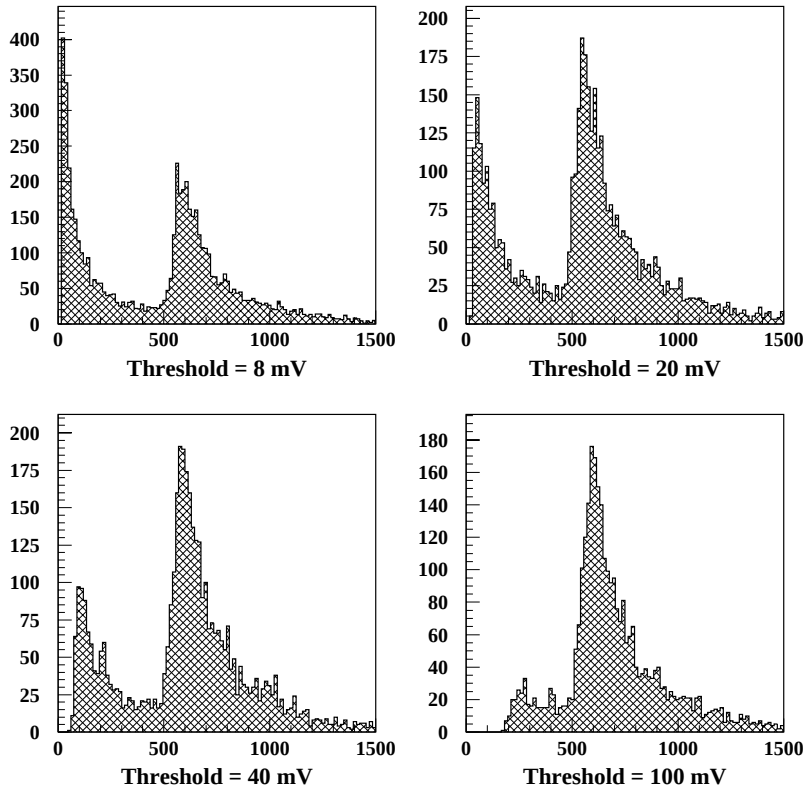

Figure 3.3: Geometric mean of both ADC's for different values of the timing discriminator threshold. A value of 20 mV has been chosen for the data taking runs.

Special beam data runs with a single TOF counter in the trigger and various thresholds were taken to calibrate discriminator thresholds in terms of the ADC pulse height. For the pretrigger discriminator calibration the data with only one self-triggering TOF counter turned on were taken with different threshold values. For the timing discriminator calibration the data with only one TOF counter turned on were taken with different threshold values, using the trigger described in Section 2.2.7. As an example of the threshold effect, the geometric mean of left and right ADC's of counter 8 in sector 2 is shown in Figure 3.3 for different values of the timing threshold of the LeCroy 2313 discriminators.

Figure 3.4 summarizes the cutoffs for each ADC and for geometrical mean of both ADCs as a function of timing discriminator and pretrigger board thresholds. The proportionality coefficient is determined by fitting these data ($\chi^2/DF = 1.32$):

$$ADC(channels) = (1.73 \pm 0.055) \times THR(mV) \tag{3.1}$$

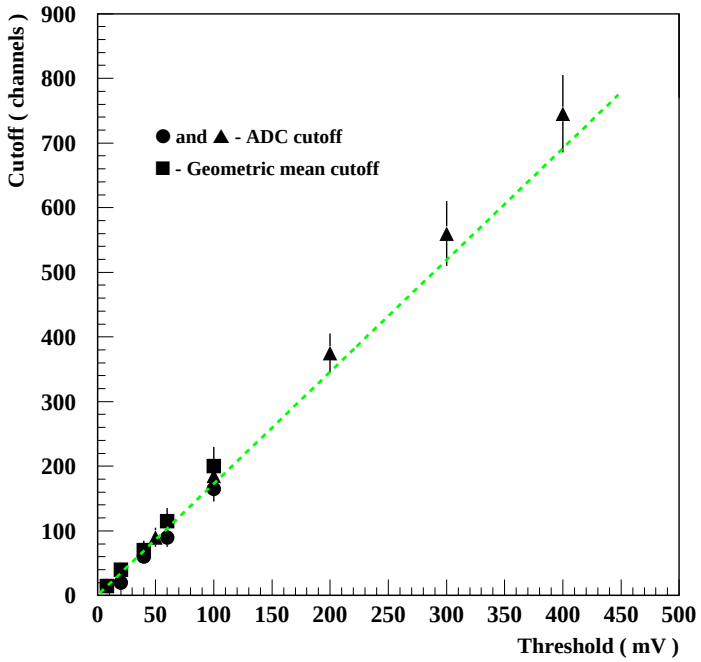

Figure 3.4: Cutoffs for each ADC and for the geometric mean of both ADC's versus the timing discriminator and pretrigger board threshold. The green dashed line is the fit to the function in Equation 3.1. ADC cutoff dependences have been used to determine the proper threshold setup.

The TDC discriminator threshold should be set up above the accidental background without cutting the signals of interest in the TDCs and ADCs. By setting the threshold below 20 mV we saw a large background contribution to the total rate ($\sim$ 10%). The most appropriate threshold for TDC discriminators appeared to be 20 mV which was the setting during the data-taking runs (see Figure 3.3). The proper pretrigger threshold should be set up during the experiments by considering background contributions to the total trigger rate and the fact that the gain of TOF PMTs was adjusted such that the Minimum Ionizing Particle

(MIP) peak is on average at ADC channel 600. During this experiment the TOF counters were not included in the trigger.

3.2.2 ADC Pedestals and TDC Calibration

For measuring the ADCs pedestals a random trigger was generated by the DAQ. The data was analyzed on line and the results were put in the off-line calibration database. In order to avoid reading the low voltage noise in the ADC's, the DAQ sparsification threshold was added to the pedestals values, and the resultive numbers were loaded into the 1881M FASTBUS ADC. The sparcification threshold was chosen to be 40 ADC channels, which is consistent with TDC offset, which corresponds to approximately 35 channels.

Special DAQ configuration was used to take the TDC calibration data [66, 55]. A quadratic equation was used to convert the TDC channel number T to time units (ns):

$$t \;=\; c_\circ + c_1 T + c_2 T^2 \tag{3.2}$$

where typical values of $c_\circ \sim 1$ ns, $c_1 \sim 0.0495$ ns/ch, and $c_2 \sim 5{\times}10^{-8}$ ns/ch^2. The constant terms, arbitrary at this point, were constrained so that the average of the 64 channels of each FASTBUS card was zero.

3.2.3 Attenuation Length and Effective Velocity

Beam data were used to extract the effective attenuation length, Figure 3.5, and effective velocity for photons in each counter, Figure 3.6. The effective attenuation length depends both on counter length and width. The errors on effective velocity are large for the first two counters because they are too short to give a reliable measurement. As the counter length increases, so does the effective velocity because the light rays at large angles with longer actual trajectories to the PMT are systematically lost owing to attenuation. These constants are used in TOF analysis to determine the hit position and energy deposition of each event. The intrinsic position resolution along the counter is given by [7]

$$\sigma_{int} = \frac{1}{2}\, v_{eff}\, \sigma(T_{left} - T_{right})\,, \tag{3.3}$$

where v_{eff} is the effective velocity and $\sigma(T_{left} - T_{right})$ is the left-right timing uncertainty. This is most relevant for the position measurement of the neutral particles. The position for charged particles can be measured more precisely with the drift chambers.

[7] The factor of 1/2 corrects an error in Reference [54].

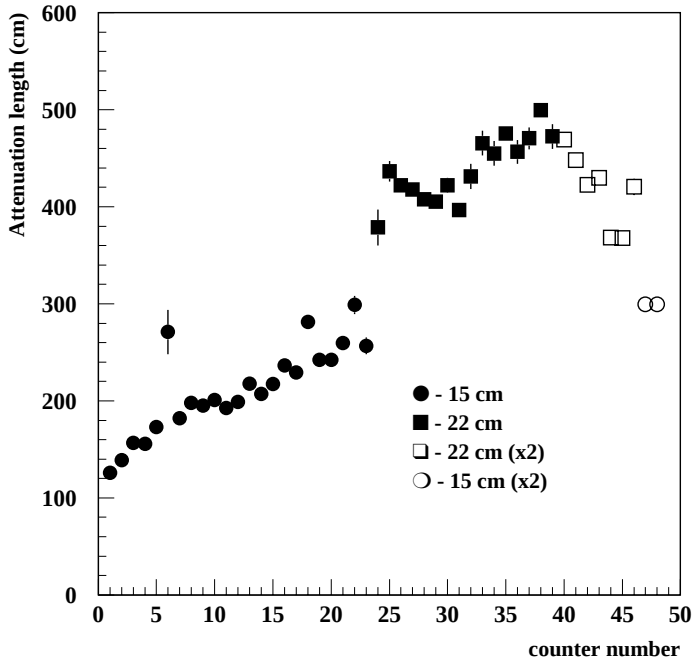

Figure 3.5: Effective attenuation length of scintillator material versus counter number. Each value represents an average over six sectors. The effective attenuation length depends both on counter length and width. The solid and open symbols show the data for the scintillators with different width.

3.2.4 Gain Matching

The purpose of gain-matching is to equalize the detector response to crossing tracks. This is a necessary procedure because each counter must contribute equally to the trigger for a common-threshold discriminator level. The gain-matching procedure is accomplished by adjusting PMT high voltages so that normally incident minimum ionizing particles (MIP) produce a peak in ADC channel 600 above the pedestal for every counter. The value was chosen from two considerations: the dynamic range of the ADC is 8192, and we expect a range of deposited energy to vary by a factor of 8, which sets the upper limit. Also, we want to be above the low channels where time-walk corrections are more important. Initial voltages were set using the laser system which matched the gain of PMTs on opposite ends of the same scintillator. The response to particles was accomplished using cosmic-ray muons. Figure 3.7, a histogram of the mean value of energy losses for MIPs, shows that the spread of gain matching was about 30% (FWHM), which is adequate for our experimental purpose.

To find the energy deposited, the ADC pulse height A are first corrected for the ADC pedestal value P, then the pulse height is normalized to that of a normally-incident, MIP at the center of the scintillator. The quality of this software energy calibration is indicated by Figure 3.8, a scatter plot of energy loss versus particle momentum. The measured pulse height

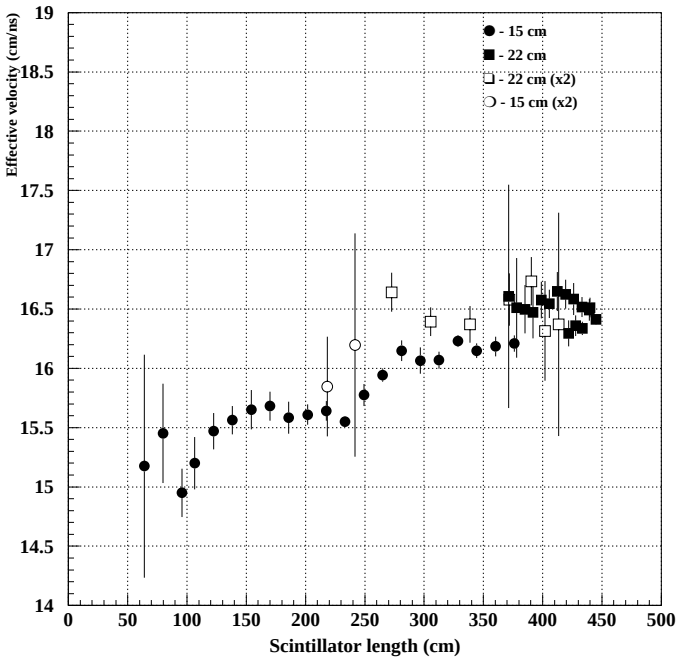

Figure 3.6: Effective velocity of signal propagation versus scintillator length. Each value represents an average over identical counters in six sectors. The solid and open symbols show the data for the scintillators with different width.

normalized to the calibrated MIP peak value is used to reconstruct the energy deposited in the scintillators. The energy loss increases linearly at low momentum for protons stopping in the scintillator until they begin passing through the scintillators at which point the energy loss follows the Bethe-Block formula. The pions and protons are clearly distinguished for momenta between 0.3 and 1 GeV/c.

3.2.5 Time-Walk Correction

The time-walk corrections, and left-right timing constants, were obtained with the laser system which delivers a light pulse to the center of each counter. Using a neutral density filter to vary the amount of light delivered to each counter, the pulse-height and time were measured for pulses with different amplitudes. These data were used to obtain the dependence of the LeCroy 2313 leading-edge discriminator pulse-timing on the pulse height. This dependence is shown in Figure 3.9 for a typical PMT.

The measured times correspond to the time of a PMT pulse crossing a fixed (leading-edge) voltage threshold. To correct for time-walk, we perform software corrections of the form

$$t_w \;=\; t - f_w\left(\frac{A-P}{Th}\right) + f_w\left(\frac{600}{Th}\right) \tag{3.4}$$

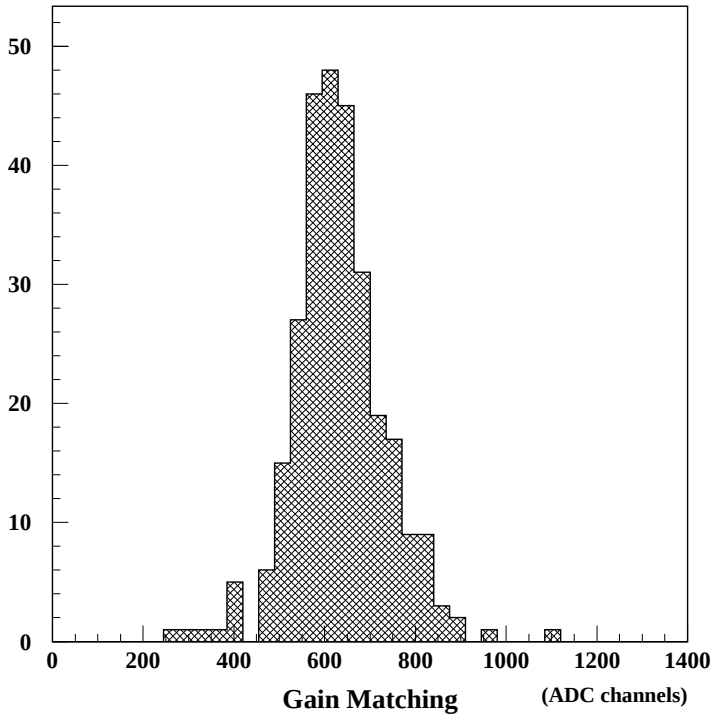

Figure 3.7: MIP peak position of all Time-of-Flight counters.

where Th is the channel corresponding to the leading-edge discriminator threshold of 20 mV (approximately 35 channels), and $f_w(x)$ is the time-walk-correction function described below. This parameterization has the desirable limit that t and t_w are equal for minimum-ionizing pulses in ADC channel 600. The function $f_w(x)$ is a monotonically decreasing function of A since the measured time is late for a pulse with a finite rise time. Our parameterization has three fit parameters w_0, w_2, and w_3. They were determined for each PMT separately using the laser calibration system described in Subsection 2.2.5. Fits to data indicate that the time-walk correction is described by a function which first decreases rapidly as a power law then changes to a slow linear decrease:

$$\begin{aligned} f_w(x) &= \frac{w_2}{x^{w_3}} \quad \text{if } x < w_o \\ f_w(x) &= \frac{w_2}{{w_o}^{w_3}}(1+w_3) - \frac{w_2 w_3}{{w_o}^{w_3+1}}\, x \quad \text{if } x > w_o \end{aligned} \tag{3.5}$$

The linear part of the curve [(A - P) $\geq$ $Th \times w_o$] corresponds to saturation of the PMTs. Monte Carlo calculations demonstrated that the time-walk parameters are not significantly affected by the position of the track through the scintillator [63]. The fitted parameters were obtained for the (A - P) range between 0 and 8100 counts and typical values are w_o ~50 (depends on the PMT), w_2 ~15 ns and w_3 ~0.07, with a strong correlation between the last two parameters.

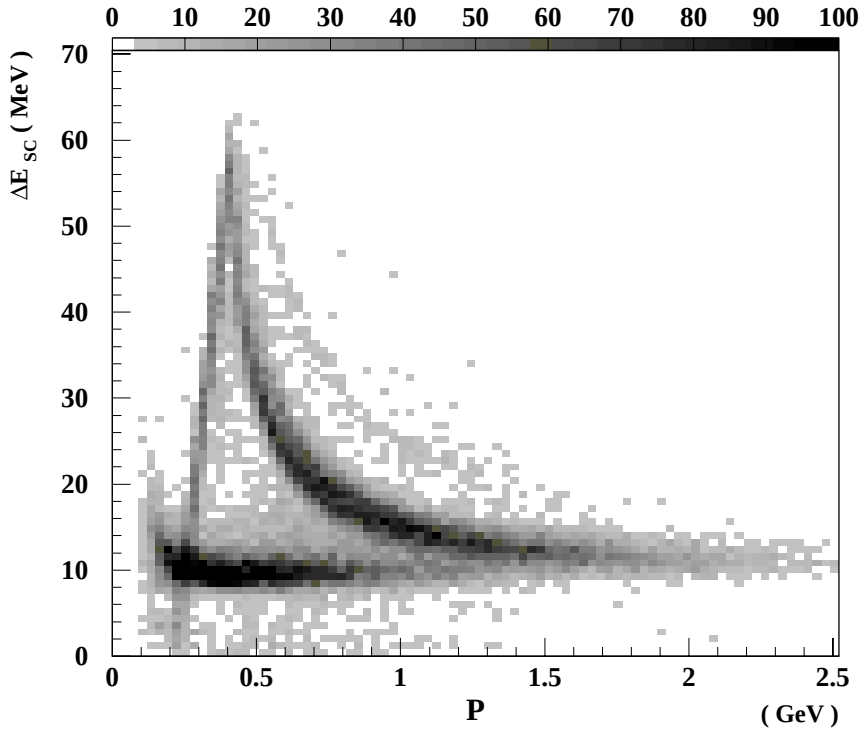

Figure 3.8: ΔE in scintillator material versus momenta of the passing through particle. Proton and pion bands can be clearly distinguished.

3.2.6 Counter-to-Counter Delay Calibration

The reaction ep→eπX is used to determine the relative time delays between the 288 counters by comparing the time from a TOF counter to the time of the beam RF [64]. The RF signal from the accelerator has a 2.004 ns period which is large enough to be resolved by the TOF system by using scattered electrons. The RF bunch length itself is a few picoseconds, and timing signals are provided by the accelerator as a reference to the experimental areas. We note, that while the timing signals are very accurate, the determination of which bunch produced a given interaction must be made by the experiment. The electrons are identified using information from the CLAS Cherenkov and calorimeter.

The calibration is divided into three steps, and in the first two steps only the ten forward scintillators in each sector were used. First, the difference between the time obtained from an electron in the TOF scintillator and the time of the RF bunch was calculated. This time is divided by 2.004 ns and the remainder is taken as the offset correction to the TOF time. However, there is still a 2.004 ns ambiguity since the actual beam bunch, which caused the event, is unknown. In order to correct for this ambiguity, electron-pion coincident events are used. Both electron and pion are detected in the forward 10 strips in different or in the same sector. Pions are selected using energy loss measured in the TOF counters (see Figure 3.8), and momentum and path lengths are calculated using reconstructed tracks in the CLAS

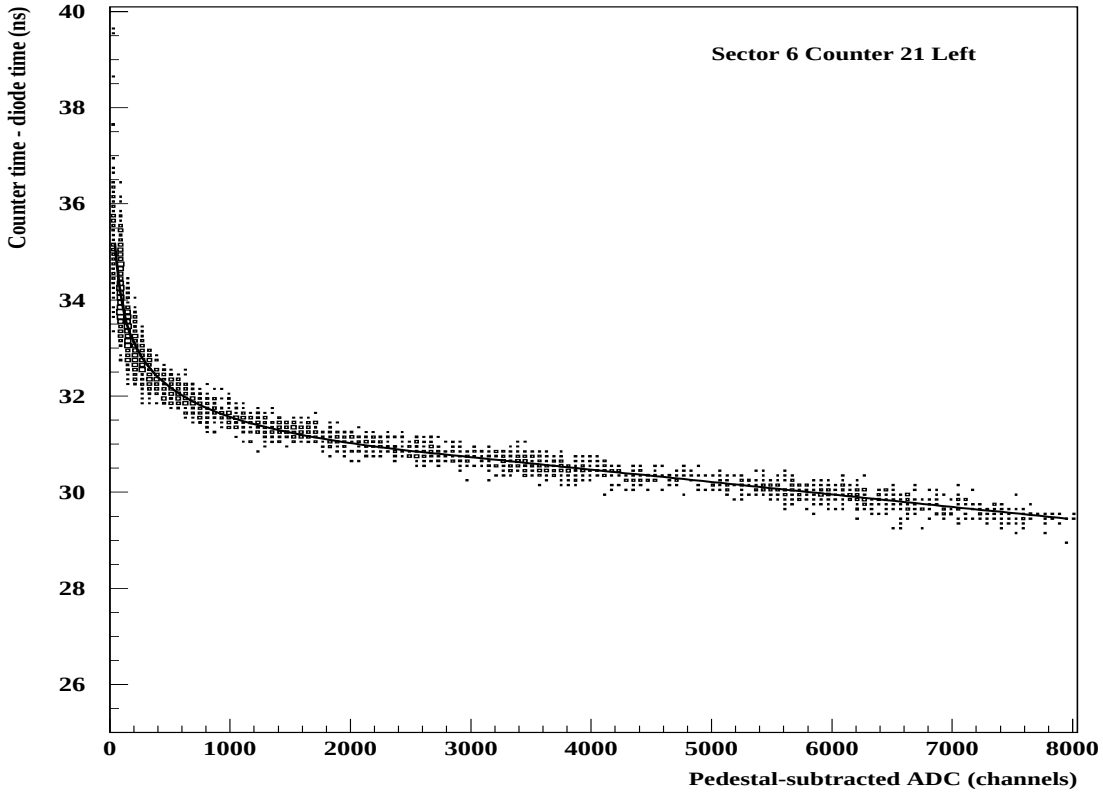

Figure 3.9: Typical example of the TDC time dependence on the pulse hight. The line shows the fitted time-walk function (Equation 3.5).

drift chambers. The calibration constants for each counter are then determined by requiring that the two reconstructed tracks have the same vertex time. In the final step the remaining TOF scintillators (11-48 in each sector) are calibrated by detecting an electron in any of the first ten counters and a coincident pion in the counter being calibrated. The result of the calibration procedure is shown in Figure 3.10c where the predicted vertex time of electrons in all counters is compared to the RF accelerator time. Overall timing resolution for the electrons is about 147 ps.

3.2.7 Alignment of TOF to Accelerator Radio Frequency

The 499 MHz RF signal of the accelerator was recorded together with accumulated data. This allowed us to synchronize events with the beam bunches during reconstruction and fix the event start time at the time of the appropriate beam bunch. Using the exact event start time[8] we eliminate the timing uncertainty of the electron and, ideally, should gain a factor of $\sqrt{2}$ in reconstructed mass resolution for the hadrons. Because of uncertainty in track length measurement the improvement in hadron mass resolution is about 10%. Since the

[8]The uncertainty is equal to the beam bunch width of a few picoseconds.

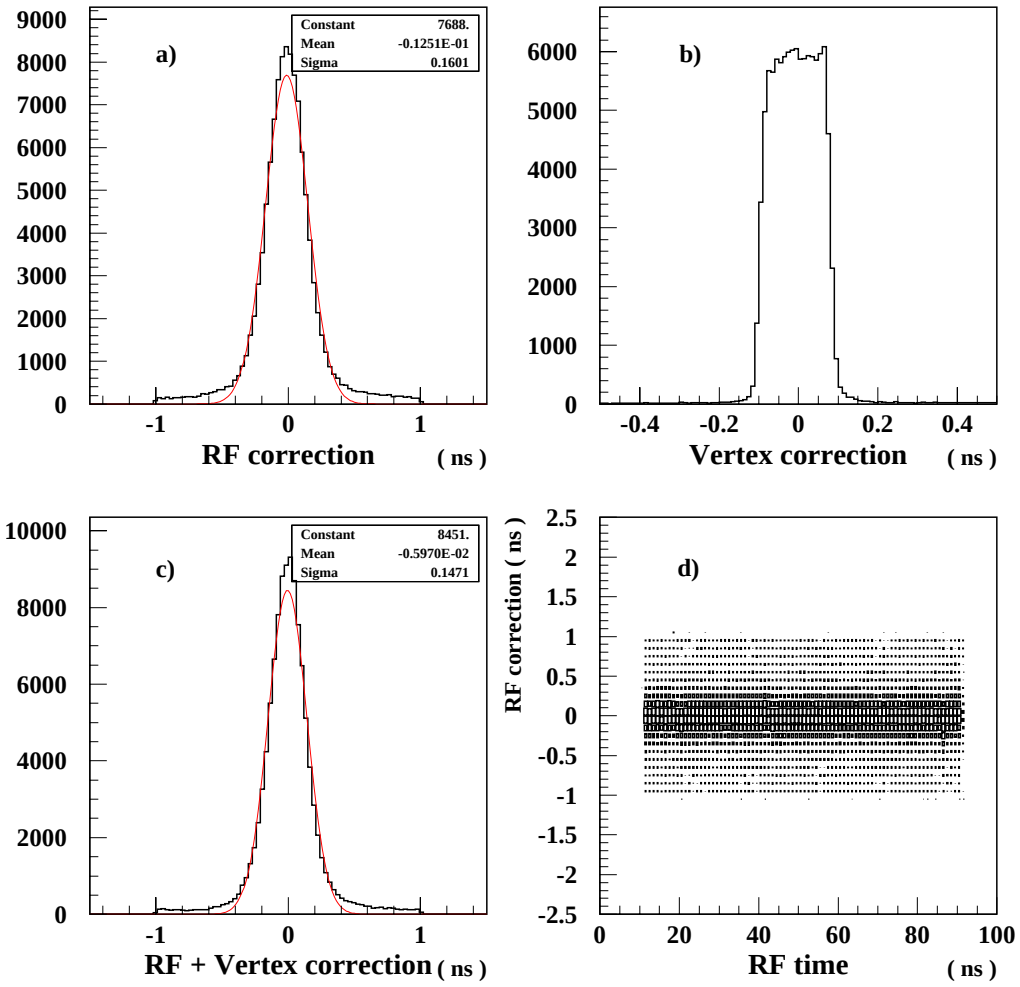

Figure 3.10: a) Measured vertex time relative to the RF signal; b) Vertex time relative to the time at the center of target; c) Measured vertex time relative to the RF signal after both the RF and vertex corrections are applied; d) Event vertex time versus raw RF time. It shows that after calibration the RF corrections are independent of the RF time.

counter-to-counter delays were already adjusted with respect to RF signal, the goal of this calibration is to fix the RF time relative to the whole TOF system to zero on run-by-run basis. Mostly, this adjustment to the RF time is is an empirical correction to compensate for little changes of the accelerator setup as a function of time. Major changes to the alignment parameters occur for each new accelerator configuration.

The difference between event start time and RF signal time (denoted as RF_{corr}) can be determine as :

$$RF_{corr} \;=\; T_{RF} - (\,T_e^{TOF} - \frac{L_e}{\beta_e}\,) + \frac{Z_{vert}}{\beta_e}\,, \tag{3.6}$$

where T_{RF} is the time of the RF signal, T_e^{TOF} is the measured electron time, L_e is the measured length of electron track, Z_{vert} is the event vertex coordinate along the beam line,

and β_e is the electron velocity, which is equal to the speed of light c. Only the RF correction term is shown in Figure 3.10a, overall timing resolution for the electrons is about 160 ps. The target correction term Z_{vert}/β_e (Figure 3.10b) is added to compensate the effect of target length. The result of both the RF and vertex corrections is shown in Figure 3.10c. These corrections give better timing resolution for electrons of about 147 ps. The RF correction dependence on the RF raw time is shown in Figure 3.10c. The goal of this calibration is to fix the mean value of RF_{corr} at zero and eliminate any systematic trend in RF_{corr} versus the RF time. The algorithm of the RF calibration is described in detail in Reference [55]. It allows the use of four independent functions (polynomial up to third order) in four regions of raw RF time to eliminate any systematic trends. Outside of these regions the RF correction is equal to zero and the start time of event is not corrected. The overall RF offset can be adjusted by one constant, common for all four functions.

3.3 TOF Resolution

The time resolution of each counter was estimated by using electron-pion coincidence events. The TOF times were determined by averaging the times of right and left PMTs. The electron track was then reconstructed and its TOF time was corrected for the flight time back to the target. This time was used to determine which RF bucket containing the incident electron and the accelerator RF time was used as the true vertex time. The measured vertex time using the pion track was compared to this time to estimate the time resolution of the counter under consideration.

The resolutions for each counter determined in this manner are shown in Figure 3.11 as a function of counter length. Scintillators of 100 cm in length, corresponding to a scattering angle of about 18°, have a measured resolution of 150 ps. At larger angles the resolution slowly degrades as expected, as the length of the scintillators increase. However, at smaller angles, the resolution also degrades, a result of higher rate or background in these counters. These measurements with beam events include non-optimized time calibration procedures and momentum and path length contributions from track reconstruction. Nevertheless, the resolution is acceptable and the level of particle identification already achieved allows the experimental program in Hall B to reach its goals. With the experience of operating the CLAS the resolution of all detector systems will be improved.

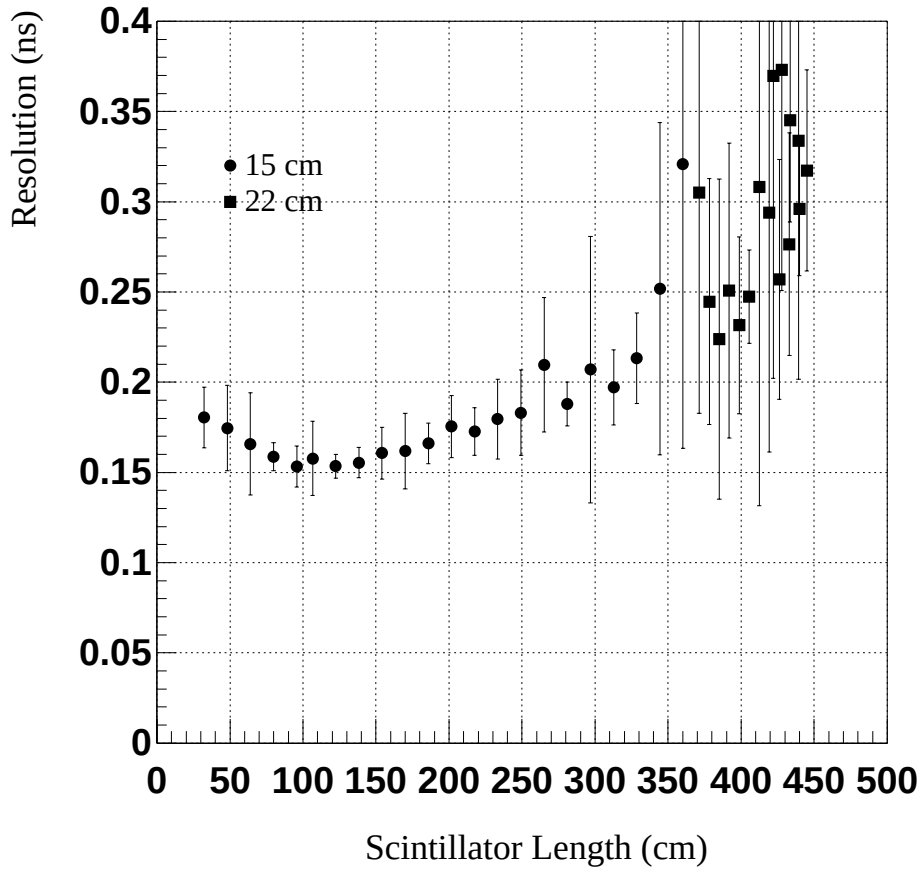

Figure 3.11: Resolution as determined by electron-pion coincidence. Each data point corresponds to the measured average for six identical counters, the error is the deviation among measurements. The solid circles and squares symbols show data for the scintillators of different width.

Chapter 4

Processing and Analysis of the Data

The data were collected during the first (E1a) and the second (E1b) electron beam running period between February and March 1998 and 1999, respectively. The data were taken on Hydrogen target at beam energies of 4.0, 4.2 and 4.4 GeV and with 60% and 85% of full main torus field (currents 2250 A and 3375 A, hereafter referred to as low and high field data respectively), running with luminosity of about $L \approx 0.6 \cdot 10^{34} cm^{-2} s^{-1}$. The beam current was limited by the background conditions in the drift chambers of CLAS. The coincidence of the Cherenkov Counter and forward Electromagnetic Calorimeter was required in the Level 1 trigger of the CLAS DAQ system (see Subsections 2.2.8 and 2.2.7). The amount of collected data is shown in Table 4.1. In accordance with the proposal of the experiment [62], the data taken at 4.0, 4.2 GeV and 4.4 GeV with 60% of full magnetic field are acceptable for the study of the ϕ production channel. The high field data sample was not used because of low acceptance for the epK^+K^- final state and high Q^2 threshold. For the analysis, presented in this work, the largest data sample, taken with 4.2 GeV of beam energy, was used. The E1a data at 4.0 GeV beam energy were also analyzed, and the results were reported in Reference [67]. Those results were used as a consistency check between two independent data sets.

Table 4.1: Data collected during the E1 run.

run period	beam energy (GeV)	torus current (A)	integrated luminosity (cm^{-2})	data status
E1a	4.0	2250	$0.253 \cdot 10^{39}$	Processed & Analyzed
E1b	4.0	2250	$1.165 \cdot 10^{39}$	Processed
E1b	4.2	2250	$1.486 \cdot 10^{39}$	Processed & Analyzed
E1b	4.4	2250	$\approx 0.3 \cdot 10^{39}$	Not available

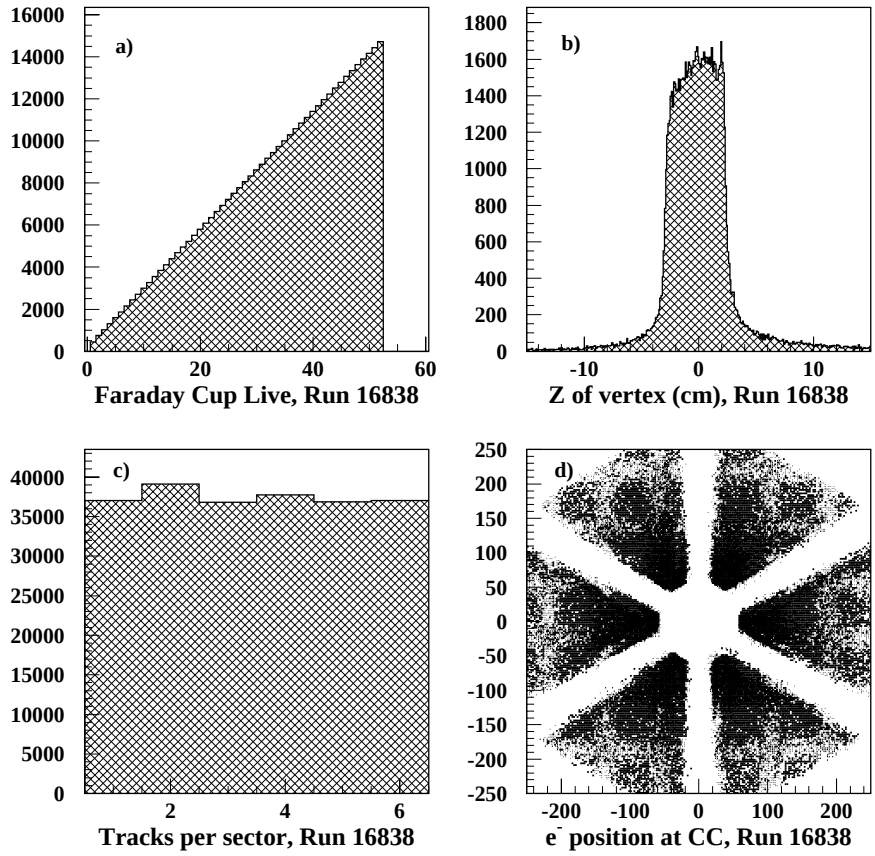

Figure 4.1: Examples of monitoring histograms for run number 16838 at 4.2 GeV. a) Value of the Integrated live-gated Faradey Cap current versus acquisition time. This dependence is used to determine the beam stability over the run period. b) Z position of the vertex for two-track events. This distribution is used to measure any ice building on the target walls. c) The number of hit-based reconstructed tracks per sector. d) Position of electron track projected out to the CC plane.

4.1 Data Processing

4.1.1 Preprocessing

For calibration purposes, a selected data sample (∼2% of the total) was processed several times. This sample uniformly populated the entire run period. These short passes through the data were used to improve the event reconstruction software and the calibrations of CLAS components. When the data reconstruction achieved the required performance level, the software and calibration maps were "frozen" in the production library PROD-1-9. This library was used to process all data (hereafter referred to as "cooking" the data). The reconstruction code required that at least one negative hit-based track be found in the drift

chambers of CLAS in each event. About 13% of triggers survived this criteria; and for those events the entire event-reconstruction and a few monitoring and filtering procedures were performed.

The output of monitoring programs (pdu_mon, trk_mon, pid_mon, sc_mon, rf_mon and scaler_mon), e.g. Faradey Cap readout values and yield of each kind of particle per sector, was put in the off-line data base and was used to control the quality of the data. The calibrations, data normalization, and histogram files were saved together with the reconstructed data. Examples of monitored quantities are shown in Figure 4.1. The results of monitoring DAQ live-time, the Faraday Cup information and the number of deuterons normalized to beam current, were used in cross section calculations.

During the processing, candidates for the epK^+K^- final state were selected and filtered into separate files. The purpose and criteria of this procedure is described in the following subsection.

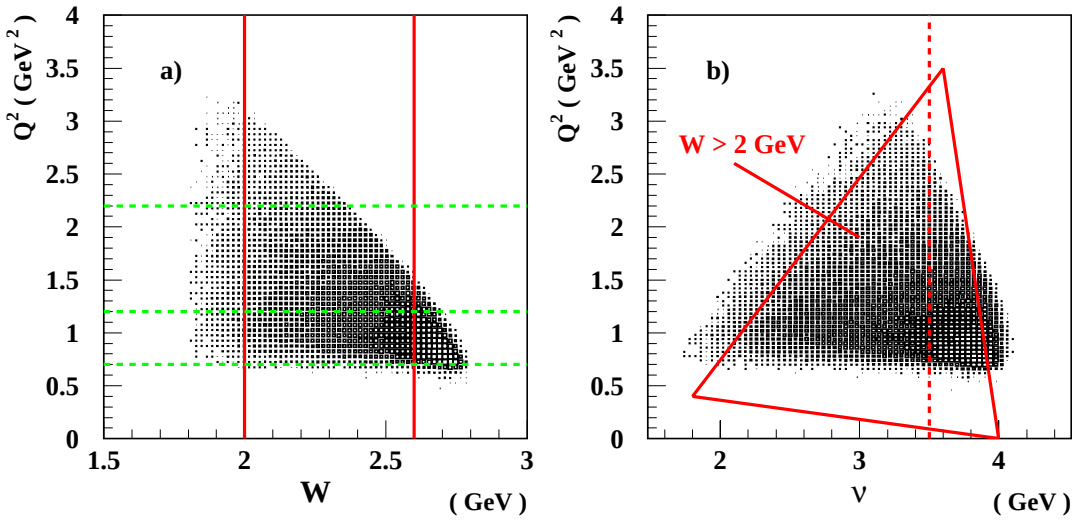

Figure 4.2: Kinematic distributions of the filtered epK^+K^- event sample: a) Q^2 versus W. The solid red lines show the W bin, the dashed green lines show the binning in Q^2. b) Q^2 versus ν. The solid red lines show the threshold for $\phi(1020)$ meson production.

4.1.2 Selecting the epK$^+$K$^-$ final state

a. Filtering procedure. The purpose of this work was to study the features of ϕ meson electroproduction in the K^+K^- decay channel. In order to reduce the data sample of interest to a manageable size and understand the particle identification (PID) and kinematic cuts, the 4.2 GeV data were first filtered with very loose requirements on PID, missing mass and the requirement for W to be above 1.8 GeV. Because of very small acceptance of K^- we required only three particles to be detected in CLAS: electron, proton and K^+. The K^- was

Table 4.2: The cuts for the epK$^+$K$^-$ final state filtering procedure.

Quantity	Low cut	Upper cut	Purpose
W (GeV)	1.8	–	Reject events below ϕ threshold
$(M_p)^2$ (GeV^2)	0.5625	1.44	Select proton candidates by TOF
$(M_{K^+})^2$ (GeV^2)	0.09	0.49	Select K^+ candidates by TOF
$(MM_{epK^+})^2$ (GeV^2)	0.09	0.49	Select events with missing K^-

reconstructed by identification in $epK^+(X)$ missing mass. The values of the applied cuts are shown in Table 4.2. The filtering selected about 82,000 events for future analysis. The size of this data sample is compact and easily manageable (∼0.5 GigaBytes). This is very important considering that the size of entire reconstructed data set is close to a TeraByte.

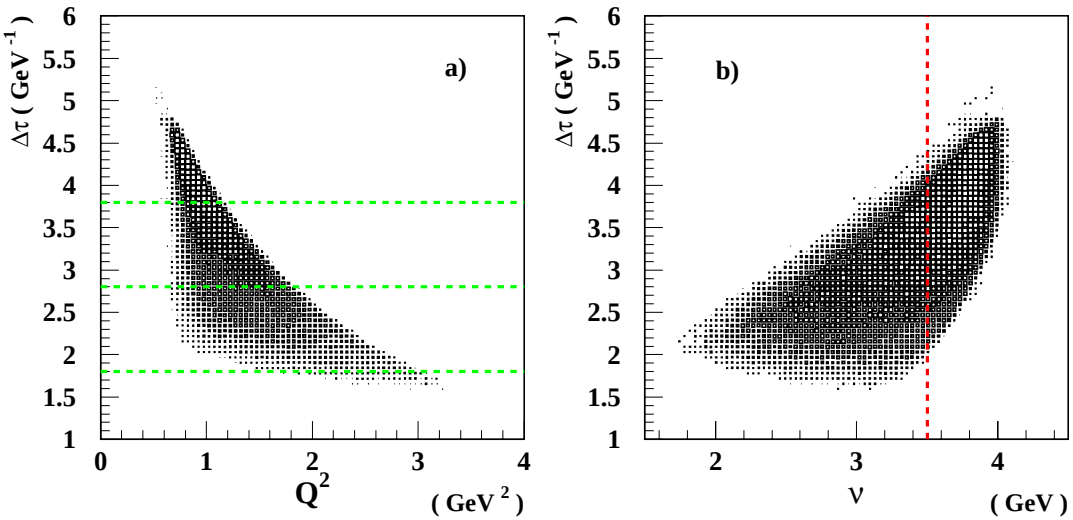

Figure 4.3: Kinematic distributions of the filtered epK^+K^- event sample: a) $\Delta\tau$ versus Q^2 . The dashed green lines show the binninig in $\Delta\tau$. b) $\Delta\tau$ versus ν. The dashed red line shows the kinematic cut in ν.

The Figures 4.2 and 4.3 show the kinematic ranges of the filtered event sample in the electroproduction variables: W, Q^2, ν and $\Delta\tau$. One can see that this is a very interesting kinematic region: CLAS data overlaps previous measurements at low Q^2 of 0.9 GeV^2 and extends it up to 2.5 GeV^2 [5, 6] (see Figure 4.2a). Moreover, CLAS has a very good acceptance in ν, and covers a W range from the ϕ threshold of about 2 GeV up to 2.7 GeV. In $\Delta\tau$ CLAS data extends from approximately 1.8 to 4.5 GeV^{-1} (see Figure 4.3).

Another important point in the filtering approach is the advantage of good particle identification (PID). It arises from the constraints of total energy and momentum conservation which considerably reduces the background of the final state of interest. The PID quality in the

filtered data sample is shown in Figure 4.7a. The K^+, π^+ and proton bands are clearly distinguished. The absence of systematic momentum dependence on the reconstructed particle mass is result of precise TOF calibration.

A detailed monitoring of the data quality was an important part of filtering procedure. In this stage the monitoring was performed with the data taking at about 10 second interval. The output of the monitoring contained a summary for every scaler event with differential number of events, accumulated beam charge, DAQ life-time, number of the epK^+K^- candidates and number of deuterons. These summaries were used for precise calculation of the integrated luminosity and the empty target contribution in the total rate.

The filtering procedure was accomplished for both production and empty target data , using "C" codes which were run on the Jefferson Lab CPU farm as a part of production PROD-1-9 processing of the data. For the reconstruction, the PID package from the off-line CLAS software was used (PART and TBID BOS result banks).

4.2 Analysis Procedure

To be consistent with the reconstruction and filtering procedures, the PROD-1-9 software library was used for the analysis of both real and simulated data. The full analysis procedure was repeated for data samples binned in Q^2 and $\Delta\tau$ in the same W range as shown in Table 4.3. The data binning in W and Q^2 variables is illustrated in Figure 4.2a. The data set of the filtered candidates for the epK^+K^- final state was used as analysis input. Because of the limited statistics it was not possible to have finer binning. The cross-sections as functions of Q^2 and $t' =\mid t - t_{min} \mid$, Φ and helicity angular distribution in $cos\theta_H$ (see Figure 1.1 for the angle definition) have been extracted. The data, binned in the two bins of Q^2 and $\Delta\tau$, were used to extract t-slope dependence. The entire data sample was used to extract the cross-section dependence on Q^2, $cos\theta_H$ angular distribution and study the different production mechanism contributions in the transition region.

Table 4.3: Binning of the data sample.

data binning	W range (GeV)	Q^2 range (GeV^2)	$\Delta\tau$ range (GeV^{-1})
Low Q^2 bin	2.0 – 2.6	0.7 – 1.2	NA
High Q^2 bin	2.0 – 2.6	1.2 – 2.2	NA
Low $\Delta\tau$ bin	2.0 – 2.6	NA	1.8 – 2.8
Low $\Delta\tau$ bin	2.0 – 2.6	NA	2.8 – 3.8

4.2.1 Kinematic Cuts

In order to minimize the event loss very few kinematic cuts were used:

ν cut. A large number of background events, with apparent high values of ν, were rejected by cutting events with $\nu > 3.5$ GeV. The nature of the background is shown in Figure 4.4. In order to extend the accepted W range of CLAS, the data were taken with lowest possible EC threshold in the trigger, which corresponds to 410 MeV of electron energy. The low threshold caused many false triggers initiated by the electrons from the $\pi^\circ \rightarrow \gamma e^+ e^-$ decay. As one can see in Figure 4.4a, the start-time of the high ν events is systematically distorted. This was choosen as criteria of the cut, shown with the solid red line. The reconstructed mass distribution for high ν events is shown in Figure 4.4b. The presence of the strong positron peak proves that these events contain e^+e^- pairs, which cause false triggers. The applied cut, $\nu < 3.5$ GeV, is shown in Figures 4.4a, 4.2b and 4.3b. We note, that with better systematic understanding of the CLAS detector and development of the reconstruction algorithms, this ν cut should be relaxed in order to accept the events with high values of W.

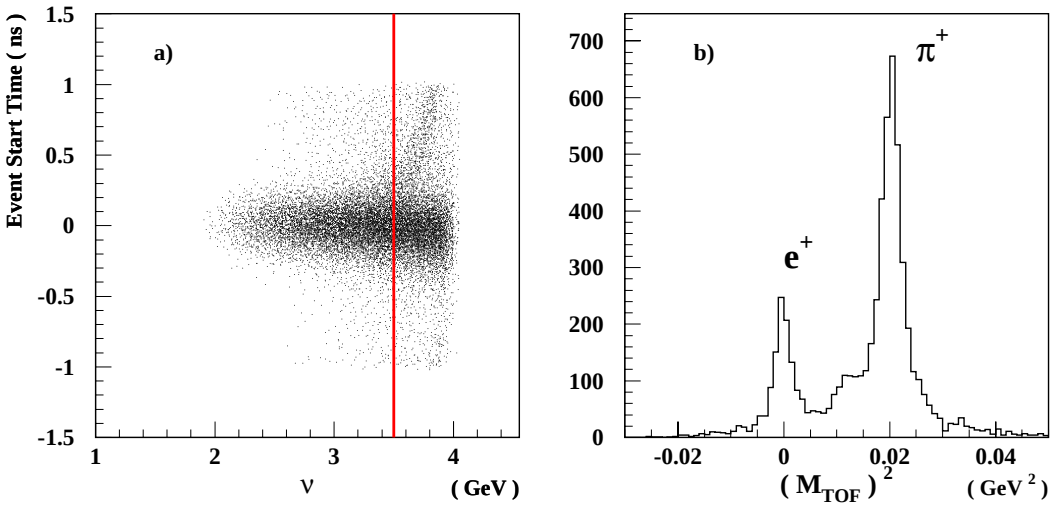

Figure 4.4: a) RF correction as function of ν. At $\nu > 3.5$ there is systematic distortion in the event start time calculation due to accidental background from previous and following beam bunches. The red line shows the applied cut. b) The positive particle reconstructed mass squared distribution for high ν events. Presence of the positron peak proves that high ν data is contaminated by e^+e^- pairs, which cause false triggers.

Q^2, W and $\Delta\tau$ cuts. These cuts were chosen to be consistent with the kinematic range for the epK^+K^- final state, a good acceptance regions of CLAS for the ϕ meson channel and the kinematic ranges of interest. We divided our data independently in two Q^2 and two $\Delta\tau$ bins, integration over W range from 2.0 to 2.6 GeV. The Q^2, W and $\Delta\tau$ cuts are shown in Figures 4.2a and 4.3a, and summarized in the Table 4.3. For each kinematic bin the data were analyzed independently.

$\pi^\pm$ exclusion cut. Charged pions in the event sample were identified by requiring the TOF reconstructed mass to be between 0.7 and 2.2 GeV (see Figure 4.7a). Using charge conservation we required no extra charged particles in the event. All events containing an extra π^+ or π^- were rejected. This cut improves the final PID and ϕ-signal to background ratio.

Electron Fiducial cut. The electron in the event was required to have a projected impact position on the front plane of the calorimeter at least 10 cm away from the edge. This cut is necessary by a few reasons. The first is unreliable electron identification near the EC edges because of electromagnetic shower leakage. The second reason is low efficiency of Cherenkov counters near the acceptance edge, which may create large systematic uncertainty in the acceptance. The third is charged particle interactions in the support material of EC and CC, which create false triggers. The effect of the fiducial cut is shown in Figure 4.5. One sees that this cut works mostly near the CC and EC acceptance edge.

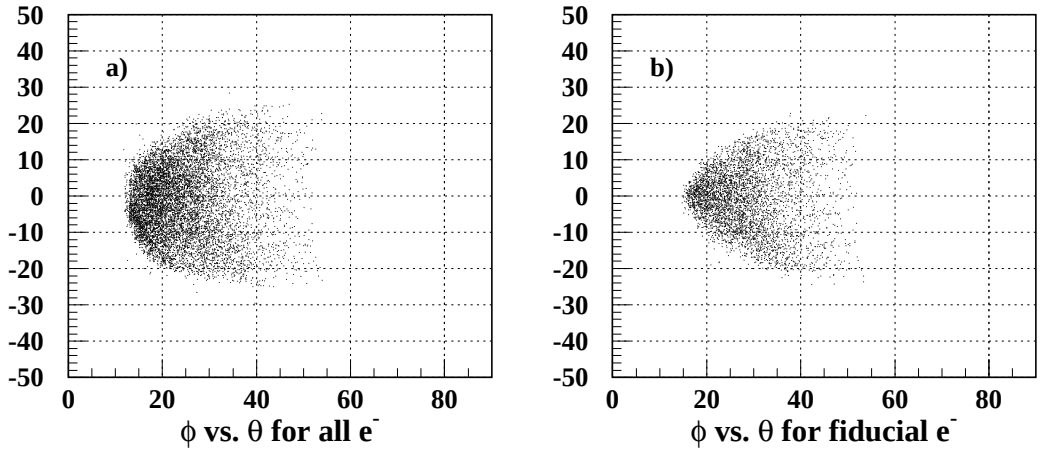

Figure 4.5: Effect of the fiducial cut for the electrons with $\nu < 3.5$ GeV (shown only for the sector number 4). a) All electrons; b) Electrons satisfying the fiducial cut.

4.2.2 Particle Identification (PID).

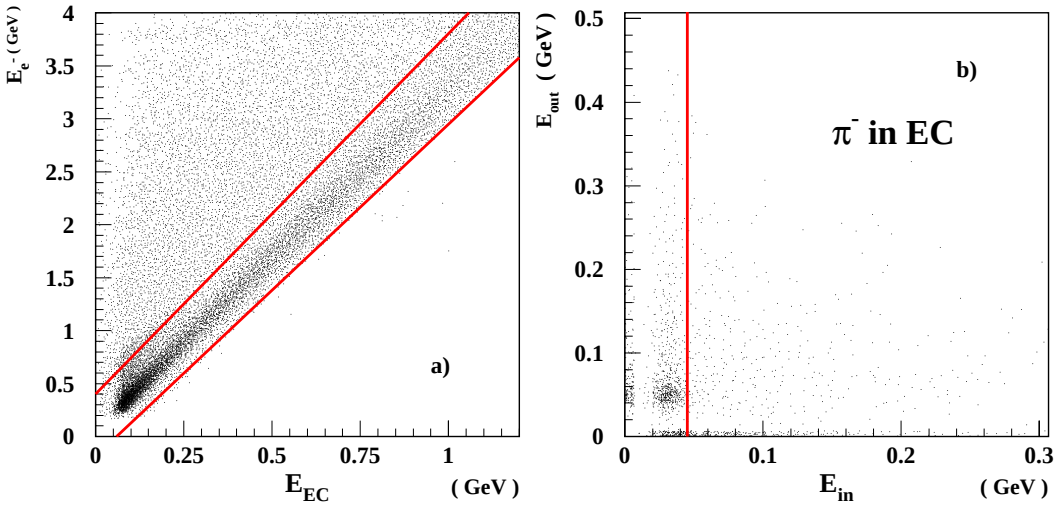

Figure 4.6: a) Electron energy versus total deposited energy in EC. The red lines show the applied cuts. b) Energy deposited by the TOF identified π^-'s in the outer EC layers versus energy deposited in the inner EC layers. The red line shows the applied cut $E_{in} > 0.04$ GeV.

Electron ID. In addition to the geomeric fiducial cut, cuts on energy deposition in EC were applied in order to avoid e^-/π^- misidentification. The total energy, deposited by electron in EC, is proportional to the electron energy. This dependence is illustrated by Figure 4.6a. The electron band with the width of EC resolution is clearly seen. In order to cut out hadronic background we applied cuts around this band (the red lines on Figure 4.6a). Additional improvement in e^-/π^- separation was made by cutting out the π^- signal on energy deposited in inner layer of calorimeter as shown on Figure 4.6b. The red line is

the applied cut $E_{in} < 0.04$ GeV, and the event cluster on the left of the line is the π^- signal in EC. To determine this cut we used π^- identified with TOF.

Hadron ID. The charged particle identification (PID) is shown in Figure 4.7 a-d. The positive charged particles momenta versus reconstructed mass distribution is shown in Figure 4.7a. Protons, kaons and positive pions bands are clearly distinguished. The width of the reconstructed mass increases with the momenta because of greater momenta uncertainty, but there is no systematic dependence of the mean value on the momenta. This indicates high quality of the TOF and RF calibrations.

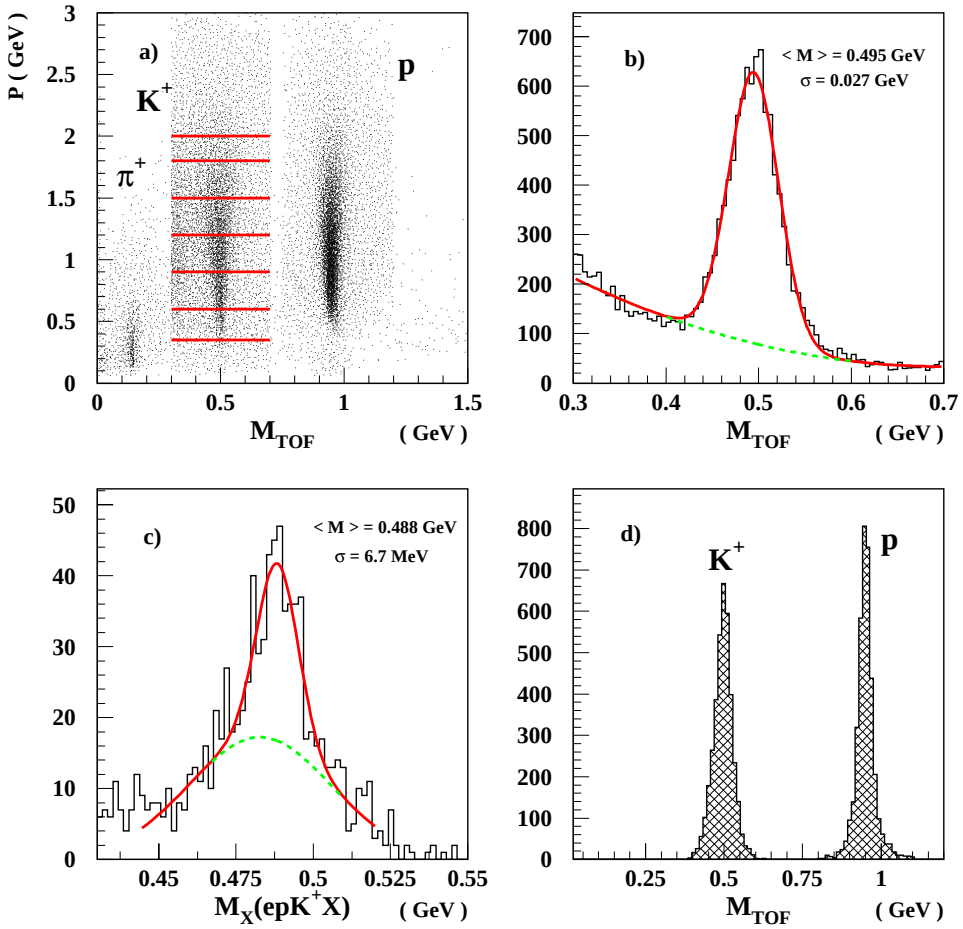

Figure 4.7: a) Positive-charged particle momenta versus reconstructed mass for the filtered event sample. The red lines shows the PID binning in kaon momenta; b) K^+ reconstructed mass distribution in its momenta bin from 0.9 to 1.2 GeV. The line shows the fitting results. c) epK^+X missing mass. The solid red line is the total fit and the dashed green line shows the background contribution; d) Proton and K^+ reconstructed mass distribution in identified epK^+K^- final state.

K^+ ID. In order to optimize the signal-to-background ratio in kaon PID, the kaon momenta range was divided into six bins. The mass distribution was fitted in each bin to determine the characteristics of the K^+ peak and the background contribution. An example of this procedure is shown in Figure 4.7a-b. The red lines in Figure 4.7a show the used momentum bins for K^+ PID, and the fitting results for one of the bins are illustrated in Figure 4.7b. To identify kaons, $< m_{K^+} > \pm 2\sigma$ cuts were applied. We note that this procedure was repeated for Monte Carlo data, where the reconstructed resolution might differ quantitatively from the real data. The use of criteria based on cuts derived from the measured widths, σ, allows us to repeat statistically equivalent cuts on simulated data for the acceptance calculation.

Proton ID. The proton signal is very clean and does not have any significant background contibution. For proton identification we applied a simple reconstructed mass cut from 0.8 to 1.1 GeV.

K^- ID. Because K^-'s bend inward toward the beam, CLAS had a very small acceptance for negative particles. Therefore we identified K^-'s using the missing mass technique. The epK^+ missing mass distribution is shown in Figure 4.7c. Similar to K^+ PID, in order to understand the signal and background contributions we fit the K^- peak, and applied $< m_{K^-} > \pm 2.5\sigma$ cuts. We note that the measured K^- mass at 485 MeV is a result of some remaining systematics in the reconstruction of the data. As we use the fitting criteria for our cuts, this has no dirrect affect on this analysis.

All applied PID cuts are summarized in Table 4.4.

Table 4.4: Final PID cuts applied to the data sample.

Quantity	Low cut	Upper cut
M_{K^+} (GeV)	-2σ	+2σ
$0.35 < P_{K^+} < 0.6$ (GeV)	0.478	0.523
$0.6 < P_{K^+} < 0.9$ (GeV)	0.462	0.532
$0.9 < P_{K^+} < 1.2$ (GeV)	0.441	0.549
$1.2 < P_{K^+} < 1.5$ (GeV)	0.426	0.564
$1.5 < P_{K^+} < 1.8$ (GeV)	0.403	0.594
$1.8 < P_{K^+} < 2.0$ (GeV)	0.388	0.627
M_p (GeV)	0.8	1.1
M_X[epK$^+$X] (GeV)	-2σ	+2σ
M_ϕ (GeV)	-2σ	+2σ

4.2.3 The ϕ Channel Identification and Background Subtraction

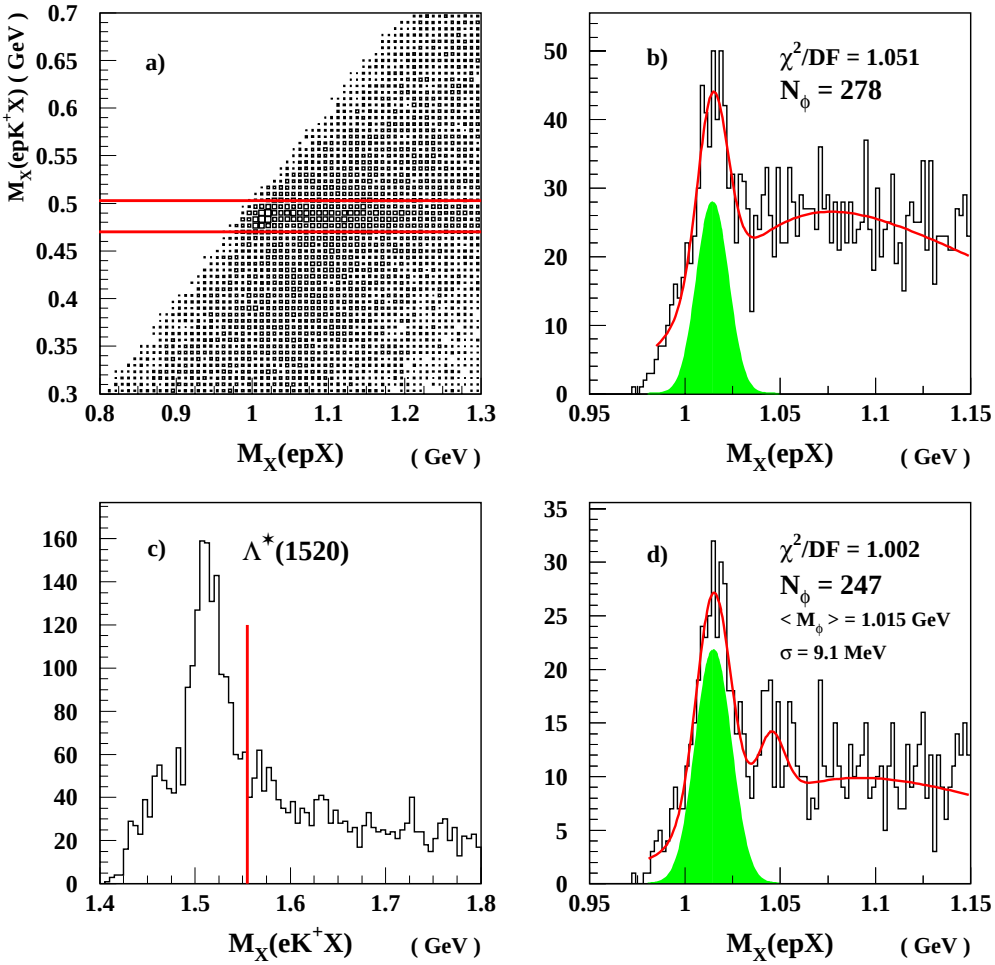

Figure 4.8: The ϕ channel separation technique. a) epK^+X missing mass versus epX missing mass. The red lines are the K^- PID cuts. b) epX missing mass of epK^+K^- final states. c) eK^+X missing mass distribution. The red line shows the $\Lambda^\star(1520)$ cut. d) epX missing mass distribution with applied $\Lambda^\star(1520)$ cut.

The epK^+K^- Final State. Applying all kinematic, fiducial and PID cuts, described above, we identified about 3800 events of the epK^+K^- final state. This sample includes the ϕ meson, the high mass hyperons production channels (see Section 4.2.3 for the description of the hyperons contribution in epK^+K^- final state), and accidental background, which comes from particle misidentification. The most important features of the identified final state are shown in Figure 4.8 a-c. On the scatter plot of epK^+X versus epX missing mass (Figure 4.8a) the signal of the epK^+K^- final state is clearly distinguished from the the rest of the data as the ϕ peak and the tail of the hyperons contribution. The red lines show the $\pm 2\sigma$ cuts in the reconstructed K^- mass. Figure 4.8b shows the epX missing mass distribution of

the selected final state with a prominent ϕ meson peak. Fitting simultaneously the peak with a Gaussian (integral is shown as green area on the plot) and the background with Landau function, we extracted the total ϕ yield in the entire data set as:

$$N_\phi = \frac{(A \cdot \sqrt{2\pi\sigma^2})}{\Delta_{bin}},$$

where A and σ are the height and the width of the Gaussian respectively, and Δ_{bin} is the histogram bin size. The fit gives $N_\phi = 278$, mean value $< M_X(epX) > = 1.015$ GeV and $\sigma = 8$ MeV. The ϕ-signal to background ratio is 1.1 within $\pm 2\sigma$ from the mean value of the ϕ peak. The mean value differs from M_ϕ due to remaining systematics in momentum measurement, and the width of the peak is dominated by CLAS resolution.

Ideally, having enough statistics and understanding of the background shape, one would like to repeat this fitting procedure for every bin of each kinematic variable of interest, and extract the ϕ yield without any direct background subtraction. With low statistics it is not possible, and only the missing mass method can be used [6]. This method includes three main steps: reduction of the hyperon contribution, separation of ϕ channel by a missing mass cut around the ϕ peak, and side-bin background subtraction in every distribution of interest. Here, we will illustrate the application of the method using the entire event sample. Similar analysis are done for each kinematic bin.

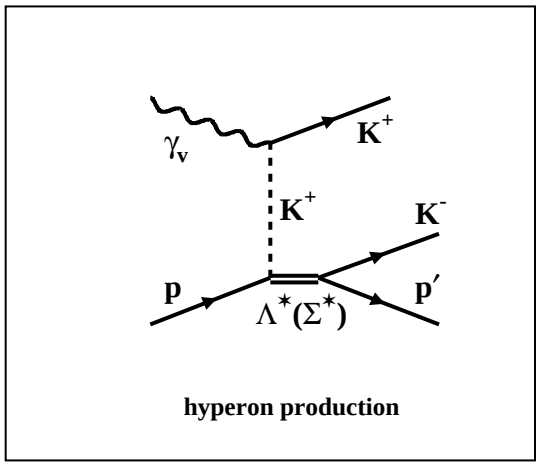

Figure 4.9: Feynman diagram for exited state hyperon production, which is the primary background channel to the ϕ reaction.

High Mass Hyperon Background. The production of epK^+K^- final state may proceed through various channels in addition to the ϕ meson production. They must be understood well in order to subtract them from the signal of interest. The primary background channel

in this case is the production of high mass strange baryons: $ep \rightarrow e'\Lambda^\star(\Sigma^\star)$, which decay $\Lambda^\star(\Sigma^\star) \rightarrow N\bar{K}$. The Feyman diagram of these processes is shown in Figure 4.9. The main source of the background is $\Lambda^\star(1520)$, which total cross section is comparable with that of ϕ. Additional contributions in background come from $\Lambda^\star(1600)$, $\Lambda^\star(1800)$, $\Lambda^\star(1820)$, $\Sigma^\star(1660)$ and $\Sigma^\star(1750)$ [52]. In a previous exclusive measurement [6] the requirement for $eK^+(X)$ missing mass to be larger than 1.6 GeV/c^2 was used to cut out the $\Lambda^\star(1520)$ events from selected epK^+K^- final state [1]. We also use this method in the present analysis because of limited statistics. The primary disadvantage of this approach is the exclusion of a fraction of the ϕ events due to this cut. However, the missing mass cut greatly reduces the $\Lambda^\star(1520)$ contribution under the ϕ peak.

Table 4.5: The high mass excited hyperon states, and relative yield used to generate events for background studies.

State	BR $N\bar{K}$ (%)	Relative yield (for $\Lambda^\star(1520) = 1$)	Number of events in background sample
$\Lambda^\star(1520)$	45	1.00	95318
$\Lambda^\star(1600)$	22	0.51	23766
$\Lambda^\star(1670)$	20	0.34	14403
$\Lambda^\star(1690)$	25	0.17	9002
$\Lambda^\star(1800)$	32	0.29	19656
$\Lambda^\star(1820)$	60	0.28	35585
$\Lambda^\star(1830)$	7	0.27	4003
$\Lambda^\star(1890)$	27	0.23	13154
$\Sigma^\star(1660)$	20	0.33	13979
$\Sigma^\star(1670)$	10	0.33	6989
$\Sigma^\star(1750)$	25	0.34	18004
$\Sigma^\star(1915)$	10	0.21	4448
$\Sigma^\star(1940)$	13	0.20	5507

In order to understand the background contributions, we generated Monte Carlo data of the ϕ and background channels separately. We could then study the signal and the background properties independently and in combination. The ϕ event sample was generated assuming VMD model (see Subsection 4.2.4) and the background states were generated with the CELEG event generator. The generated background states with their relative amplitudes are shown in Table 4.5. Only the states, which have large branching ratios for decay into the $N\bar{K}$ channel in this kinematic regime, were selected [52]. All generated events were processed with exactly the same code as the data (PROD-1-9 production library of CLAS

[1] This method was applied to the first available data at 4 GeV with CLAS (E1a, 1998). The results can be found in Reference [67].

software). For the background studies the ϕ meson and hyperon events were mixed together under the assumptions that the ratio of ϕ to $\Lambda^\star(1520)$ yield is approximately 0.5 [68], and the amplitude interference terms between the ϕ meson and hyperon states are small.

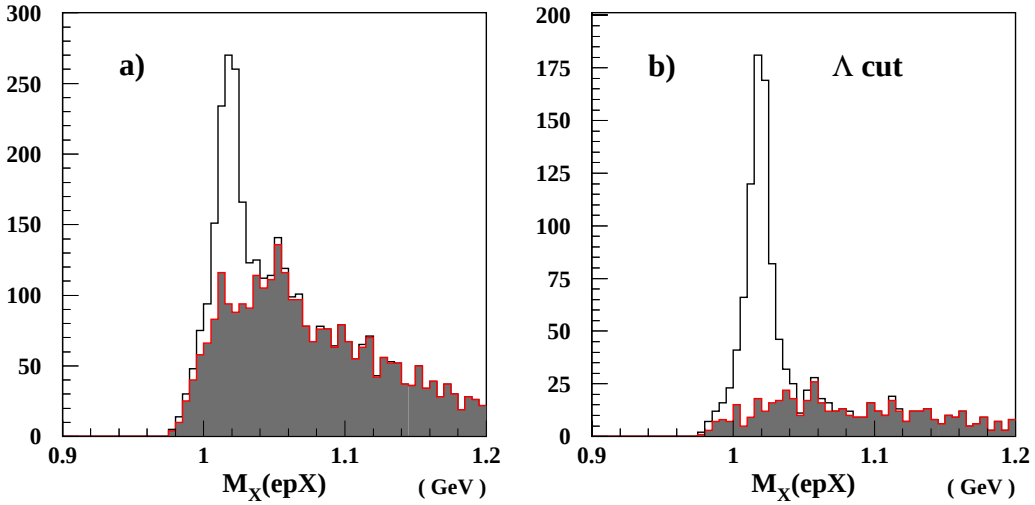

Figure 4.10: The simulated epK^+K^- final state: ϕ and high mass hyperons. a) and b): ϕ signal and high mass hyperon background (filled histogram) before and after $\Lambda^\star(1520)$ cut respectively. The Monte Carlo data do not include the background due to kaon misidentification.

The efficiency of eK^+X missing mass cut applied to the simulated data is show in Figure 4.10. Plot a) shows the epX missing mass distribution for the entire simulated event sample and the hyperon background (filled histogram) before the cut, and plot b) contains the same distributions but after $\Lambda^\star(1520)$ cut was applied. The remaining background of high mass hyperon states is smoothly distributed in phase-space, and its contribution under the ϕ peak is reduced from 50% to about 13%. Because of the restriction in the eK^+ phase-space, the ϕ meson yield is also decreased by amount of approximately 10%.

The $\Lambda^\star(1520)$ contribution in the epK^+K^- final state of the data sample is illustrated in Figure 4.8c. The strong $\Lambda^\star(1520)$ peak in the eK^+X missing mass distribution indicates that this reaction yield is comparable with that of ϕ in this kinematic regime. In order to exclude $\Lambda^\star(1520)$ contribution in the selected sample we require $M_X(eK^+)$ to be greater than 1.56 GeV. The cut is shown with the red line. However, the other excited hyperon states can contribute to the background under the ϕ meson peak.

Accidental Background. The epX missing mass distribution of experimental data with applied $\Lambda^\star(1520)$ cut is shown in Figure 4.8d. The simultaneous fit of the ϕ peak and the background gives $N_\phi = 247$, mean value, $< M_X(epX) > = 1.015$ GeV, and $\sigma = 9.1$ MeV. The background function was modified by an additional Gaussian in order to fit the structure due to remaining high mass hyperon contribution (see Figures 4.8d and 4.10). The decrease in ϕ

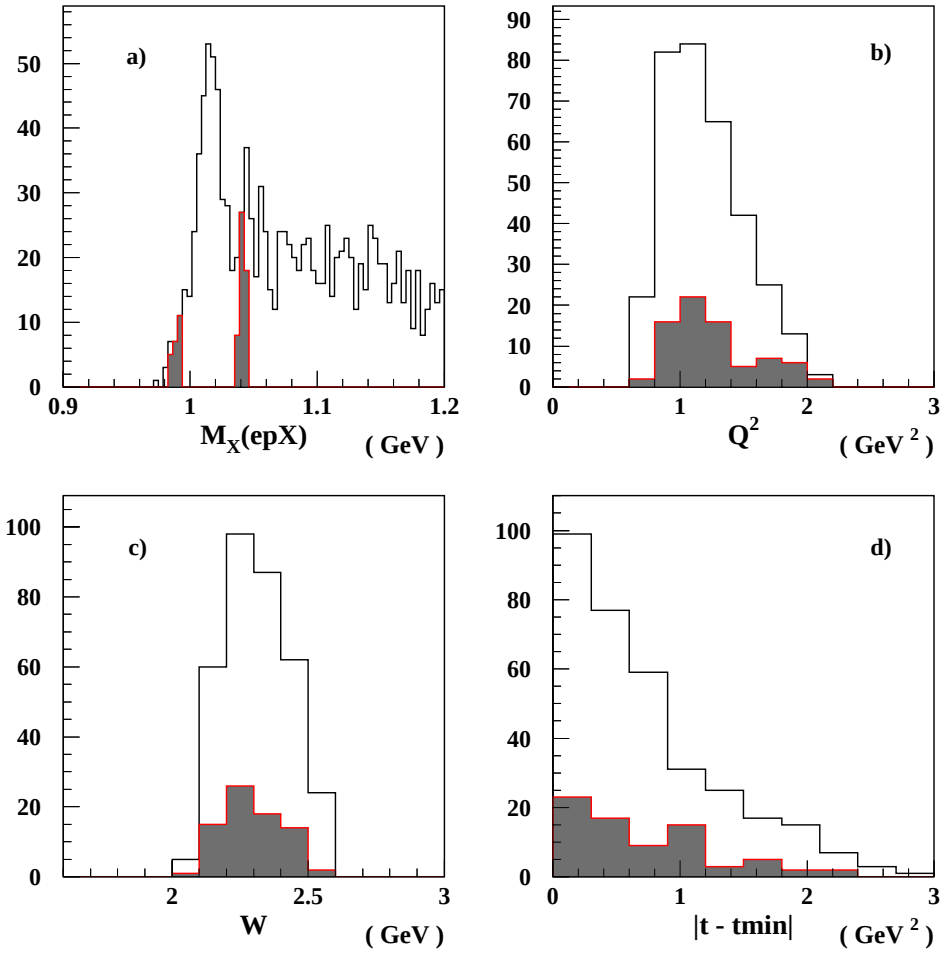

Figure 4.11: Side-bin background subtraction technique: a) Side bins location; b), c) and d) Propagation of the side bins events into Q^2, W and $\mid t - t_{min} \mid$ distributions respectively.

meson yield of about 11% is consistent with the estimate from Monte Carlo simulation. The ϕ signal to background ratio is improved and equals to 2.5 within $\pm 2\sigma$ from the mean value of the ϕ peak. Since the hyperon states contribution is on the level of 13%, the remaining background is due to particle misidentification. This background, so called "accidental", is part of the selected epK^+K^- final state.

Separation of ϕ channel and Background Subtraction. To separate ϕ events we used the $\pm 2\sigma$ cut around the $< M_\phi >$ in the epX missing mass after excluding the $\Lambda^\star(1520)$ from the final state data sample. These separated events were used to extract the results for ϕ meson production. The side-bin technique, illustrated in Figure 4.11, was used for the background subtraction. In order to avoid the ϕ signal subtraction from itself the close to ϕ peak side-bin edges were located $\pm 2.5\sigma_\phi$ away from the peak. The width of the bins was adjusted to the amount of the background events under ϕ meson peak, extracted from the

Table 4.6: Summary of the ϕ yield and signal to background ratio.

Data bin	ϕ yield	ϕ to background ratio
All data	247	2.5
Low Q^2	114	2.1
High Q^2	130	6.5
Low $\Delta\tau$	141	7.7
High $\Delta\tau$	113	2.2

fit (see Figure 4.8d). The summary of the ϕ yield and signal to background ratio is shown in Table 4.6. The selected side-bin events were propagated and subtracted in every distribution of interest. An example of ϕ channel identification and the background propagation into Q^2, W and $\mid t - t_{min} \mid$ distributions for the entire data sample are shown in Figure 4.11. The same procedure was repeated for each kinematic region.

In order to estimate the systematic errors of this technique, we used a different fit of the background with Landau function alone. From the comparison of the analysis results with different amount of subtracted background, the systematic errors of this method are about 20%. This is the main contribution in systematic uncertainty of our results.

4.2.4 Acceptance Calculation

The procedure. For the acceptance calculation one million Monte Carlo (MC) events were generated and propagated through GSIM, a GEANT-based simulation code for CLAS, and then through GSIMKO, the code which removes non-functional and problematic detector channels from simulated data and smears the drift chamber space resolution. For this analysis the dead wires of the drift chambers and dead scintillator counters were removed, and 1000 μm for DC smearing was used. The results of data monitoring and DC calibration were used for this procedure. The simulated events were then processed with the same PROD-1-9 version of the off-line code and the same cuts were applied as for the real data (see Sections 4.2.1 and 4.2.2). In each kinematic region the acceptance was calculated for every bin of each distribution from the ratio of reconstructed over generated ϕ events.

An example of the acceptance calculation for $\mid t - t_{min} \mid$ in the high Q^2 kinematic region is shown in Figure 4.12. The acceptance function in this variable is smooth and flat everywhere except at one very high value of $\mid t - t_{min} \mid$. Because of large statistical errors the last two bins at high values of $\mid t - t_{min} \mid$ were not included in the extraction of results. The same procedure was used to calculate the acceptance functions of Q^2, W, $\Delta\tau$, ϵ, Φ, $cos\theta_H$ and Ψ in all defined kinematic bins. The average acceptance of ϕ meson channel is about 5%.

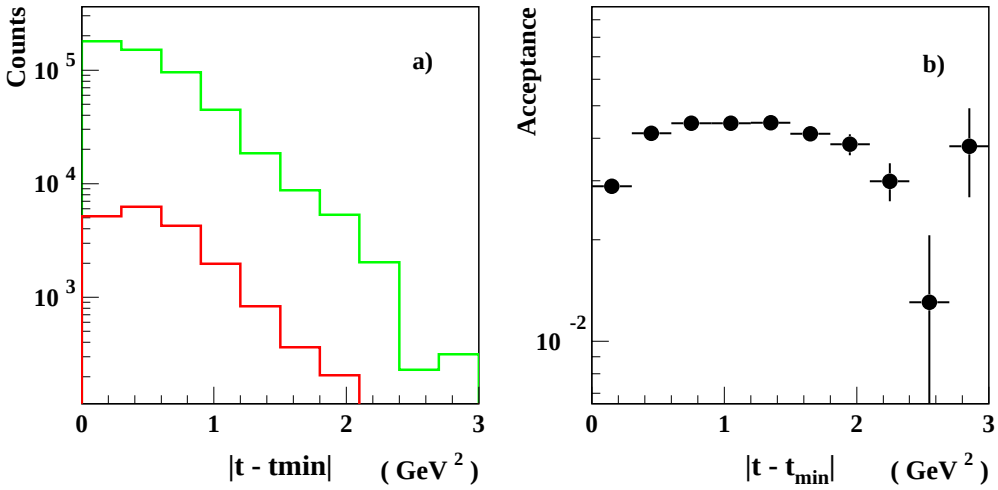

Figure 4.12: Acceptance calculation of $\mid t - t_{min} \mid$ in the high Q^2 kinematic region. a) Generated event distribution (green line) and reconstructed event distribution (red line); b) Acceptance function versus $\mid t - t_{min} \mid$ calculated as ratio of reconstructed to generated ϕ events. Only the region of smooth acceptance, from 0 to 2.3 GeV^2 was used in analysis.

Table 4.7: Kinematics and VMD model parameter values of ϕ meson generated events

Beam energy (GeV)	4.247
Target	proton
Q^2 range (GeV^2)	0.7 – 3.0
ν range (GeV)	1.5 – 4.2
t range (GeV^2)	-4.0 – 0.0
R	1.3
b (GeV^{-2})	1.5

Kinematic Correlations. The MC event sample was generated [2] assuming VMD model for ϕ electroproduction. Table 4.7 shows the important values for generated events. Two iterations in the acceptance calculation were made to adjust the VMD parameters to be close to that of the data. Because of the integration over the different kinematic variables and complicated topology of the events, this was a very important step.

An example of a strong acceptance dependence on angular correlations is shown in Figure 4.13 as an example of extreme importance of model adjustment. Because of the CLAS toroidal magnetic field, symmetric respect to the direction of the beam, the reconstruction efficiency of K^+K^- pair from ϕ meson decay depends strongly on the difference in laboratory polar angles of the charged kaons, (θ_{K^+} - θ_{K^-}). Because of small opening angle in laboratory,

[2] We used the ϕ event generator code, written by M. Morlet, J. Van de Wiele and M. Guidal (IPN Orsay).

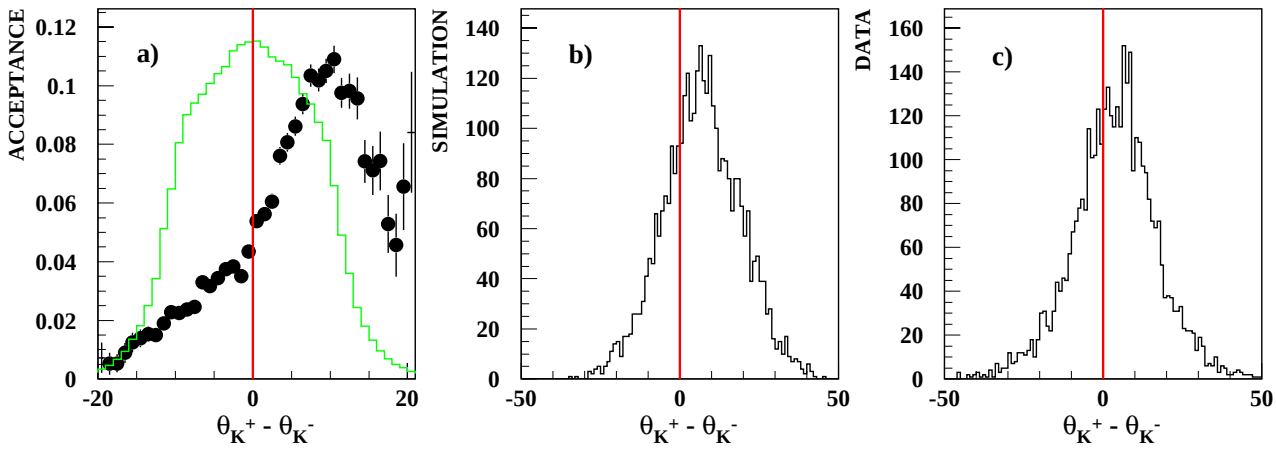

Figure 4.13: Acceptance dependence on $(\theta_{K^+} - \theta_{K^-})$ in laboratory coordinate system: a) Solid green line is the generated ϕ event distribution ($\times 10^5$) and solid circles are the calculated acceptance; b) Simulated epK^+K^- final state; c) Experimental data: epK^+K^- selected final state.

when this difference is negative the K^+ and K^- tracks cross each other in the DC of CLAS, and when it approaches zero the tracks are located very close. This topology results in reconstruction inefficiency, e.g. in Figure 4.13a: the original generated distribution (solid green line) gets distorted, and the ϕ acceptance drops rapidly, about a factor of five. This effect explains the low average acceptance of ϕ meson channel. However, the complete simulation of the epK^+K^- final state, including ϕ and high mass hyperon states (see Section 4.2.3), reproduces the data behavior very well, Figure 4.13b and c. Close matching of the simulation and the experimental data confirms the reliability of the calculated acceptance functions [3].

Trigger Efficiency Simulation. The event trigger in this experiment required the coincidence of CC and EC signals within one sector. The EC triggering efficiency for the electron is close to 100%, but for CC efficiency can be significantly lower near the geometric acceptance edges. During CC calibration its efficiency was mapped for and stored in the off-line data base.

Because of limited statistics we could not restrict the electron fiducial cut (see Section 4.2.1), and in order to correct the data for the trigger inefficiency, during acceptance calculation, we simulated CC efficiency on event-by-event basis using the CC calibration results. Two Q^2 simulated distributions, with and without CC inefficiency correction, are shown in Figure 4.14a, and their ratio is shown in Figure 4.14b. At large values of Q^2 this correction factor is of order of 6%, but at large Q^2 the correction becomes larger. The dashed red line in Figure 4.14b shows the low limit in Q^2 for the differential cross-section extraction.

[3]Independent studies of the correlation effects in CLAS acceptance, made by Sacley group for the ϕ photoproduction at high momentum transfer, are consistent with our results [70].

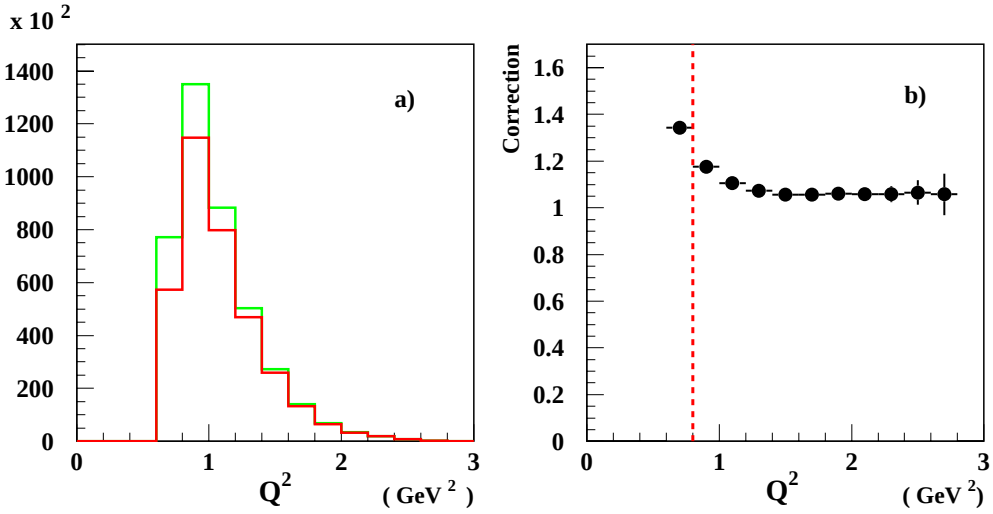

Figure 4.14: Correction on CC efficiency. a) The Q^2 distributions without (green) and with CC efficiency simulation (red). b) The CC efficiency correction factor versus Q^2. The dashed red line shows the low limit in Q^2 for the differential cross-section extraction.

4.2.5 Energy Loss in the Detector

The energy loss in the liquid hydrogen of the target and in the drift chambers of CLAS can affect the missing mass values. Because of the configuration of the magnetic field in CLAS, only material between the target and R3 of the DC can affect the measured momenta. The effect of momenta losses before entering R3 of the DC as a function of momenta for protons and kaons is shown in Figure 4.15 (the energy loss for the electrons is very small). The calculation for the protons has been done with a GEANT based Monte Carlo program (dashed line in Figure 4.15a) and with code, which calculates the averaged energy loss using the Bethe-Bloch formalism (solid squares in Figure 4.15a). For kaons the energy loss was calculated using only the last mentioned method (solid squares in Figure 4.15b). Because of the kinematics of the chosen reaction we see protons mostly with momenta above 0.5 GeV/c and K^+ PID starts above 0.3 GeV (see Figure 4.7a). The energy loss for this momenta regions is below 1% for both protons and kaons, and, it was tested, does not affect the missing mass information.

4.2.6 Empty Target Contribution

During the 1998 data taking, ice collected on the out-going target window, and the amount changed with time. Hence, it is very important to control the stability of the target status and to know the empty target contribution to the total ϕ rate for this data. For this purpose the empty target data were taken periodically through the run. The total accumulated charge on the empty target $Q^{empty} = 506.9$ μC, which is 43.4% of that accumulated on the

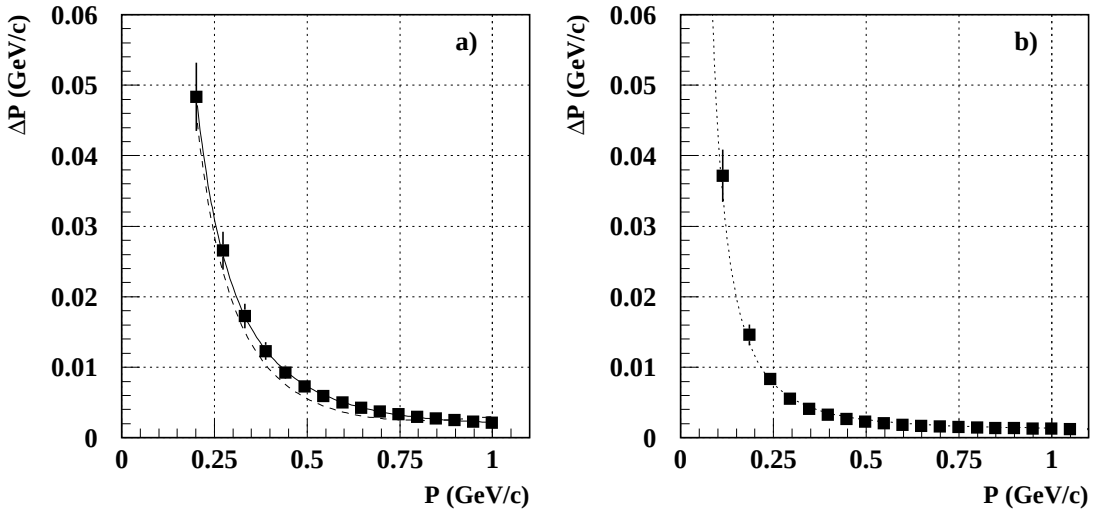

Figure 4.15: Lost momenta in detector media versus momenta of the particles: a) protons and b) kaons. Only target and detector components between the target and region 3 of the drift chambers were taken into account.

full target.

Target Stability. To monitor the stability of the target, we tracked the time dependence of the following rates: epK^+K^- event candidates, live-gated accumulated charge and deuteron rate. These rates were checked for production and empty target runs as well. The rate of deuteron-events, which can not come from the hydrogen target, was used to monitor background from the target windows. This procedure was performed on a run-by-run basis during the selection of epK^+K^- event sample (see Section 4.1.2). The results of this monitoring are shown in Figure 4.16. The empty target epK^+K^- event candidates rate in the preselected event sample was calculated as

$$R^{empty}_{K^+K^-} \;=\; \frac{N^{empty}_{K^+K^-}}{N^{full}_{K^+K^-}} \cdot \frac{N^{empty}_{d}}{N^{full}_{d}}\,(\%)\,, \tag{4.1}$$

where $N^{empty}_{K^+K^-}$ and N^{empty}_{d} are preselected event and deuteron rates in the empty target runs, and $N^{full}_{K^+K^-}$ and N^{full}_{d} are preselected event and deuteron rates in the full target runs. In the Figure 4.16 the empty target rate is plotted versus the data run number. One sees that the target conditions were stable within $\pm 0.7\%$ (dashed green lines), and the average empty target contribution in preselected epK^+K^- event rate is about 6 % (dashed red line). The target fluctuation of $\pm 0.7\%$ was added to the final systematic errors during data normalization.

Absolute contribution. Unfortunately, we could only put an upper limit on the absolute empty target contribution to the ϕ meson production rate. Performing the same analysis

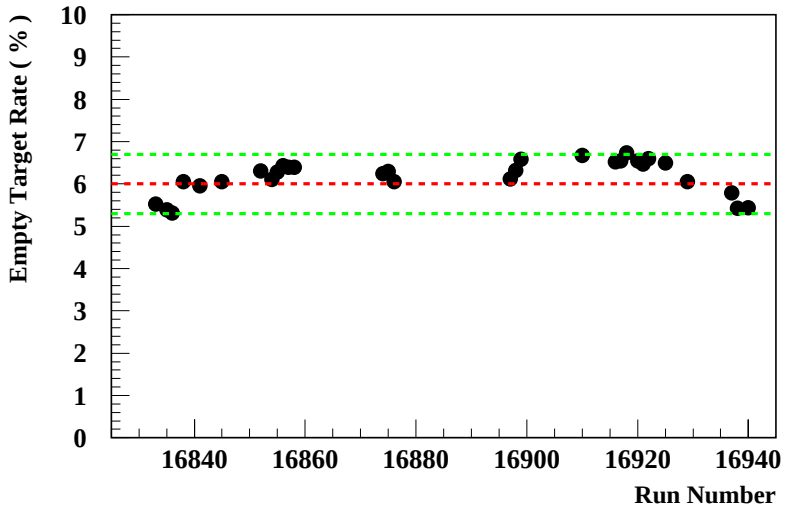

Figure 4.16: The empty target rate in preselected epK^+K^- event sample versus the run number. The average is about 6% of total rate (dashed red line).

on the empty target data as on the production data, we did not find any ϕ events. If one ϕ meson event was found, the upper limit for the absolute empty target contribution would be:

$$F^{empty} = \frac{Q^{prod}}{Q^{empty}} \cdot \frac{1}{N_\phi^{prod}} = 0.8\% \,, \tag{4.2}$$

where Q^{empty} and Q^{prod} are total accumulated charges on empty and filled targets, respectively, and N_ϕ^{prod} is the total number of ϕ events in the production data. This number was used as the average scale factor for the absolute empty target contribution to the ϕ production rate.

4.2.7 Data Correction Factors and Normalization

Normalization Procedure. The final step in analysis procedure was the normalization of the ϕ yield to the integrated luminosity, the virtual photon flux, and all calculated corrections as:

$$\frac{d\sigma(Q^2,W)}{dX} = \frac{1}{\Delta_X}\cdot\frac{1}{\Delta_{Q^2}}\cdot\frac{1}{\Delta_W}\cdot\frac{N_\phi}{\Gamma(Q^2,W)\cdot L_{int}}\cdot F_\phi^{acc}\cdot F_\phi^{empty}\cdot F^{rad}, \qquad (4.3)$$

where X is the variables of interest (W, Q^2, t' and $\Delta\tau$), Δ_X is its bin width, Δ_{Q^2} and Δ_W are the bin widths of Q^2 and W variables, $\Gamma(Q^2,W)$ is the virtual photon flux, L_{int} is the integrated luminosity, N_ϕ is ϕ yield in the bin, F_ϕ^{acc} is the acceptance factor in a given bin, F_ϕ^{empty} is the total empty target correction factor and F^{rad} is radiative correction factor. The integrated luminosity for the used data sample is $L_{int} = 1.486{\cdot}10^{39}$ cm^{-2} (see Equation 1.15). The virtual photon flux (see Equation 1.13) was calculated on an event-by-event basis averaging over measured Q^2 and W variables for each kinematic bin. The results are summarized in the Table 4.8.

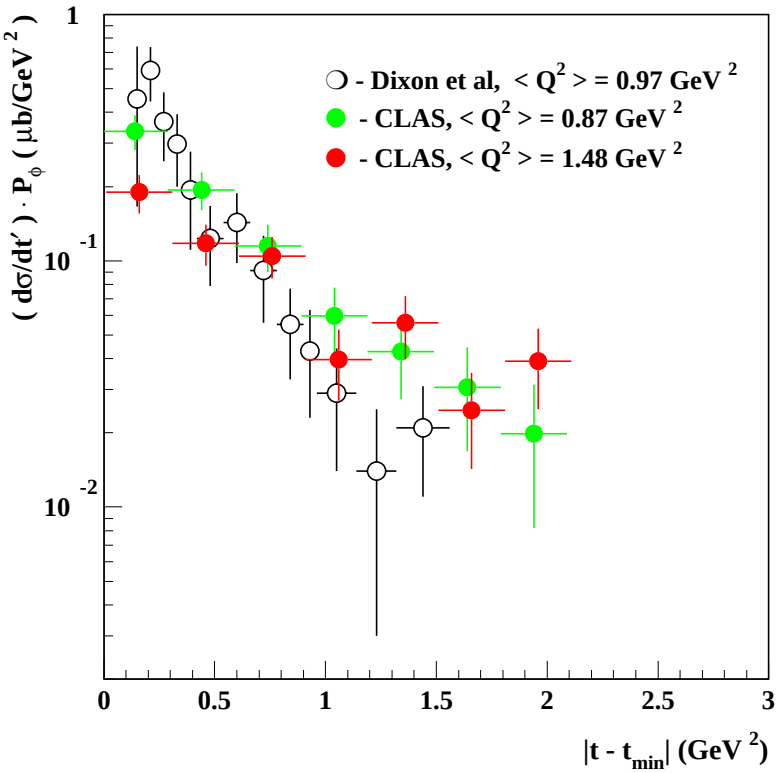

Figure 4.17: The $d\sigma/dt'$ differential cross-section with ϕ-propagator dependence removed.

Because of the same final state and close kinematics region in Q^2 and W kinematic variables, the radiative correction factor for the ϕ meson channel, in first order approximation, is the

same as for the $\Lambda^{\star}(1520)$ production. It has also been shown, that the radiative effects contribute uniformly over broad $\mid t - t_{min} \mid$ and Q^2 ranges [5, 68, 69]. For data normalization we used the value for $F^{rad} = 1.1$ from Reference [68]. Since this analysis is focused on the study of the $\mid t - t_{min} \mid$, Q^2 and angular distributions of ϕ meson decay, this approximation is safe.

Table 4.8: Mean values of Q^2, W, ϵ, $\Gamma(Q^2,W)$ and P_ϕ used for $d\sigma/dt'$ normalization.

Data bin	Q^2 (GeV^2)	W (GeV)	ϵ	$\Gamma(Q^2, W)$ (GeV^{-3}) $\times 10^{-3}$
Low Q^2	0.87	2.30	0.56	0.137
High Q^2	1.48	2.25	0.47	0.073

Differential Cross Section, $d\sigma/dt'$. The results of the measured differential cross-section, $d\sigma/dt'$, for low and high Q^2 kinematic bins are shown in Figure 4.17. In order to compare our results with the previous measurement [5], the Q^2 dependence of ϕ propagator,

$$\frac{1}{P_\phi} = \left(\frac{M_\phi^2}{Q^2 + M_\phi^2} \right)^2 , \tag{4.4}$$

was removed. The shape of our differential cross-sections $d\sigma/dt'$ is not consistent with the previous measurement [5], the slope of the distributions is systematically smaller.

Cross Section, $\sigma(Q^2)$. The cross-section, $\sigma(Q^2)$, was extracted in six bins over a Q^2 range from 0.8 to 2.0 GeV^2 with bin width of 0.2 GeV^2 and with an average value of W=2.3 GeV. The details of the cross-section normalization procedure is shown in Figure 4.18: the raw data and background distributions (a); the acceptance function versus Q^2 (b); the virtual photon flux in every Q^2 bin (c), and the resulting $\sigma(Q^2)$ cross-section (d). The values of the virtual photon flux, $\Gamma(Q^2,W)$, used during normalization, and of the measured differential cross-section are shown in Table 4.9.

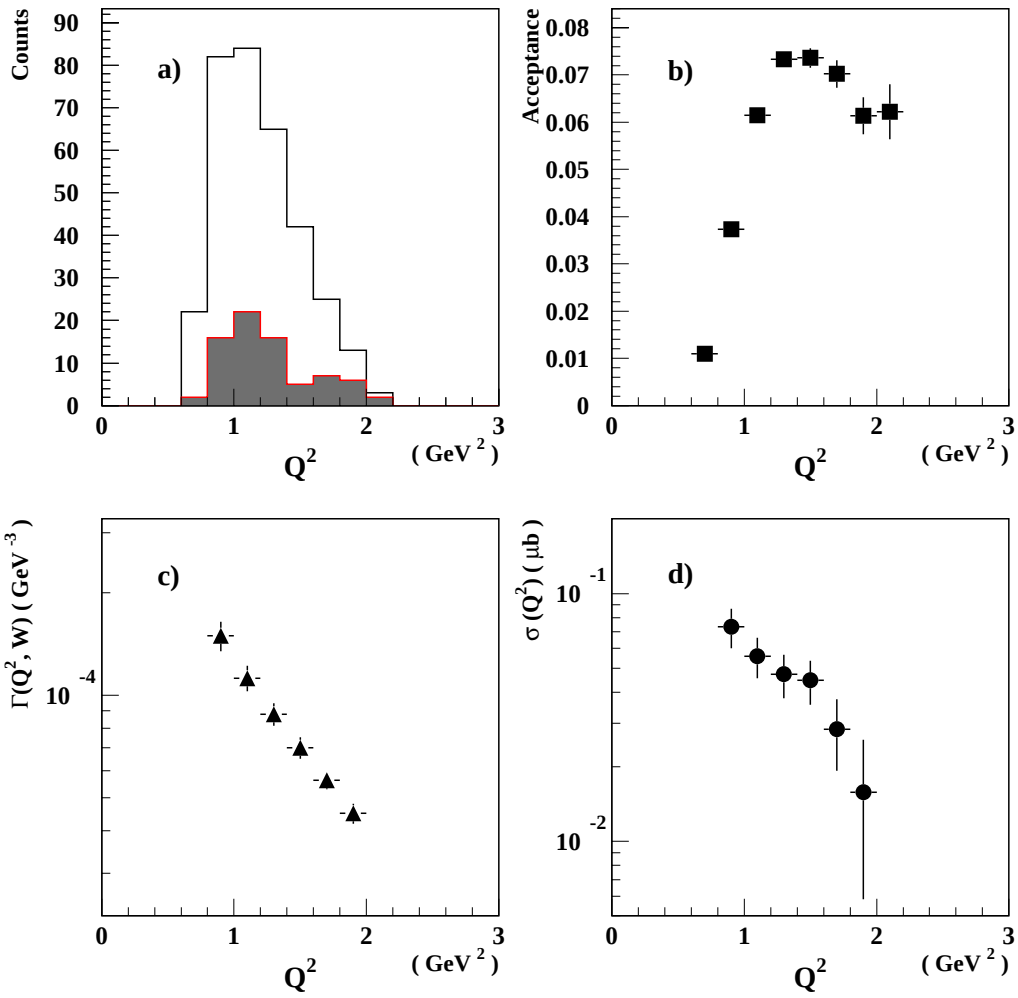

Figure 4.18: Q^2 normalization procedure. a) Raw ϕ data and the background events (filled histogram); b) Acceptance of CLAS versus Q^2; c) Virtual photon flux $\Gamma(Q^2,W)$ versus Q^2; d) The measured ϕ meson cross-section.

Table 4.9: Measured values of $\Gamma(Q^2,W)$ and $\sigma(Q^2)$ for a Q^2 range from 0.8 to 2.0 GeV^2.

Q^2 bin (GeV^2)	$\Gamma(Q^2,W)$ (GeV^{-3})	$\sigma(Q^2)$ (μb) $\times 10^{-2}$
0.8 – 1.0	$(1.50 \pm 0.15)\cdot 10^{-4}$	7.33 ± 1.32
1.0 – 1.2	$(1.12 \pm 0.10)\cdot 10^{-4}$	5.58 ± 1.05
1.2 – 1.4	$(8.79 \pm 0.67)\cdot 10^{-5}$	4.72 ± 0.94
1.4 – 1.6	$(7.01 \pm 0.50)\cdot 10^{-5}$	4.43 ± 0.89
1.6 – 1.8	$(5.62 \pm 0.33)\cdot 10^{-5}$	2.84 ± 0.91
1.8 – 2.0	$(4.50 \pm 0.30)\cdot 10^{-5}$	1.58 ± 0.99

Chapter 5

Physics Results

After the extraction of the ϕ meson yields, corrected for the background contribution, geometric acceptance of the detector, and all factors described in Section 4.2 we obtained the ϕ electroproduction differential cross-sections, $d\sigma/dt'$, for each kinematic bin, cross-section dependence on Q^2, $\sigma(Q^2)$, and the azimuthal angular distribution in $cos\theta_H$ for the Q^2 region from 0.7 to 2.2 GeV^2. The entire ϕ meson event sample lies in low $c\Delta\tau$ region below 1 fm, and the t-slope parameter, b_ϕ, is systematically lower than it was found in the previous measurements (see Figure 4.17). This observation makes the application of the standard VMD model in our kinematic regime doubtful. Therefore, we concentrated our analysis on understanding the t-slope parameter dependence on $c\Delta\tau$ and Q^2; comparison of the predictions by the VMD and Pomeron exchange models with the experimental data, and estimation of the non-diffractive ϕ meson production mechanisms contribution at high momentum transfer, t'.

5.1 The t-slope Dependence on $\Delta\tau$ and Q^2

Table 5.1: The fitted values of t-slope parameter, b_ϕ, in each kinematic region.

Data bin	Range	$<Q^2>$ (GeV^2)	$<c\Delta\tau>$ (fm)	b (GeV^{-2})	χ^2/DF
Low Q^2 (GeV^2)	0.7 – 1.2	0.87	NA	1.87 ± 0.33	0.33
High Q^2 (GeV^2)	1.2 – 2.2	1.48	NA	1.52 ± 0.32	1.22
Low $\Delta\tau$ (GeV^{-1})	1.8 – 2.8	NA	0.49	1.55 ± 0.31	0.08
High $\Delta\tau$ (GeV^{-1})	2.8 – 3.8	NA	0.64	1.91 ± 0.31	2.58

In order to compare our results with existing data we extracted the t-slope parameter values, b_ϕ, in each kinematic bin using the VMD predicted parametrization of the differential cross-

section at low t':

$$\sigma_{t'} \quad = \quad A_\phi \; exp(-\, b_\phi t') \; , \tag{5.1}$$

where $t' = \mid t - t_{min} \mid$ (see the definition of t and t_{min} in Section 1.1). To be consistent with the previous analysis, we fit the $\sigma_{t'}$ distribution in the range of $\mid t - t_{min} \mid$ from 0.0 to 1.1 GeV^2. The extracted values of b_ϕ are shown in Table 5.1. Within statistical errors they agree with the preliminary results of E1a data analysis reported in Reference [67]. Here we show only the statistical errors, the systematic errors are about 20%, due mostly to the uncertainty in the background subtraction technique (see Section 4.2.3).

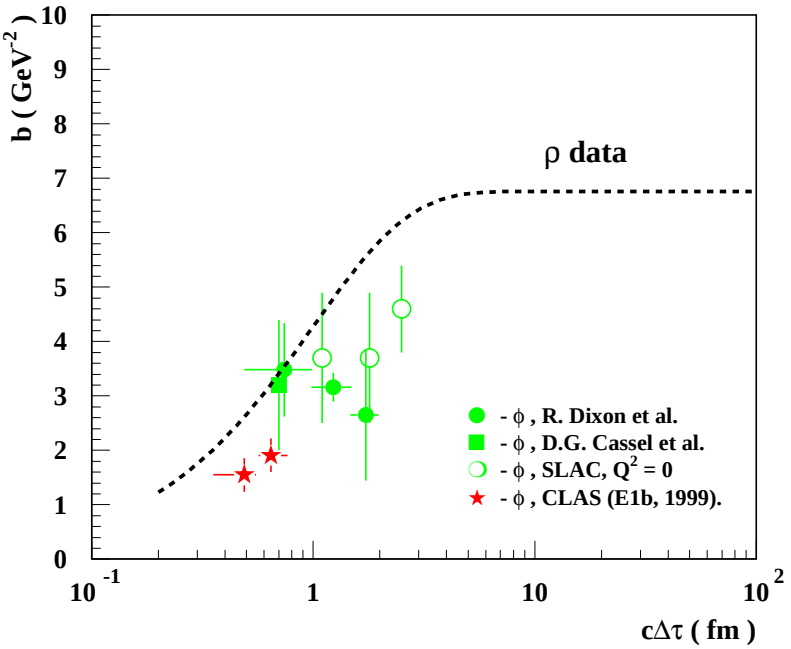

Figure 5.1: The dependence of b versus $c\Delta\tau$ for the ϕ and ρ meson production. The black dashed curve is the trend of the ρ meson production data [6]. The green symbols are the previous ϕ meson production data from References [6, 5, 72], and the red stars are the results of this experiment.

Dependence on $\Delta\tau$. The dependence of the t-slope, b_ϕ, on formation time, $c\Delta\tau$, for ϕ meson production is shown in Figure 5.1 in comparison with ρ meson production data. In the terminology of the uncertainty principle, $\Delta\tau$ is the time during which the virtual photon mass, $\sqrt{Q^2}$, can have the off-shell mass of a ϕ, $M_\phi = 1020$ MeV (for the definition of $\Delta\tau$ see Section 1.1). As we derived in Section 1.2.3 (see Equation 1.27), b_ϕ should decrease at low $\Delta\tau$, as the interaction becomes more point-like. The previous measurements (shown in green color) do not show the expected behavior. Both our data points (the red stars) lie in the region of $c\Delta\tau$ below 1 fm and show the decrease of b_ϕ with decreasing formation time. This, is consistent with well-measured dependence of ρ meson production (the trend is shown with the black dashed line), and with the simple model (see Section 1.2.3) as illustrated in Figure 1.7b.

Dependence on Q^2. A summary of the existing measurements of b_ϕ together with our results is shown in Figure 5.2. In contrast with the ρ meson production data, shown in Figure 1.9, the previous ϕ photo- and electroproduction measurements are consistent with no Q^2 dependences [1, 5]. Our data points are consistent with a low value of $b_\phi \approx 1.7$ GeV^2, which taken together with the slopes measured in photoproduction show a striking dependence on Q^2.

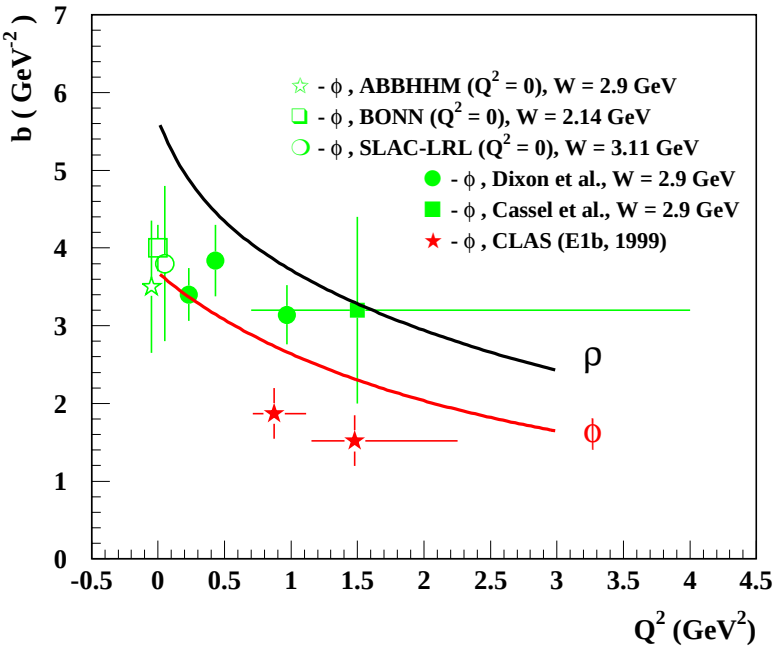

Figure 5.2: The dependence of b versus Q^2 for the ϕ and ρ meson production. The green symbols are the ϕ electroproduction data are from References [5, 6] and the photoproduction data from References [71, 72, 73]. The data of this experiment are shown with the red stars. The black curve is a fit to the ρ production data from References [6, 32, 75]. The red curve is a fit to all ϕ meson production data.

Only for comparison with previous conclusion in Reference [5] we fit all ϕ data points in Figure 5.2 to zero- and first-order polynomial functions. The zero-order polynomial fit gives

$$b_\phi = 2.92 \pm 0.14\,, \quad \chi^2/DF = 6.23\,, \tag{5.2}$$

and the first-order polynomial fit gives

$$b_\phi = (3.96 \pm 0.21) - (1.57 \pm 0.25)\; Q^2\,, \quad \chi^2/DF = 1.39 \tag{5.3}$$

with considerably smaller value of χ^2/DF. This result means that b_ϕ decreases with increasing Q^2, as it does for the ρ meson production [1].

[1] The same fits to the previous ϕ production measurements alone give very close values of χ^2/DF, which is consistent with no Q^2 dependence of b_ϕ. See for detail Reference [5].

To both ϕ and ρ meson production data we applied the formalism, developed in Section 1.2.3. Combining the Equations 1.27, 1.29 and 1.10, and factorizing out radius of the proton, r_h, we obtained a parameterization function

$$b(Q^2) \propto \left[1 - exp\left(-\frac{< \nu >}{M_\phi^2 + Q^2} \right) \right] \cdot \left(1 + \frac{P_{VM}}{\sqrt{1 + Q^2/M_\phi^2}} \right)^2 \tag{5.4}$$

where the parameter $P_{VM} = (r_{VM}/r_h)$ at $Q^2 = 0$, and the average value of photon energy, $< \nu >$, is 6 GeV for the ρ production data, and 4 GeV for the ϕ production data. Fitting the ρ data with this function we obtained

$$P_\rho = \left(\frac{r_\rho}{r_h} \right)_{Q^2=0} = 0.85 \pm 0.31 \,, \quad \chi^2/DF = 0.4 \,. \tag{5.5}$$

The low value of χ^2/DF for the ρ meson production shows a consistency of the data with the chosen parameterization. The fit of the ρ meson data is shown in Figure 5.2 with the black curve. For the ϕ production data the fit gives

$$P_\phi = \left(\frac{r_\phi}{r_h} \right)_{Q^2=0} = 0.51 \pm 0.04 \,, \quad \chi^2/DF = 2.3 \tag{5.6}$$

These results confirm the idea of the smaller size for the ϕ meson because of heavy quark, $s\bar{s}$, structure. Similar decrease rate of b_ϕ and b_ρ with Q^2 indicates the same nature of interaction size change for both ϕ and ρ mesons, and, subsequently, the same dominating production mechanism.

This is the first time the expected b_ϕ dependence on $\Delta\tau$ and Q^2 is seen in the $\phi(1020)$ vector meson reaction channel. The value of $c\Delta\tau$ below the size of nucleon puts the application of the VMD model in our kinematic regime in doubt [1] and indicate a point-like scattering regime. The application of QCD-based theoretical models, sensitive to the quark structure of the interacting meson and nucleon, would provides an interesting interpretation of the observed $b(Q^2)$ and $b(\Delta\tau)$ dependencies.

5.2 Cross-Section Dependence on Q^2

The comparison of our measured cross-section, $\sigma(Q^2, W)$, with the calculations from Reference [4] is shown in Figure 5.3. Here we show only the statistical errors. Systematic errors of the measurement are about 20%, mostly due to uncertainty in the background subtraction technique. We note that previous VMD model calculations of ϕ electroproduction did not include the t-slope, b_ϕ, dependence on Q^2, seen in this experiment. Therefore, it is not surprising that their predictions are not consistent with the data, and lie factor of five, in average, lower. The $s\bar{s}$-knockout model predicts a steep falloff of the ϕ cross-section with Q^2,

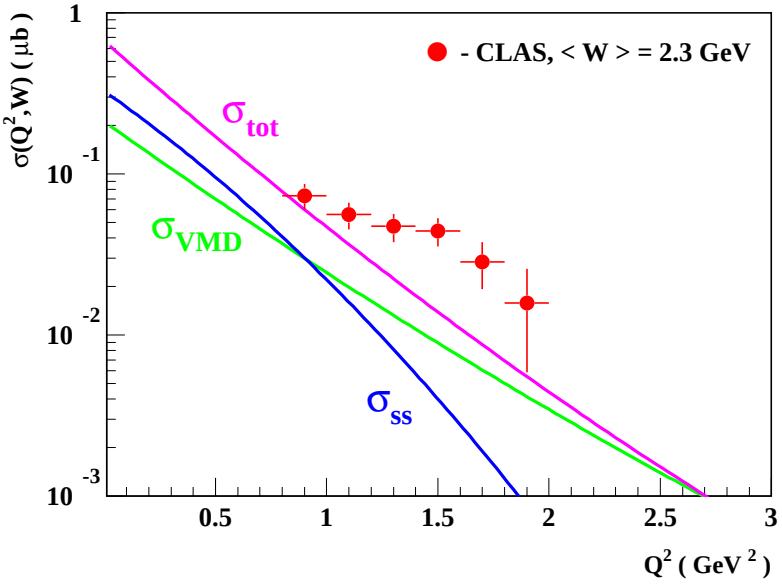

Figure 5.3: Comparison of the constituent quark and the VMD model predictions with CLAS data. The theoretical calculations were made at W = 2.1 GeV [4]. The green line is the diffractive contribution, blue and magenta lines are the $s\bar{s}$-knockout contribution and total cross-section, respectively.

when the data show the opposite behavior. Even at Q^2 close to 1 GeV^2 the $s\bar{s}$-knockout and VMD model prediction are close to the data, both models fail to describe the experimental cross-section distribution over the measured Q^2 range.

The comparison of our data with ZEUS data at high W [50, 48, 51], CORNELL data [6], BONN and SLAC photoproduction data at low W [71, 72], and Pomeron exchange model calculations is shown in Figure 5.4. The solid magenta and dashed green curves are the Pomeron exchange model predictions from Reference [11] at $W = 70$ and 2.3 GeV, respectively (see Section 1.2.2). The calculation describe very well the ZEUS data at $W = 70$ GeV, and the data at low W from Reference [6], BONN [71], SLAC [72] and the results of this experiment. Our data is in a very good agreement with the previous CORNELL measurement at $W = 2.8$ GeV.

Because of limited Q^2 range and large statistical errors, the sensitivity to the shape of the cross-section dependence on Q^2 is low. Here we show the results, obtained by applying two different parameterization functions:
a) Power law fit gives the value of power parameter 1.47 ± 0.37 with χ^2/DF of 0.51:

$$\sigma(Q^2) \propto \frac{1}{(Q^2)^{1.47}} \tag{5.7}$$

b) Parameterization with an exponential function gives the value of the slope parameter 1.17 ±0.41 with χ^2/DF of 0.35:

$$\sigma(Q^2) \propto exp\,(-1.17\,Q^2) \tag{5.8}$$

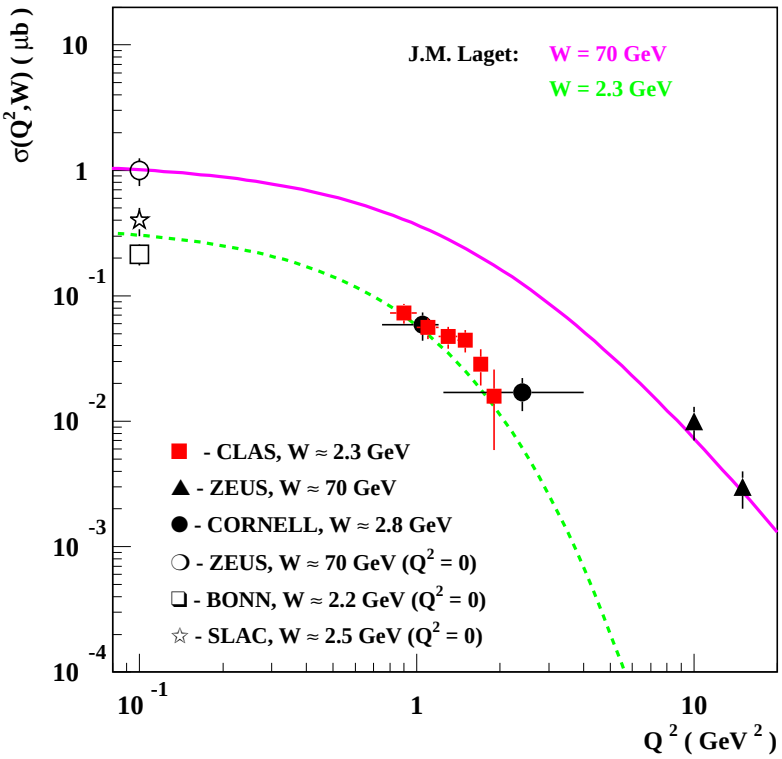

Figure 5.4: The ϕ meson cross-section, σ_ϕ, versus Q^2. The solid magenta and dashed green curves are the Pomeron-exchange model predictions at W = 70 and 2.3 GeV, respectively, from Reference [11]. The solid circles are CORNELL data from Reference [6] (for clarity, the point at $Q^2 = 1.1$ GeV^2 is shifted to the left on 0.05 GeV^2). The open circle and solid triangles are the ZEUS data from References [50, 48]. The open square and star are the photoproduction data from References [71] and [72], respectively. The solid red squares are the data from this experiment.

5.3 Comparison with VMD Model

R Measurement. The assumption of the VMD model and the SCHC allows the ratio of longitudinal to transverse cross-sections, R, to be determined from the polar angle distribution of the K^+ in the ϕ rest frame (see the frame definition in Figure 1.1). In terms of r^4_{00}, the probability that the ϕ meson is produced longitudinally polarized [12, 1, 7], R can be expressed as

$$R = \frac{1}{\epsilon} \frac{r^4_{00}}{1 - r^4_{00}}, \tag{5.9}$$

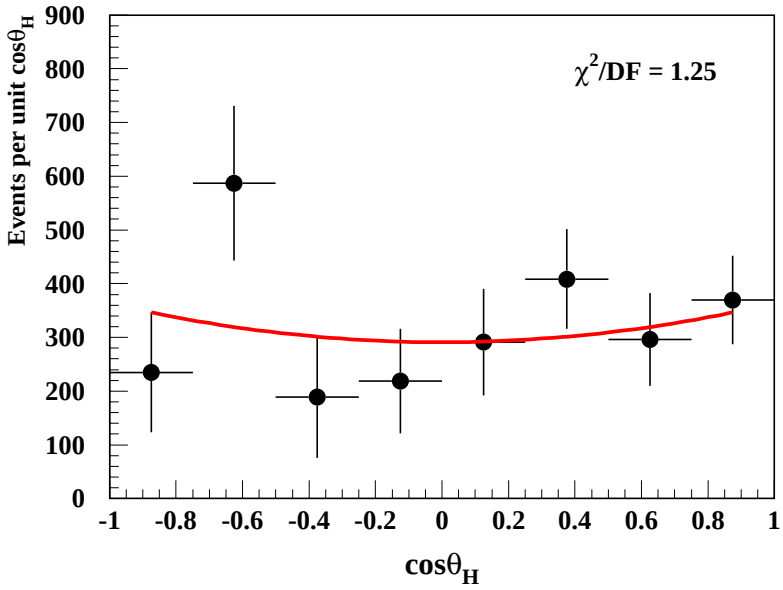

Figure 5.5: The measured $cos\theta_H$ angular distribution for Q^2 range from 0.7 to 2.2 GeV^2. The solid red line is the fit with the function from Equation 5.10.

where r^4_{00} is linear combination of matrix elements and can be extracted from the ϕ meson yield dependence on $cos\theta_H$. In term of r^4_{00} the Equation 1.20 can be written as [2].

$$\frac{dN}{dcos\theta_H} \propto 1 - r^4_{00} + (3r^4_{00} - 1)\ cos^2\theta_H\ . \tag{5.10}$$

The $cos\theta_H$ distribution for the entire data set is shown in Figure 5.5 [3]. The red line is the fit of the data with the function in Equation 5.10. The measured VMD model parameters are shown in Table 5.2. Our data point and the previous R measurements, plotted versus Q^2, are shown in Figure 5.6a. Our value of $R = 1.16 \pm 0.55$ is consistent with general behavior of the previous measurements and the VMD prediction (see Equation 1.18). A linear fit to the previous results from Reference [5] (open squares) together with our data point (red circle) gives the proportionality factor $\xi^2 = 0.366 \pm 0.102$ with χ^2/DF of 1.5. The Pomeron exchange model is also in a good agreement with the data, it predicts $R = 1.06$ at $Q^2 = 1$ GeV^2 [11].

Modified VMD Model. As the standard VMD parameterization, with a constant b_ϕ, fails to describe the measured cross-section dependence on Q^2 (see Figure 5.3), we modified the model in order to test the changes in its predictions. We included the measured $b_\phi(Q^2)$

[2] We have chosen to apply the Equations 5.9 and 5.10 for R measurement in order to be consistent with the analysis procedure in References [2, 7]

[3] In order to avoid distortion in the angular distribution, caused by complicated acceptance correlation, we applied an additional cut, requiring the difference $(\theta_{K^+} - \theta_{K^+})$ to be positive. With this cut we excluded the low acceptance region (see Figure 4.13 in Section 4.2.4).

Table 5.2: The measured VMD model parameters, all assuming SCHC.

Parameter	Value
r^4_{00}	0.384 ± 0.084
R	1.16 ± 0.55
ξ^2	0.366 ± 0.102

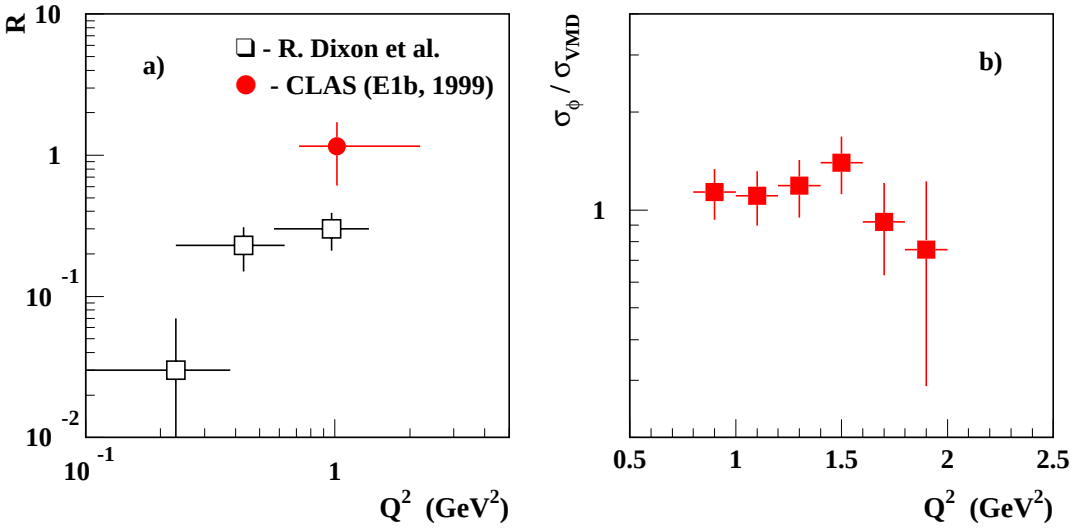

Figure 5.6: a) R dependence on Q^2. The open squares are the previous measurements from Reference [5], and the red circle is the data from this experiment. b) The ratio of measured, σ_ϕ, to calculated cross-section, σ_{VMD}, versus Q^2. The σ_{VMD} is calculated using the modified VMD model with the measured in this experiment b_ϕ dependence on Q^2 and $\xi^2 = 0.366$.

dependence (the red curve in Figure 5.2) in calculations of the cross-section $\sigma(Q^2)$. For the normalization we used the measured total cross-section of ϕ meson photoproduction from References [73, 74], $\sigma_{tot} = 0.3 \pm 0.1$ μb. The ratio of the measured to calculated cross-sections is shown in Figure 5.6b. Within the errors this modified VMD parameterization is consistent with the experimental data. We interpret this result as an additional indication on the importance of taking into account the t-slope parameter dependence on Q^2.

5.4 Production Mechanisms

In Figure 5.7 we show the measured differential cross-section, $d\sigma/dt'$, for the entire data sample in the Q^2 range from 0.7 to 2.2 GeV^2. At t' of about 1.1 GeV^2 an indication of change in the t-slope is observed. This behavior may confirm the theoretical calculations in Reference

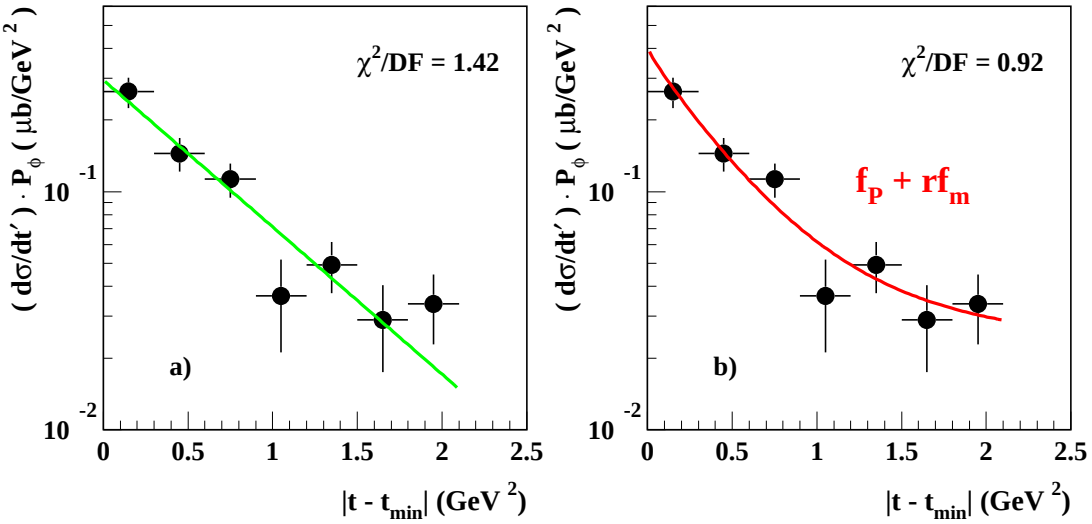

Figure 5.7: $d\sigma/dt'$ over all Q^2 range from 0.7 to 2.2 GeV^2. A change of the slope at about 1.1 GeV^2 can be seen. a) The fit to a single exponential function is shown with the green solid line. b) The red solid line is the fit to the parameterization functions of both Pomeron and meson exchange production mechanisms from Reference [41].

[41] (see Section 1.2.2). It is possible that in our kinematic regime the diffractive production mechanism is competing with the π and η meson-exchange production mechanisms. In order to test this prediction we fit the data with two different parameterizations. The solid green line in Figure 5.7a shows the fit with a single exponent, which is the general VMD prediction for the diffractive ϕ meson production. This fit gives a χ^2/DF of 1.42. The solid red line in Figure 5.7b represents the fit of the data to the function

$$f_{tot} = A(f_P + r f_m) \,, \tag{5.11}$$

where f_P and f_m are the parameterization functions of the diffractive and π/η-exchange production mechanisms, respectively (see Figure 1.15b); A is scaling parameter and r is the ratio of the contribution from two mechanisms. Since the calculations in Reference [41] were made for ϕ photoproduction, we modified the functions, taking into account the t-slope dependence on Q^2. This fit gives $A = 0.308 \pm 0.058$ and $r = 0.334 \pm 0.135$ with χ^2/DF of 0.92. We interpret this result as a preference for the π/η meson-exchange production contribution on the level of 33% in this kinematic regime, although the precision of this measurement is poor.

Chapter 6

Conclusions

The electroproduction of the $\phi(1020)$ vector meson was studied in the transition region of Q^2 from 0.7 to 2.2 GeV^2, W from 2.0 to 2.6 GeV, and $\Delta\tau$ from 1.8 to 3.8 GeV^{-1} ($c\Delta\tau$ from 0.4 to 0.9 fm). A sample of 278 $\phi(1020)$ vector mesons was accumulated in an exclusive measurement with the CLAS detector, Hall B, at Jefferson Lab. We find that this data has the following features:

• For the first time, we observe the expected t-slope dependence of the differential cross-section, $d\sigma/dt'$, on Q^2 and $\Delta\tau$ kinematic variables. The slope parameter, b_ϕ, decreases with increasing Q^2 and decreasing $c\Delta\tau$ below 1 fm. The rate of the b_ϕ decrease with Q^2 is similar to that for ρ meson production but with a lower asymptotic value. Within a simple optical model framework, the data show that ϕ meson has a smaller size than the ρ.

• The measured ϕ meson cross-section is in good agreement with the previous measurements. The standard VMD parameterization with a constant t-slope parameter, b_ϕ, and the $s\bar{s}$-knockout model both fail to accommodate the dependence of the measured cross-section on Q^2. The Pomeron-exchange model describes the data very well.

• The VMD model, modified for the measured b_ϕ dependence on Q^2, consistently describes the measured $\sigma(Q^2)$ within statistical errors.

• The VMD model parameters, R and ξ^2, have been extracted from the ϕ meson decay angular distribution, but with relatively large uncertainties. Within statistical errors the data agree with the previous measurements and the model expectations.

• The parameterization of the differential cross-section, $d\sigma/dt'$, in Q^2 range from 0.7 to 2.2 GeV^2 with both the diffractive and π/η meson exchange mechanism contributions describes the data slightly better than with the diffractive term alone. This is interpreted as a possible presence of about 33% π/η meson-exchange mechanism contribution in ϕ production in our kinematic regime.

Bibliography

[1] T.H. Bauer *et al*, Rev.Mod.Phys. 50, 261 (1978).

[2] EM Collaboration, J.J. Aubert *et al*, Phys.Lett. B161, 203 (1985).

[3] M. Atkinson *et al*, Z. Phys. C 30, 521 (1986).

[4] A. G. Williams *et al*, "Electro- and Photo Production of ϕ Mesons: Probing Strangeness in the Nucleon", talk at CEBAF 1992 Summer Workshop, Newport News, VA, 15-19 Jun 1992.

[5] R. Dixon *et al*, Phys. Rev. Lett. 39, n.9, 516 (1977).

[6] D.G. Cassel *et al*, Phys.Rev. D 24, 2787 (1981).

[7] J.A. Crittenden, "Topical Results on Vector-Meson Production from ZEUS and H1", Talk at the Joint INT/Jefferson Lab Workshop on Exclusive and Semi-exclusive Processes at High Momentum Transfer, May 20, 1999.

[8] L. Frankfurt, G. Miller, M. Strikman, Annu. Rev. Nucl. Sci., 501 (1994).

[9] K. Goulianos, Phys. Reports 101, n.3, 169 (1983).

[10] J. M. Laget, Nucl. Phys. A581, 397 (1995).

[11] J. M. Laget, Private communication.

[12] K. Schilling and G. Wolf, Nucl. Phys. B61, 381 (1973).

[13] J.J. Sakurai, Phys. Rev. Lett. 22, 981 (1969).

[14] H.J. Besh *et al*, Nucl. Phys. B70, 257 (1974).

[15] D.P. Barber *et al*, Phys. Lett. 79B, 150 (1978).

[16] H.-J. Behrend *et al*, Nucl. Phys. B144, 22 (1978).

[17] D.W.G.S. Leigh, High-Energy Photoproduction: Diffractive Processes", Electromagnetic Interactions of Hadrons, Vol. 1, Plenum Press, New York and London, A.Donnachie and G. Shaw, ads.

[18] A.H. Rosenfeld and P. Soding, "Photoproduction of Vector Mesons - Experimental", International School of Subnuclear Physics, Erice, Italy, 1971, A. Zichichi, ed.

[19] J.A. Crittenden, "Applications of QCD in Studies of Diffractive Processes at HERA", lecture at the University of Regensburg "Physics of the Strong Interaction", 30 June 1999.

[20] R.L. Anderson *et al*, Phys. Rev. Lett. 30, 149 (1973a).

[21] D.B. Kaplan *et al*, Nucl. Phys. B310, 527 (1988).

[22] M.D. Scadron, Z. Phys. C 54, 595 (1992).

[23] L. Ahrens *et al*, Phys. Rev D 35, 785 (1987).

[24] T.P. Cheng and R.F. Dashen. Phys. Rev. Lett. 26, 594 (1971); Phys. Rev. D 13, 216 (1976).

[25] C.A. Dominguez and P. Langacker, Phys. Rev. D 24, 1905 (1981).

[26] J. Gasser, H. Leutwyler and M.E. Sainio, Phys. Lett. B253, 252 (1991).

[27] J. Ellis *et al*, Phys. Lett. B217, 173 (1989).

[28] R.L. Jaffe, Phys. Lett. B229, 275 (1989).

[29] E.M. Henley *et al*, Phys. Lett. B269, 31 (1991).

[30] E.M. Henley *et al*, Phys. Lett. B281, 178 (1991).

[31] E.M. Henley *et al*, "Some Measurements for Determining Strangeness Matrix Elements in the Nucleon", XIIIth European Conference on Few-Body Problems in Physics, Marciane Marina, Island of Elba, Italy, 1991.

[32] J. Ballam *et al*, Phys. Rev. D 7, 3150 (1973).

[33] H.J. Halpern *et al*, Phys. Rev. Lett. 29, 1425 (1972).

[34] W.D. Shambroom *et al*, Phys. Rev. D 26, 1 (1982).

[35] P.G.O. Freund, Nuovo Cemento A48, 541 (1967).

[36] V. Barger and D. Cline, Phys. Rev. Lett. 24, 1313 (1970).

[37] H. Joos, Phys. Lett. B24, 103 (1967).

[38] K. Kajantie and J.S. Trefil, Phys. Lett. B24, 106 (1967).

[39] F. E. Low, Phys. Rev. D 12, 163 (1975).

[40] S. Nussinov, Phys. Rev. D 34, 1286 (1975).

[41] M.A. Pichowsky and T.-S. H. Lee, "Exclusive diffractive processes and the quark substructure of mesons", Phys. Rev. D 56, n.3, 1644 (1997).

[42] M.A. Pichowsky, private communication.

[43] T. Sato and T.-S. H. Lee, Phys. Rev. C 54, 2660 (1996).

[44] ZEUS Collaboration, M. Derrick *et al*, Z Phys. C 69, 39 (1995).

[45] W. Struczinski *et al*, Nucl. Phys. B108, 45 (1976).

[46] R. M. Egloff *et al*, Phys. Rev. Lett. 43, 657 (1979).

[47] D. Aston *et al*, Nucl. Phys. B209, 56 (1982).

[48] ZEUS Collaboration, M. Derrick *et al*, Phys. Lett. B377, 259 (1996).

[49] D. P. Barber *et al*, Z. Phys. C 12, 1 (1983).

[50] ZEUS Collaboration, M. Derrick *et al*, Phys. Lett. B380, 220 (1996).

[51] M. Arneodo *et al*, Nucl. Phys. B429, 503 (1994).

[52] Caso *et al*, Particle Data Group: Review of Particle Physics, The European Physical Journal C, v3, n.1-4 (1998).

[53] M.D. Mestayer *et al*, "The CLAS Drift Chamber System", in print at Nuclear Instruments and Methods.

[54] E. Smith *et al*, "Time of Flight system of CLAS", Nucl. Inst. and Meth. A 432, 265 (1999).

[55] E. Smith *et al*, "Calibration procedure for TOF of CLAS", CLAS-NOTE, 99-011.

[56] K. Schilling *et al*, Nucl. Phys. B15, 397 (1970).

[57] O. Dumbrajs *et al*, Nucl. Phys. B216, 277 (1983).

[58] H. Fraas, Nucl. Phys. B36, 191 (1972).

[59] L.N. Hand, Phys. Rev. 129, 1834 (1963).

[60] R.H. Dalitz, "The Production and Decay of Resonant States in Strong Interactions", Proceedings of the International School of Physics Enrico Fermi, 1966.

[61] H1 Collaboration, hep-ex/9902019, submitted Eur. Phys. C.

[62] W. Brooks *et al*, Proposal to (PAC6) "Measurement of the Polarization of the $\phi(1020)$ in Electroproduction.

[63] J. Aftosmis, J. Ficenec, D. Jenkins, and E. Smith, "Computer Modeling of Time-of-Flight Scintillator Pulses", CLAS Note 96-017, August 24, 1996.

[64] L. Elouadrhiri, V. Burkert, S. Stepanyan, H. Egiyan, "Charged Particle Identification in CLAS", CLAS Note 98-004, February 20, 1998

[65] K. Egiyan, "Determination of Electron Energy Cut due to the CLAS EC Threshold", CLAS-NOTE 1999-007, June 6, 1999.

[66] CLAS On-line Documentation.

[67] K. Loukachine and E. Smith, "Preliminary Results on $\phi(1020)$ Electroproduction at 4 GeV", CLAS-ANALYSIS, 99-001.

[68] S. Barrow, "$\Lambda^\star(1520)$ electroproduction results", CLAS-ANALYSIS note, in preparation.

[69] R. Thompson, private communication.

[70] C. Marchand, private communication.

[71] H. J. Besch *et al*, Nucl. Phys. B70, 257 (1974).

[72] J. Ballam *et al*, Phys.Rev. D5, 545 (1972); D7, 3150 (1973).

[73] ABBHHM Collaboration, Phys. Rev. 175, 1669 (1968).

[74] J. Ballam *et al*, Proc. 4th Intern. Symp. on Electron and Photon Interactions at High Energies 1969, Daresbury Nucl. Phus. Lab. 1969.

[75] W. Francis *et al*, Phys. Rev. Lett. 38, 633 (1977).

Appendix A

Properties of the $\phi(1020)$ vector meson.

The complete review of the properties of $\phi(1020)$ meson is given in [52]. The $\phi(1020)$ is a vector meson ($J^{PC} = 1^{--}$, I = 0), with a mass of 1019.413 $\pm$ 0.008 MeV and a full width $\Gamma = 4.43 \pm 0.06$ MeV. The branching ratio for B($\phi \rightarrow K\bar{K}$) = 83.5%, with the fraction of charged kaons B($\phi \rightarrow K^+K^-$) = 49.1%. The only other significant branching fraction is B($\phi \rightarrow \rho\pi$) = 12.9%. This experiment is based on detection of the decay to two charged kaons to tag the production of ϕ mesons.

Within the Quark Model for mesons, the ϕ may be written as a linear combination

$$| \phi \rangle \;\; = \;\; cos\theta \mid s\bar{s} \rangle + sin\theta \, \frac{1}{\sqrt{2}} \mid u\bar{u} + d\bar{d} \rangle \tag{6.1}$$

where $cos^2\theta$ represents the strange content in the ϕ. Normally, the mixing is given in the context of SU(3) in terms of octet and singlet components with a mixing angle θ_V. In terms of SU(3) mixing angle, one can write

$$cos\theta \;\; = \;\; \frac{cos\theta_V}{\sqrt{3}}(\sqrt{2} + tan\theta_V) \tag{6.2}$$

Various estimates of the mixing angle allow for the deviations of up to 4° from "ideal mixing", which corresponds to $\theta_V = 35.3°$. This determines the non-strange components in the ϕ to be less than 0.5%.

Appendix B

Decay Distributions

The $\phi \to K^+K^-$ decay correlation, $W^{unpol}(cos\theta, \varphi, \Phi)$, is the product of trigonometric functions of the K^+K^- decay angles, taken in the ϕ-meson center of mass (K^+ and K^- are back to back), and density matrix elements, $\rho_{\lambda,\lambda'}$, characterizing the ϕ's polarization. θ_H and ϕ_H are the polar and azimuthal decay angles and Φ is the angle between the electron and hadron scattering planes. Since $J_\gamma = J_\phi = 1$, the multi-polarity in these angles equals 2. Schilling and Wolf [12] decompose $\rho_{\lambda,\lambda'}$ into components $\rho^\alpha_{\lambda,\lambda'}$ characteristic of the γ_V polarization, i.e., α = 1, 2, ...6 = T, TT, TT, L, LT, LT. L = longitudinal, T = transverse, TT = transverse-transverse interference, etc. A general expression for W for electroproduced vector mesons is then derived in Reference [12] for unpolarized incident electrons:

$$
\begin{aligned}
W^{unpol} \;=\; & \frac{1}{1+(\epsilon+\delta)R}\,\frac{3}{4\pi} \\
& \times[\,\frac{1}{2}(1-\rho^0_{00}) + \frac{1}{2}(3\rho^0_{00}-1)\,cos^2\theta \;-\; \sqrt{2}\,Re(\rho^0_{10})\,sin2\theta\,cos\varphi \;-\; \rho^0_{1-1}\,sin^2\theta\,cos2\varphi \\
& - \epsilon\,cos2\Phi\,\{\,\rho^1_{11}sin^2\theta + \rho^1_{00}cos^2\theta \;-\; \sqrt{2}\,Re(\rho^0_{10})\,sin2\theta\,cos\varphi \;-\; \rho^1_{1-1}\,sin^2\theta\,cos2\varphi\,\} \\
& - \epsilon\,sin2\Phi\,\{\,\sqrt{2}\,Im(\rho^2_{10})\,sin2\theta\,sin\varphi \;+\; Im(\rho^2_{1-1})\,sin2\theta\,sin\varphi\,\} \\
& + (\epsilon+\delta)\,R\,\{\,\frac{1}{2}(1-\rho^4_{00} + \frac{1}{2}(3\rho^4_{00}-1)\,cos2\theta \;-\; \sqrt{2}\,\{\,Re(\rho^4_{10})\,sin2\theta\,cos\varphi \\
& - \rho^4_{1-1}\,sin^2\theta\,cos2\varphi\,\} \\
& + \sqrt{2\,\epsilon\,R\,(1+\epsilon+2\delta)}\,cos\Phi\,\{\,\rho^5_{11}\,sin^2\theta + \rho^5_{00}\,cos^2\theta \\
& + \sqrt{2}\,Re(\rho^5_{10})\,sin2\theta\,cos\varphi - \rho^5_{1-1}\,sin^2\theta\,cos2\varphi\,\} \\
& - \sqrt{2\,\epsilon\,R\,(1+\epsilon+2\delta)}\,sin\Phi\,\{\,\sqrt{2}Im(\rho^6_{10})\,sin2\theta\,sin\varphi \\
& + Im(\rho^6_{1-1})\,sin^2\theta\,sin2\varphi\,\}\,]. \qquad (6.3)
\end{aligned}
$$

R is the ratio of longitudinal to transverse cross section; $\delta = m_e/E \approx 0$. The transition amplitudes for the helicity conserving diffractive and pseudoscalar exchange scattering are incoherent; the two processes have additive terms in W^{unpol} [58].

The decay angles are defined relative to an appropriate coordinate system chosen to simplify

$\rho^{\alpha}_{\lambda,\lambda'}$. For diffractive helicity conserving ϕ production choosing the helicity frame (z-axis antiparallel to the outgoing proton direction, making it to be parallel the ϕ momentum direction), yields:

$$\rho^{\alpha}_{\lambda,\lambda'} \;=\; \rho^0, \rho^1, \rho^2, \rho^3, \rho^4, \rho^5, \rho^6 \quad (diffraction) \tag{6.4}$$

where ρ^{α} is defined in Appendix E of Reference [12].

$\rho^{\alpha}_{\lambda,\lambda'}$ for pseudoscalar exchange is obtained from the invariant amplitude for the upper (γ_V, PS, ϕ) pseudoscalar exchange vertex. The amplitude is the contraction of the anti-symmetric 4-tensor with the incoming γ_V and outgoing ϕ 4-momenta and 4-spin functions [58]. Using the Gottfried-Jackson frame, in which the coordinate system z-axis is parallel to γ_v, the invariant amplitude expression is greatly simplified - only transverse ϕ helicity remains, and the ϕ helicity matrices

$$\rho^{\alpha}_{\lambda,\lambda'} \;=\; \rho^0, -\rho^1, -\rho^2 \quad (PS\ exchange). \tag{6.5}$$

Expressions for pseudoscalar and diffractive W in the appropriate frames are given in Equations 1.30 and 1.19, where $\psi = \phi_H - \Phi$.

Following Reference [12], the helicity system should be chosen for the analysis. The pseudoscalar exchange, $\rho^{\alpha}_{\lambda,\lambda'}$, had to be rotated by angle $\alpha_{H\to GJ}$ from the Gottfried-Jackson frame into the helicity system.

$$\alpha_{H\to GJ} \;=\; cos^{-1}\frac{\beta^\star - cos\theta^\star}{\beta^\star cos\theta^\star - 1}\ , \tag{6.6}$$

where $\theta^\star$ is the hadron CMS scattering angle and $\beta^\star$ is the velocity of the ϕ in the hadronic CMS. $\alpha_{H\to GJ}$ increases rapidly from 0 at $t = t_{min}$. The increase of $\alpha_{H\to GJ}$ with t results in the ϕ unpolarized transfer (longitudinal) pseudoscalar exchange component decreasing (increasing) as t increases, providing a t signature for pseudoscalar exchange. At $t = t_{min}$, the unpolarized transverse component of the virtual photon gives only unpolarized transverse pseudoscalar exchange ϕ. This cannot be distinguished in W from the diffractive unpolarized transverse ϕ. As a result, at $t = t_{min}$, pseudoscalar exchange is distinguished from diffraction only in the two transverse-transverse components; the signs of PS ρ^1 and ρ^2 are opposite to those of diffraction, see Equations 6.4 and 6.5 above.

In general, the unpolarized transverse and transverse-transverse pseudoscalar components rotated from the Gottfried-Jackson frame into the helicity frame produce eight non-zero terms, with $\alpha = 0$, 1, 2, all proportional to the amount of pseudoscalar scattering. Helicity conserving diffractive scattering has, in the same system, six terms which can be grouped into three components, transverse unpolarized and transverse-transverse, (T, TT), with $\alpha =$ 1, 2; longitudinal, (L), with $\alpha = 4$; transverse-longitudinal, (LT), with $\alpha = 5$, 6.

Hence pseudoscalar exchange and helicity conserving diffractive scattering will produce four components in W, three diffractive and one pseudoscalar exchange:

$$W = F_{PS}W_{PS} + f_D^{T,TT}W_D^{TT} + f_D^{L}W_D^{L} + f_D^{LT}W_D^{LT}\ , \tag{6.7}$$

where the angular arguments of W have been omitted for brevity. Using Equations 105 and 106 in reference [12],

$$f_D^L \sim R \tag{6.8}$$

and

$$f_D^{LT} \sim \sqrt{R}\, cos\delta\ . \tag{6.9}$$

where δ is the phase angle of the longitudinal amplitude relative to the transverse in diffractive helicity conserving scattering. Using Equations 6.5, 6.8 and 6.9, the diffractive terms of Equation 6.7 can be collected together and written as a function of $cos\delta$ and ξ^2, in addition to the decay angles. The final expression is given in Equation 1.31.

Vita

Name: Konstantin Loukachine

May 1997 - 1999: Ph.D. candidate in Physics at Virginia Polytechnic Institute and State University on research at Jefferson Lab, Newport News, Virginia. Graduate Student Fellowship at Jefferson Lab, temporary (student) member of the CLAS Collaboration. The research on "Electroproduction of the $\phi(1020)$ Vector Meson at 4 GeV". Calibrations and maintenance of the Time-of-Flight (TOF) system of the CEBAF Large Acceptance Spectrometer (CLAS) in Hall B at Jefferson Lab. Design and performance of remote control of the TOF laser calibration system of CLAS. Design and maintenance of the TOF official web page. Coding in C, Perl and FORTRAN programming languages in UNIX and LINUX operating systems, developing the data analysis software and algorithms. Data processing and data analysis. The preliminary results on the thesis topic were presented at APS DNP meeting, Santa Fe, October 1998.

August 1996 - May 1997: Graduate student in Physics at Virginia Polytechnic Institute and State University. Teaching Assistant at Physics Department of VA Tech. Fulfillment of the academic requirements for the Ph.D. program in Physics.

March1995 - August 1996: Research Associate at Laboratorio Nazionale del Sud (LNS) of Instituto Nazionale di Fisica Nucleare (INFN), Catania, Italy. Studies of the HPDs (hybrid photo-diodes) properties. Design, performance and testing of the laser calibration system for the Multi Element DEtector Array (MEDEA). Participation in MACISTE project: calculations of multiple scattering and energy loses for the different configurations of the MACISTE spectrometer. Experimental research and data analysis on "Hard Photons and Energetic Protons production at intermediate energy ion beams" at LNS INFN. Presentation of the results on the MACISTE project at the LXXXI Congress of SIF (Societa' Italiana di Fisica) and at NSS IEEE conference, Fall 1995. Since Spring 1996 a reviewer of IEEE Transaction on Nuclear Science.

July 1994 - March 1995: Staff Scientist at St. Petersburg Nuclear Physics Institute (PNPI), Gatchina, Russia. Experimental research on the "Intermediate Mass Fragment Production on Au, Ag, Ni and Al Targets Induced by 1 GeV Protons" at PNPI.

July 1992 - July 1994: Fellowship for Foreigners of INFN, Italy. Experimental study on The Giant Resonances at GANIL, France. Installation and tests of the MEDEA detector at LNS INFN, Catania, Italy. Experience of working with heavy crystal (BaF_2) and plastic scintillator detectors, gas detectors and vacuum systems. Design of laser calibration system for the MEDEA detector based on the N_2 ultraviolet pulsed beam laser and quartz fiber optics.

February 1990 - July 1992: Research Associate and Staff Scientist at St. Petersburg Nuclear Physics Institute, Gatchina, Russia. Studies of BaF_2 properties for application in calorimetry measurements. Working on the Pre-shower Calorimetry technique using BaF_2 scintillator crystals and Resistive Parallel-Plate Counters ($RPPC$) for the separation of Electromagnetic Showers. Experimental Research on "Search for Di-barion Resonances Using Two Branch Time-of-Flight Spectrometer", acceptance calculation of the spectrometer, design of the electronic event-trigger, design and realization of the TOF laser calibration system. Experimental research on "Intermediate Mass Fragment Production on Light Targets Induced by 1 GeV Protons" at PNPI.

September 1987 - February 1990: Graduate student in Physics at St. Petersburg Polytechnic University, Russia. Fulfillment of the academic requirements for the Master of Science degree in Physics. Graduate thesis: "Ion Source for the Mass Separator with the Bunching of Ions". Achieved the Master of Science degree.

September 1984 - February 1987: Undergraduate student in Physics at St. Petersburg Polytechnic University, Russia.